A TWO-SEASON IMPACT STUDY OF ASCAT AND WINDSAT SURFACE WIND

RETRIEVALS IN THE NCEP GLOBAL DATA ASSIMILATION SYSTEM

by

Li Bi

A dissertation submitted in partial fulfillment of

the requirements for the degree of

Doctor of Philosophy

(Atmospheric and Oceanic Sciences)

at the

University of Wisconsin-Madison

2009

UMI Number: 3367611

INFORMATION TO USERS

The quality of this reproduction is dependent upon the quality of the copy
submitted.   Broken or indistinct print, colored or poor quality illustrations
and photographs, print bleed-through, substandard margins, and improper
alignment can adversely affect reproduction.
In the unlikely event that the author did not send a complete manuscript
and there are missing pages, these will be noted.   Also, if unauthorized
copyright material had to be removed, a note will indicate the deletion.

UMI®

A dissertation entitled

A TWO-SEASON IMPACT STUDY OF ASCAT AND

WINDSAT SURFACE WIND RETRIEVALS IN THE

NCEP GLOBAL DATA ASSIMILATION SYSTEM

submitted to the Graduate School of the
University of Wisconsin-Madison
in partial fulfillment of the requirements for the
degree of Doctor of Philosophy

by

Li Bi

Date of Final Oral Examination: **22 December, 2008**

Month & Year Degree to be awarded: **December**   **May** 2009   **August**

****
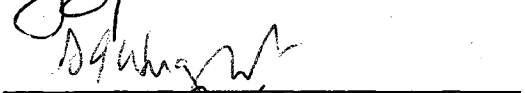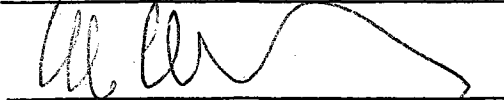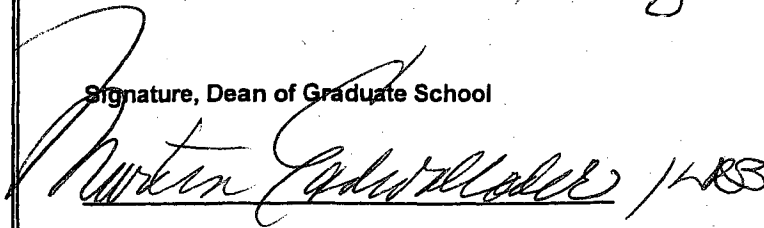
Approval Signatures of Dissertation Committee

Signature, Dean of Graduate School

Abstract

The WindSat/Coriolis satellite is the first polarimetric microwave radiometer used to measure ocean surface wind speed and direction. The Advanced SCATterometer (ASCAT) instrument, on the European Meteorological Operational (MetOp) satellite program's – polar orbiting MetOp-A satellite, is a scatterometer that has been primarily designed to provide global ocean wind with extended coverage, and better accuracy in the wind components than previous comparable satellites. In collaboration with NASA, the United States Navy, NOAA and NCEP personnel, the Joint Center for Satellite Data Assimilation (JCSDA) has been evaluating the forecast impact of assimilating WindSat and ASCAT data in the National Centers for Environmental Prediction (NCEP) Global Data Assimilation/Global Forecast System (GDAS/GFS) model.

Using the NCEP GDAS/GFS as the assimilation system and forecast model, the objective of this thesis is to evaluate through forecast hour 168, the forecast impacts associated with the assimilation of the WindSat and ASCAT surface wind products into the NCEP GDAS/GFS during two-season observing system experiments (OSEs).

The impacts of assimilating the ASCAT and WindSat surface wind products were assessed by comparing the output through 168 hours of control simulations utilizing all the data types assimilated into the operational GDAS with experimental simulations using these new surface wind products. Quality control procedures required to assimilate the surface winds are discussed. Anomaly correlations (AC) of geopotential height at 1000 and 500 hPa were evaluated for the control and experiment during both seasons.

The geographical distribution of forecast impact on the 10m wind, 500 hPa wind, 1000hPa temperature, and 500 hPa temperature fields are also presented.

The results of these studies show that the assimilation of WindSat and ASCAT surface wind retrievals improves forecast skills in terms of traditional anomaly correlation. In addition to use NCEP's verification software to quantify forecast impacts, after the two season surface winds experiments were completed, we compared the attributes of forecasts using the ASCAT/WindSat data to a set of control forecast experiments by computing the geographic distribution of Forecast Impact (FI). FI study is a useful tool to diagnosis the short term forecast skill before the statistical results are shown in the traditional anomaly correlation curve. Positive forecast impacts are noted of wind and temperature field particularly in the tropics for 500hPa wind speed field starting from 6 hour forecast and beyond.

In addition to the forecast impact results from assimilation of the ocean surface wind vectors, case assessments have been performed to investigate the surface winds vectors' impacts on the development African easterly waves. Results of this study are discussed.

Acknowledgements

I wish to express my gratitude to Dr. Michael Morgan, my advisor, for his guidance and support with my academics and this research. Without Dr. Morgan's support, help and guidance, none of this work would have been possible. He has been and continues to be a source of encouragement, for which I am most grateful. Thanks to the faculty members on my committee: Dr. Steve Ackerman, Dr. Ralf Bennartz, Dr. John F. Le Marshall, Dr. Jon Martin, and Dr. Steve Wright. I cannot thank them enough for their advice and suggestions in completing this research. I wish also thank Dr. Tom Zapotocny and Dr. James Jung for their encouragement and support.

I wish to thank Dr. Todd Schaack and Dr. Will Lewis for giving me helpful suggestions. Thanks to Dr. Lars Peter Riishojgaard and Dr. John Derber for giving me insightful advice. Additional thanks to the support from Dr. Morgan's research group and my friends in UW-Madison.

Thanks are also due to: Peter Gaiser and Mike Bettenhausen of the Naval Research Laboratory for providing WindSat data, Zorana Jelenak of the Center for Satellite Applications and Research for providing ASCAT data. Dennis Keyser and Stacie Bender of the National Center for Environmental Prediction for collecting and processing the various data streams.

This research was supported under National Oceanographic and Atmospheric Administration (NOAA) grant NA06NES4400002 and the Joint Center for Satellite data Assimilation (JCSDA).

Finally, I must mention the unending supporting of my entire family: my mother Shi and my father Chao; my daughter Allison; and especially my husband Kai, who have all been patient and supported my higher education effort.

Table of Contents

List of Figures

List of Tables

Chapter 1: Introduction

Sea surface wind vectors have been estimated with active remote sensing instruments, such as QuikSCAT (Yu and McPherson 1984) and the Advanced SCATterometer (ASCAT) and with passive polarimetric microwave radiometry, such as WindSat (Bettenhausen et al., 2006). The assimilation of these near-ocean surface wind vectors has been proven to have a positive impact on NCEP global forecasts (Le Marshall et al., 2006, Bi et al., 2008).

The primary application of spaceborne scatterometry is to provide estimates of near-surface winds over the ocean. The notion of meteorological scatterometery has its origins in some of the earliest uses of radar during World War II. At that time, the earliest measurements from radar the over oceans were found to be corrupted by sea clutter (noise). It was not known that the noise could be attributed to the radar response to the winds over the oceans. Radar response was first related to wind in the late 1960's. The first spaceborne scatterometer, which flew as part of the NASA Skylab missions in 1973 and 1974, demonstrated the feasibility of spaceborne scatterometry.

Since 1991 scatterometers onboard satellites have provided continuous surface wind speed and direction estimates over the global oceans. Scatterometer surface wind products are widely used for various scientific and operational purposes. For instance, scatterometer surface wind measurements have been used to enhance the determination of the ocean circulation model forcing function at global and regional scales. These wind

products have been successfully assimilated in numerical weather prediction models (e.g. Figa etal., 2000). Numerous studies have demonstrated the positive impact of scatterometer wind retrievals in prediction and describing tropical cyclones (e.g. Le Marshall et al., 2000; Katsaros et al., 2001). All these studies contribute significantly to promoting the use of remotely sensed winds and encourage satellite organizations to maintain surface observation systems from scatterometers.

As the only remote sensing systems able to provide accurate, frequent, high-resolution measurements of ocean surface wind speed and direction under both clear sky and cloudy conditions, scatterometers play an increasingly important role in oceanographic, meteorological, and climatic studies. Scatterometers use an indirect technique to measure wind over the ocean, since the atmospheric motions themselves do not substantially affect the radiation emitted and received by the radar. Scatterometers transmit microwave pulses and receive backscattered power from the ocean surface. Changes in wind velocity cause changes in ocean surface roughness, modifying the radar cross-section of the ocean and the magnitude of the backscattered power. Scatterometers measure this backscattered power, allowing estimation of the normalized radar cross section (σ_0) of the sea surface. Backscatter cross section varies with both wind speed and direction when measured at moderate incidence angles. Multiple, collocated, nearly simultaneous σ_0 measurements acquired from several directions can thus be used to retrieve (i.e., solve simultaneously for) wind speed and direction.

Polarimetric microwave radiometers measure passively the microwave radiation emitted from the ocean surface and quantifies these measurements in terms of the

brightness temperature. In microwave measurement systems, the amount of radiation detected depends on the properties of the scene and the observation frequency. Wind roughening the surface of the ocean causes an increase in the brightness temperature of the microwave radiation emitted from the water's surface. Airborne experiments conducted jointly by Naval Research Laboratory and the Jet Propulsion Laboratory have indicated that there is a relationship between wind speed and direction and the surface roughness.

In this dissertation, we consider three satellite remote sensing systems, QuickSCAT, ASCAT, and WindSat.

Thesis objectives and structure

As the objectives of this thesis, two seasons of WindSat/ASCAT data have been assimilated into the NCEP GDAS/GFS model, the forecast impact of assimilating the WindSat surface winds was assessed by comparing the forecast results with and without assimilating the WindSat/ASCAT winds through 168 hours for the months of October 2006 and March 2007 for the WindSat experiment and months of August 2007 and January 2008 for the ASCAT experiment. Quality control procedures required to assimilate the surface winds are also discussed and the geographical distribution of the anomaly correlations and forecast impacts are presented.

The thesis is structured as follows. Chapter 2 briefly describes background information related to the National Centers for Environmental Prediction (NCEP) Global Data Assimilation/Global Forecast System (GDAS/GFS) version used for this study.

Chapter 3 discusses the diagnostic tools used to evaluate the forecast impacts. The results of the calculations the author performed for the WindSat experiments are found in chapter 4. These results were published in Le Marshall et al. (2006) prior to the defense of this dissertation. Chapters 5 and 6 are intended to be stand-alone papers that will be submitted to refereed journals following the defense. References cited in chapters 5 and 6 are found at the end of the dissertation. Chapter 5 presents the results for this WindSat forecast impact study through 7 days of model forecasts. Chapter 6 presents the results for this WindSat forecast impact study through 7 days of model forecasts. Chapter 7 presents the results from case study and the investigation of how the surface winds affect the forecase development of African easterly waves. Chapter 8 summarizes the overall results of these experiments and provides a critique of the experimental design used to evaluate the usefulness of observations taken from new observational platforms.

Chapter 2: Background information

2.1 Overview of ocean surface wind vector sensors

Oceanic near-surface wind vector is a key parameter for short-term weather forecasting, the issuing of timely weather warning, and the gathering of general climatological data. In addition, it affects a broad range of naval missions, including strategic ship movement and positioning, aircraft carrier operations.Near surface wind data, combined with other remotely sensed and *in situ* measurements help in understanding mechanisms of global climatic change and weather. These measurements will help to determine atmospheric forcing, ocean response and air-sea interaction mechanisms on various spatial and temporal scales. (QuikSCAT Science Data Product User's Manual, 2001) Wind stress is the single largest source of momentum to the upper ocean, driving ocean motions on scales ranging from surface waves to basin-wide current systems. Winds over the ocean modulate air-sea fluxes of hear, moisture, gases and particulates, regulating the crucial coupling between atmosphere and ocean that establishes and maintains global and regional climate. Measurements of surface wind velocity can be assimilated into regional and global numerical weather and wave prediction models, potentially improving the ability to predict weather on longer time scales.

WindSat measurements will help researchers determine atmospheric forcing, ocean response and air-sea interaction mechanisms on various spatial and temporal scales.

Operational users will need to develop improved methods of assimilating wind data into numerical weather and wave-prediction models.

Since 1991 scatterometers onboard satellites provide continuously valuable surface wind speed and direction estimates over global ocean. Scatterometer surface wind products are widely used for various scientific and operational purposes. For instance, they were used to enhance the determination of the ocean circulation model forcing function at global scale as well as at regional scales. They were successfully used within assimilation process in numerical weather prediction models. Numerous studies demonstrated the positive impact of scatterometer wind retrievals in prediction and diagnosis of tropical cyclone structure. All these studies contribute significantly to promote the use of remotely sensed winds and encourage satellite organizations to maintain surface observation systems from scatterometers.

2.1.1 Overview of QuikSCAT scatterometer and measurement geometries

The SeaWinds on QuikSCAT mission was flown as a "quick recovery" mission in June 1999 to fill the gap created by the loss of data from the NASA Scatterometer (NSCAT) in June 1997. The QuikSCAT satellite was launched into a sun-synchronous, 803-kilometer, circular orbit with a local equator crossing time at the ascending node of 6:00 A.M ±30 minutes. Table 2.1 lists the parameters that defines the nominal orbit for QuikSCAT:

Table 2.1. Nominal Orbital Parameters

Recurrent Period	4 days (57 orbits)
Orbital Period	101 minutes (14.25 orbits/day)
Local Sun time and Ascending node	6:00A.M ± 30 minutes
Altitude above Equator	803 km
Inclination	98.6160^0

The SeaWinds instrument on QuikSCAT is an active microwave radar designed to measure electromagnetic backscatter from wind roughed ocean surface and infer subsequently the near-surface wind speed and direction under all weather and cloud conditions over Earth's ocean. QuikSCAT uses a dual-beam, conically scanning rotating antenna that samples the full range of azimuth angles during each revolution. At the QuikSCAT orbital altitude of 803 km, the radii of the inner and outer beams are about 700 and 900km. In principle, the QuikSCAT measurement approach therefore yields a single, contiguous swath of 1800-km width centered on the satellite's nadir subtrack over ocean, land, and ice. This approach allows for approximately 1.1 million daily ocean surface wind estimates to be obtained .

Spaceborne scatterometers transmit microwave pulses to the ocean surface and measure the backscattered power received at the instrument. Since atmospheric motions themselves do not substantially affect the radiation emitted and received by the radar, scatterometers use an indirect technique to measure wind velocity over the ocean. Wind stress over the ocean generates ripples and small waves, which roughen the sea surface. These waves modify the radar cross section (σ_0) of the ocean surface and hence the magnitude of backscattered power. In order to retrieve wind vector estimates from these measurements, the relationship between σ_0 and near-surface winds, known as the geophysical model function, must be developed.

The cross section σ_0 varies with wind speed, wind direction relative to the antenna azimuth, incidence angle, polarization, and radar frequency. Near-simultaneous, collocated σ_0 measurements are acquired from different measurement geometries and polarizations, allowing wind speed and direction to be retrieved in ground processing (Naderi et al. 1991). The scatterometers developed and operated by NASA acquire vertically and horizontally polarized σ_0 measurements at Ku-band frequency (13.4 GHz) with approximately 25-km resolutions.

An accurate model function is essential to deriving ocean wind vectors from scatterometers measurement. The initial post-launch model function used for QuikSCAT was the NSCAT-2 model. Starting with the version 2.0 of the data set, the model function used was the QSCAT-1 model developed during the QuikSCAT calibration/validation phase. Finally, the recalibrated model function called QSCAT-1/F13 was used for all L2B processing staring July 2006. The SeaWinds wind retrieval algorithm uses a maximum-likelihood estimator (MLE) as the objective function for determining wind vector solutions.

The wind retrievals are calibrated to the equivalent neutral-stability wind at a reference height of 10m above the sea surface – that is, the 10m wind that would be associated with the observed surface stress if the atmospheric boundary layer were neutrally stratified (Liu and Tang 1996).

2.1.2 Overview of WindSat radiometry

(a) Mission Description

The WindSat payload was launched on 6 January 2003 on the Coriolis satellite. Coriolis was originally designed as a 3-year demonstration/validation mission sponsored by the Department of Defense (DoD) Space Test Program (STP), the U.S Navy and the National Polar-Orbiting Operational Environmental Satellite System (NPOESS) Integrated Program Office (IPO). The primary payload, WindSat, is a multi-frequency polarimetric microwave radiometer developed by the Naval Research Laboratory Remote Sensing Division. WindSat is designed to demonstrate the viability of using polarimetric microwave radiometry to measure the ocean surface wind vector from space.

Coriolis is in a 98.7^0 inclined orbit at an altitude of about 830km and with a local ascending node time near 1800 UTC. It completes about 14 orbits per day with each orbit requiring 102 minutes. WindSat records data on both the forward (fore) and back (aft) side of each spin of the conically scanning feedhorn structure. The on-Earth fore- and aft-viewing swath width encompasses 1025 and 350 km, respectively, as the sensor's conical scan spins counterclockwise (Gaiser et al., 2004). The nominal orbit for CORIOLIS is defined by the following parameters lists in Table 2.2.

Table 2.2. Nominal Orbital Parameters

Recurrent Period	8 days
Orbital Period	102 minutes (14 orbits/day)
Local Sun time and Ascending node	6:00 P.M.
Altitude above Equator	840 km
Inclination	98.7^0

(b) WindSat Sensor Overview and measurement geometries

The WindSat radiometer has polarimetric channels at 10.7, 18.7 and 37.0 GHz and dual-polarization (vertical and horizontal) channels at 6.8 and 23.8 GHz. These

provide information related to surface wind vectors, sea surface temperature, atmospheric water vapor, integrated cloud liquid water and rain rate over the ocean. Measurements of the modified Stokes vector provide sufficient information to retrieve the ocean wind vector. The 6.8GHz dual-polarized channel is sensitive to sea surface temperature (SST) and is used to determine effects due to variations in SST. Similarly, the 23.8GHz dual-polarized channel is highly sensitive to atmospheric water vapor. Consequently, measurements at 23.8 GHz help determine the effects of atmospheric attenuation on radiation from the ocean surface. The WindSat instrument channel characteristics are summarized in Table 2.3.

Table 2.3. WindSat Characteristics

Frequency (GHz)	Polarization	Bandwidth (MHz)	Incidence Angle (deg)	Spatial Resolution (km)
6.8	V. H	125	53.5	40x60
10.7	V, H, ±45, L, R	300	49.9	25x38
18.7	V, H,± 45, L, R	750	55.3	16x27
23.8	V,H	500	53.0	12x20
37.0	V, H, ±45, L, R	2000	53.0	8x13

NRL has developed a nonlinear iterative algorithm for simultaneous retrieval of sea surface temperature, columnar water vapor, columnar cloud liquid water, and the ocean surface wind vector from WindSat measurements. The algorithm uses a physically based forward model for estimating the WindSat brightness temperature. From the radiation measurements of the modified Stokes vector, which includes the vertical and horizontal polarizations and the third and fourth Stokes parameters, wind speed and direction can be retrieved (Bettenhausen et al., 2006). The ocean surface wind vectors have been determined using a non-linear iterative optimal estimation method which

employs a one-layer atmospheric and a sea surface emissivity model. WindSat wind speed retrieval processing also uses a median filtering technique to smooth the final wind field and applies empirical corrections to the vertically and horizontally polarized brightness temperature to the physically based model (Bettenhausen et al., 2006).

Various improvements to the WindSat wind vector retrieval algorithm were incorporated to derive the wind vectors (version 2) and used to generate the data in this study (Peter Gaiser, personal communication). The wind data were delivered as Environmental Data Records (EDRs) and put into Binary Universal Form for the Representation of meteorological data (BUFR) format at the National Oceanic and Atmospheric Administration's (NOAA) NCEP in preparation for operational use.

2.1.3 Overview of ASCAT scatterometer

(a) Mission Description

The ASCAT mission has been primarily designed to provide global ocean wind vectors operationally. The main application foreseen is the assimilation of those winds into numerical weather prediction (NWP) models. Furthermore, its dense coverage makes the winds useful for direct use by operational weather forecasters when performing the necessary real-time interpretation of NWP model results to elaborate a forecast. Requirements arising from the use of the data include (1) extended coverage; (2) better accuracy in the wind components; and (3) real-time data access.

ASCAT is on the MetOP-A satellite which was launched on 19 October 2006. MetOp-A is the first in series of three satellites developed to provide meteorological data until 2020. MetOp is in a circular orbit (near sun synchronous orbit) for a period of about

101 minutes, at an inclination of 98.59^0 and at a nominal height of 800km with a 29-day repeat cycle. The ascending equatorial times occur approximately at 09:30 p.m. local time for MetOp. ASCAT has two swaths 550 km wide, located on each side of the satellite track, separated by 700km. It operates at 5.3 GHz (C band) (Bentamy, 2008). Besides ASCAT, MHS, AVHRR, AMSU-A, IASI and GOME-2 are also on board MetOp-A. The nominal orbit for MetOp is defined by the following parameters lists in Table 2.4.

Table 2.4 Nominal Orbital Parameters

Recurrent Period	29 days
Orbital Period	101 minutes (14 orbits/day)
Local Sun time and Ascending node	9:30 P.M.
Altitude above Equator	800 km
Inclination	98.59^0

(b) ASCAT Sensor Overview and measurement geometries

ASCAT is a real aperture radar using vertically polarized antennas. It transmits a long pulse with a linear frequency modulation or 'chirp'. Ground echoes are received by the instrument and, after de-chirping, the backscattered signal is spectrally analysed and detected. The ASCAT beams measure normalized radar cross sections with vertical polarization, which are a dimensionless property of the surface, describing the ratio of the effective echoing area per unit area illuminated. The backscattered signal is spectrally detected and analyzed. In the power spectrum, frequency can be mapped into slant range provided the chirp rate and the Doppler frequency are known. The above processing is in

effect a pulse compression, which provides range resolution (http://www.knmi.nl/scatterometer/publications/pdf/ASCAT_Product_Manual.pdf).

Two sets of three antennas are used to generate radar beams looking 45° forward, sideways, and 45° backwards with respect to the satellite's flight direction, on both sides of the satellite ground track. These beams illuminate 550 km-wide swaths (separated by about 700km) as the satellite moves along its orbit, and each provides measurements of radar backscatter from the sea surface on a 25 km or 12.5 km grid. The result of three independent backscatter measurements for each wind vector cell are obtained using the three different viewing directions and separated by a short time delay. As the backscatter depends on the sea surface roughness as a function of the wind speed and direction at the ocean surface, it is possible to calculate the surface wind speed and direction by using these 'triplets' within a mathematical model (http://www.knmi.nl/scatterometer/publications/pdf/ASCAT_Product_Manual.pdf).

The Koninklijk Nederlands Meteorologisch Instituut (KNMI) (Royal Netherlands Meteorological Institute) processes and makes available surface wind vector data derived from the ASCAT backscatter coefficient. For the KNMI ASCAT wind product, the CMOD5.5 geophysical model function (GMF) is used http://www.knmi.nl/scatterometer/publications/pdf/ASCAT_Product_Manual.pdf). The GMF has two unknowns, namely wind speed and wind direction, so, if more than two backscatter measurements are available then these two unknowns may by estimated using a maximum-likelihood estimator (MLE) as the objective function for determining wind vector solutions

(http://www.knmi.nl/scatterometer/publications/pdf/ASCAT_Product_Manual.pdf).   The

solution selection is performed based on the 2D-VAR method (Stoffelen et al., 2002).

ASCAT wind products (L2 b product) were declared pre-operational on 10 October 2007

at the end of the scatterometer calibration experiment using a ground transponder.

The ASCAT data flow from the MetOp satellite to the National Oceanic and

Atmospheric Administration's (NOAA) processing system and are converted into Binary

Universal Form for the Representation of meteorological data (BUFR) format at the

NOAA NCEP in preparation for operational use.

2.2 Overview of Global Data Assimilation System/Global Forecast System

A January 2007 version of the Gridpoint Statistical Interpolation (GSI) routine

and GFS were used for the observing system experiments. The NCEP assimilation

system consists of a first or "early" cycle with a 2.5 hour cut-off. The analyses for this

cycle are performed at times centered on 0000, 0600, 1200 and 1800 UTC and are

followed by a 384 hour forecast. Consistent with the operational GDAS/GFS, a model

resolution of T382L64 (i.e., spectral triangular truncation 382 with 64 layers) is used

through 168 hours. For this study, only the 0000 UTC forecasts were run. The analysis

is repeated later (+6 hrs) to provide the "final" analysis for the six hour forecast for the

next early cycle first guess. This "final" analysis includes data that had missed the

previous "early" data cut-off.

The vertical domain of GFS model ranges from the surface to approximately 0.27

hPa and is divided into 64 unequally spaced sigma levels with enhanced resolution near

the bottom and top of the model domain. There are 15 layers below 800 hPa and 24

layers above 100 hPa. The time integration is leapfrog for nonlinear advection terms and semi-implicit for gravity waves and the zonal advection of vorticity and moisture. Comprehensive documentation of the GFS was completed by the National Meteorological Center (NMC) (now NCEP) Development Division (1988) and can be found online at http://wwt.emc.ncep.noaa.gov/gmb/wd23ja/doc/web2/tocold1.html. Subsequent model developments after completion of the above documentation have been summarized by Kanamitsu (1989), Kalnay (1990), and Kanamitsu et al. (1991). More recent updates to the radiation, surface layer, vertical diffusion, gravity wave drag, convective precipitation, shallow convection and non-convective precipitation can be found at http://sgi62.wwb.noaa.gov:8080/research/SONGYU/doc/physmrf1.html. The most recent information about the GFS atmospheric model (2003) is in NCEP Office Note No. 442 or online at http://emc.ncep.noaa.gov/officenotes/newernotes/OF442.pdf. A summary of GFS changes and references up to and past the dates of this study are available in an "updates" log of changes online at both http://www.emc.ncep.noaa.gov/gmb/moorthi/gam.html and http://www.emc.ncep.noaa.gov/gmb/STATS/html/model_changes.html.

The GDAS utilizes a three-dimensional variational data assimilation (3DVAR) scheme to obtain an initial state that fits optimally (in a least squares sense) the available observations and a short-range (6 hour) forecast (background). In this study, we use NCEP's GSI (Derber et al. 1991; Wu et al. 2002; Derber et al. 2003) 3DVAR system. With this type of analysis system, the incorporation of radiances directly into the analysis and assimilation system has become practical. The analysis becomes a 3D retrieval of

mass, momentum, and moisture fields derived from all available data including the radiances (Caplan et al. 1997).The GSI uses a thinning routine which identifies the optimal radiance profile for each satellite sensor type (AMSU, HIRS, MSU, etc.) in a pre-designated grid box. The optimal radiance profile is determined by its departure from the model background temperature, distance from the center of the grid box, temporal departure from the assimilation time, and surface features (ocean, land, and ice).

Chapter 3 Diagnostics Tools

Several diagnostics were performed using the Control and WindSat/ASCAT experiment analyses and forecasts. In this section we briefly describe the diagnostics used throughout this thesis.

3.1 Anomaly Correlation (AC) statistics

The anomaly correlation (AC) is the correlation between the forecast and analyzed deviations from climate and can be regarded as a skill score with reference to the climate. In this study, the AC statistics were performed using the traditional NCEP algorithms (NWS 2006) which are commonly used by NWP centers worldwide. The computation of all anomaly correlations for forecasts produced by the GFS are completed using code developed and maintained at NCEP. NCEP (NWS 2006) provides a description of the method of computation while Lahoz (1999) provides an interpretation for the anomaly correlation statistic. The reanalysis fields from the National Center for Atmospheric Research (NCEP/NCAR) (Kistler 2001) are used for the climate component of the anomaly correlations. This reanalysis was run at a resolution of T62L28. The output grids were reduced to 2.5° by 2.5° horizontal resolution and to rawinsonde mandatory levels. To calculate anomaly correlations the output grids from the control and both experiments were reduced to this 2.5° by 2.5° horizontal resolution using the GFS post processor. The fields being evaluated using anomaly correlations are truncated to only include spectral wave numbers 1 through 20. These fields are also limited to the zonal bands of 20°-80° in each Hemisphere and a tropical belt within 20° of the equator

(20°N to 20°S).

The anomaly correlation coefficient is computed for individual model forecasts and the ensemble based on the method suggested by Brankovic et al. (1990). Anomaly correlation for forecast variables is defined as the correlation between the predicted and analyzed anomalies of the variables. Here anomalies are deviations from the mean climatological values. The following expression is used for computing the anomaly correlation of geopotential height at 500hpa.

$$ACC = \frac{\sum \left\{ \left[(Z_F - Z_c) - \overline{(Z_F - Z_c)} \right] \cdot \left[(Z_V - Z_c) - \overline{(Z_V - Z_c)} \right] \right\}}{\sqrt{\sum \left[(Z_F - Z_c) - \overline{(Z_F - Z_c)} \right]^2 \sum \left[(Z_V - Z_c) - \overline{(Z_V - Z_c)} \right]^2}}$$

Here suffix F denotes forecast, suffix C denotes climatology and suffix V stands for verifying analysis. Over bar is the area mean and Z is the geopotential height at 500hPa.

3.2 Geographic Distribution of the AC

In addition to the traditional AC statistics, geographic distributions of the AC for the 1000hPa and 500hPa geopotential height fields are performed. The field being evaluated using geographic AC distributions include all spectral wave numbers. These fields are not limited to the zonal bands or the tropical belt.

3.3 Forecast Impact (FI)

Another diagnostic used here is the modified forecast impact (FI), which is discussed further by Zapotocny et al. (2005). For this study, a series of two-dimensional FI results are presented as the positive/negative impact provided by the experiment of a

particular data type. The geographic distributions of FI are shown in section 4.b and are evaluated using:

$$FI(x,y) = 100 \times \{[\sqrt{\frac{\sum_{i=1}^{N}(C_i - A_i)^2}{N}} - \sqrt{\frac{\sum_{i=1}^{N}(E_i - A_i)^2}{N}}]/\sqrt{\frac{\sum_{i=1}^{N}(E_i - A_i)^2}{N}}\} \quad (1)$$

The variables C and E are the control and experiment forecasts, respectively. The variable A is the 00-hr GDAS experiment analysis containing all data types which is valid at the same time as the forecasts. N is the number of diagnostic days.

The area ratio weights the grid points to account for the reduction in area as the grid boxes approach the poles. The area ratio weighting is defined as:

$$A_i' = A_i \times \frac{\sin(\phi_i + \frac{\Delta}{2}) - \sin(\phi_i - \frac{\Delta}{2})}{2\sin(\frac{\Delta}{2})} \quad (2)$$

Where ϕ is the latitude of grid point i and Δ is north/south resolution of the grid box. The numerator is the relative size of the grid box. The denominator is the relative size of a grid box at the equator.

The vertical cross section plots shown in section 4.c are evaluated using:

$$FI(t,z) = 100 \times \left[\frac{\sqrt{\frac{\sum_{i=1}^{X}(C_i' - A_i')^2}{X}} - \sqrt{\frac{\sum_{i=1}^{X}(E_i' - A_i')^2}{X}}}{\sqrt{\frac{\sum_{i=1}^{X}(E_i' - A_i')^2}{X}}} \right] \quad (3)$$

Where X is the number of horizontal grid points. A', C' and E' are the area ratio

weighted values of A, C and E defined in (1). The first term on the right enclosed by parentheses in (1) and (3) can be considered the error in the denied experiment. The second term enclosed by parentheses in (1) and (3) can be considered the error in the control forecast. Dividing by the error of the control forecast normalizes the results. Multiplying by 100 provides a percent improvement/degradation with respect to the RMS error of the control forecast. A positive forecast impact means the WindSat forecast compares more favorably to its corresponding analysis than the control.

The FI is then averaged over the number of days by using:

$$F_t = \frac{\sum_{i=1}^{N} FI(t,z)}{N} \tag{4}$$

Where FI is from (3) and N is the number of diagnostic days.

All FI diagnostics were computed from grids generated by NCEP's post processing package. These grids have a 1° X 1° horizontal resolution and have 26 vertical isobaric surfaces. None of the fields were smoothed during plotting. The forecast diagnostics for this paper were also terminated at 168 hours to concentrate on the shorter term forecast impacts.

Chapter 4: WindSat Polarimetric Microwave Observations Improve Southern Hemisphere Numerical Weather Prediction

4.1 Introduction

Measurement of global ocean surface wind vectors is important for short and medium term weather forecasting, ocean forecasting, the issuing of timely warnings and for the climate record. As a result WindSat, a space-based multi-frequency polarimetric microwave radiometer (Gaiser et al., 2004), was developed by the Naval Research Laboratory for the U.S. Navy and the National Polar-orbiting Operational Environmental Satellite System (NPOESS) Integrated Program Office (IPO). It was designed to demonstrate the capability of polarimetric microwave radiometry to measure ocean surface wind vectors from space. Similar technology has been planned for the NPOESS Conical Microwave Imager Sounder (CMIS) instrument. The Coriolis/WindSat satellite was launched on 6 January 2003 into a 830-km 98.7-degree orbit. It was designed for a three-year lifetime.

4.2 The WindSat Radiometer

The WindSat radiometer has polarimetric channels at 10.7, 18.7 and 37.0 GHz and dual-polarization (vertical and horizontal) channels at 6.8 and 23.8 GHz. These provide information related to surface wind vectors as well as sea surface temperature,

atmospheric water vapor, integrated cloud liquid water and rain rate over the ocean. Measurements of the modified stokes vector, which includes the vertical and horizontal polarizations and the third and fourth stokes parameters, provides sufficient information to retrieve the ocean surface wind vector (Bettenhausen et al., 2006). The 6.8GHz dual-polarized channel is more sensitive to sea surface temperature (SST) than to winds and is used to determine effects due to variations in SST. Similarly, the 23.8GHz dual-polarized channel is highly sensitive to atmospheric water vapor. Consequently, measurements at 23.8 GHz help determine the effects of atmospheric attenuation on radiation from the ocean surface. The WindSat instrument characteristics are summarized in Table 4.1.

Table 4.1. WindSat instrument characteristics

Frequency (GHz)	Polarization	Bandwidth (MHz)	Incidence Angle (deg)	Spatial Resolution (km)
6.8	V. H	125	53.5	40x60
10.7	V, H, ±45, L, R	300	49.9	25x38
18.7	V, H,± 45, L, R	750	55.3	16x27
23.8	V,H	500	53.0	12x20
37.0	V, H, ±45, L, R	2000	53.0	8x13

The ocean surface wind vectors used in this study have been determined using a non-linear iterative optimal estimation method (Rodgers, 2000). The method also provides sea surface temperature, total water vapour, and cloud liquid water. Details of the scheme which uses a one layer atmospheric model and a sea surface emissivity model is found in Bettenhausen et al., (2006). The Environmental Data Records (EDRs) generated by this scheme have been put into BUFR format at NCEP in preparation for operational use.

4.3 Data selection and thinning

In relation to data selection, the wind vector ambiguity issue was addressed by selecting the WindSat wind vector closer to the NCEP model wind field which was used in the ambiguity selection routine in generating the EDRs. This approach is anticipated to change as newer versions of the wind generation algorithm have less dependence on the model fields. Data thinning was achieved using a similar technique to that used operationally for QuikSCAT wind vectors, namely using super-obs. Tests were run to determine whether one degree or one- half degree latitude, longitude averaging boxes were more effective and it was found that the one degree boxes gave the best forecast result. In terms of quality control an accurate land sea mask was used to eliminate any data that could be contaminated due to land effects. In addition the retrieval status of the records used had to be flagged ok, and the confidence status of the record had to indicate there were no problems in the retrieval process including those caused by rain, ice or land contamination. A gross error check was also constructed for the data. Information from N. Bettenhausen, A. Gaiser and J. Goerss, (Private Communications) assisted in the establishment of quality control criteria.

4.4 Data assimilation

The effect of adding WindSat Version.2 wind vectors to the NCEP operational forecast system, was gauged using a T254 64 level version of the Global Forecast System

(Version, November, 2005). The satellite data used operationally with the NCEP Global

Forecast System in 2004 is shown in Table 4.2.

Table 4.2: The satellite data used operationally within the NCEP Global Forecast System in 2004

HIRS sounder radiances	TRMM precipitation rates
AMSU-A sounder radiances	ERS-2 ocean surface wind vectors
AMSU-B sounder radiances	Quikscat ocean surface wind vectors
GOES sounder radiances	AVHRR SST
GOES, Meteosat	AVHRR vegetation fraction
atmospheric motion vectors	AVHRR surface type
GOES precipitation rate	Multi-satellite snow cover
SSM/I ocean surface wind speeds	Multi-satellite sea ice
SSM/I precipitation rates	SBUV/2 ozone profile and total ozone

In the first two experiments a *Control* data base was established which contained

all *operational data without QuikSCAT data.* The forecast performance using the

Control data base was compared to that of the same database with *QuikSCAT* data, in a

series of experiments to gauge the impact of QuikSCAT data over the Southern

Hemisphere. In a second experiment, forecasts from the *Control* data base were

compared to those generated using the control data base plus *WindSat* data. In a final

series of experiments forecasts from the full *operational data base* (which included

(QuikSCAT data) were compared to forecasts using the full *operational data base plus*

WindSat data.

4.5 The forecasts

In each of these experiments the NCEP operational systems was run from the 1 of January to 15 of February 2004. The forecast model had a resolution T254 with 64 vertical levels. The analysis used was the NCEP operational SSI 3D-VAR. (Derber and Wu, 1998; Derber et al., 2003).

In the first series of experiments, forecasts from the *Control* which contained the operational data base without QuikSCAT data, were contrasted with forecasts using the full operational data base plus *QuikSCAT* data. The results for this experiment are summarized in Fig. 4.1 where the 500 HPa geopotential Anomaly Correlations for the *Control* and the *QuikSCAT* runs are recorded. It can be seen, as in past studies (see for example, Yu and Gemmill, 2004), QuikSCAT has had a positive influence on Southern Hemisphere forecasts for the NCEP system.

In a second series of experiments, (*Control*) forecasts based on the operational data base without QuikSCAT data, were contrasted with forecasts from the operational system without QuikSCAT data but with the addition of *WindSat* data (*WindSat*). It can be seen in these experiments (Fig. 4.2), the addition of WindSat data has had a positive overall impact on the forecast skill, but of lesser magnitude than that measured for QuikSCAT data.

In a final series of experiments forecasts using the full operational data base which includes QuikSCAT data (*Ops*) were contrasted with those obtained from the

operational data base including QuikSCAT data and with the addition of *WindSat* data (*Ops+WindSat*). It can be seen from the Southern Hemisphere 500HPa Geopotential Anomaly Correlation curves shown in Fig. 4.3, that for the period studied, WindSat has had a modest but positive impact on the forecast.

The results for including WindSat data in the operational data base for the Northern Hemisphere, (Fig 4.4) are similar to those for the Southern Hemisphere and are included here for completeness.

4.6 Conclusions

This is any early report of the potential benefit of WindSat polarimetric data to operational numerical weather forecasting. For the period 1 January to 15 February 2004, the impact of WindSat surface wind vectors (NRL, Version.2 EDRs) obtained from polarimetric microwave radiometer observations, on the NCEP operational forecast system has been assessed. It was found, for the period studied and over the Southern Hemisphere, that the WindSat data had a positive impact on the Global Forecast System when added to the full operational data base without QuikSCAT data. It was also found for the period studied and over the Southern Hemisphere that the WindSat data had a modest positive impact when added to the full operational data base with QuikSCAT data. For the period studied and over the Southern Hemisphere the impact of WindSat data was not as large that of QuikSCAT, it was also found however, that WindSat and QuikSCAT together had larger impact that either by themselves. For completeness the

benefit to Northern Hemisphere GFS forecasts from including WindSat data in the operational data base was also shown.

In conclusion, the potential benefit of using polarimetric microwave observations to estimate surface wind vectors for operational application in the Southern Hemisphere has been shown. These vectors could be estimated through a space based imaging and sounding payload with polarimetric capability such as the Conceal Microwave Imager/ Sounder (CMIS). This polarimetric information is not available through current microwave imagers and sounders (other than WindSat), however some current instruments do enable surface wind speed estimates (eg. in the case of the Spectral Sensor Microwave/Imager (SSM/I)) for operational analysis and forecasting. In terms of future directions for these studies, a real time experiment during the Northern Hemisphere summer is well underway. This will later use wind vectors generated with newer algorithms, less dependent on the model first guess fields. An experiment involving the direct assimilation of radiances is also planned. It is anticipated these studies will allow these data to be transitioned to operational use for the JCSDA Partners.

S. Hemisphere   500 hPa AC Z   1 Jan - 15 Feb '04
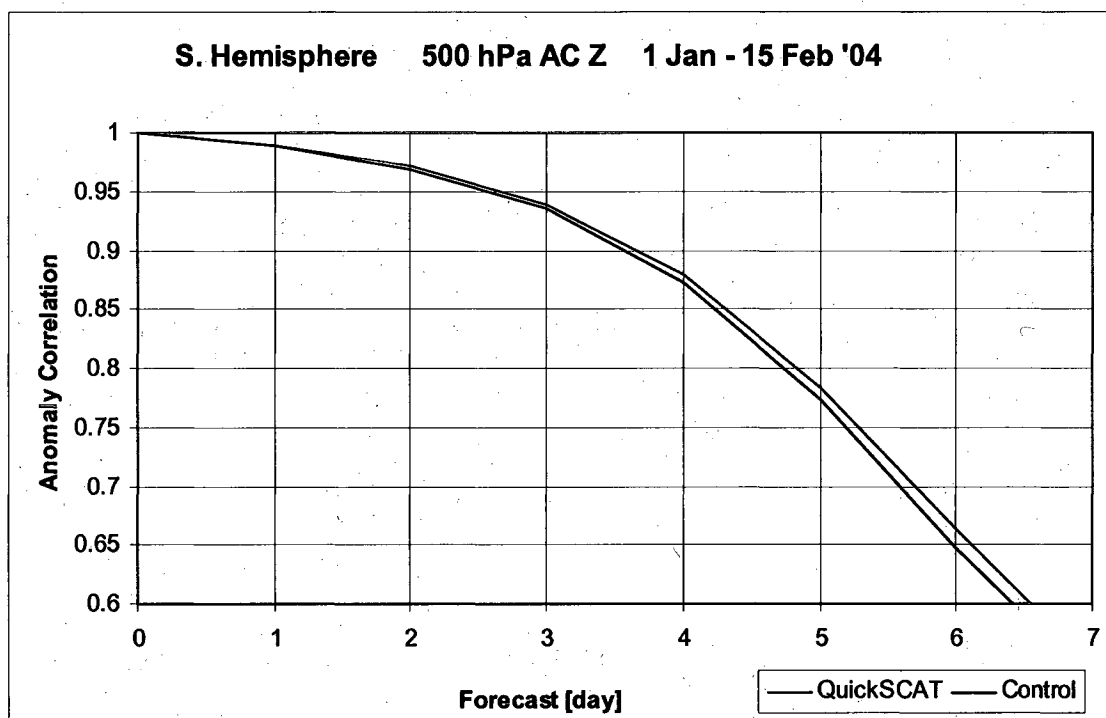
Figure 4.1. The 500HPa Geopotential Anomaly Correlations versus forecast period for GFS forecasts using the operational data base without QuikSCAT data (Control) and using the operational database including QuikSCAT data (QuikSCAT) over the Southern Hemisphere.
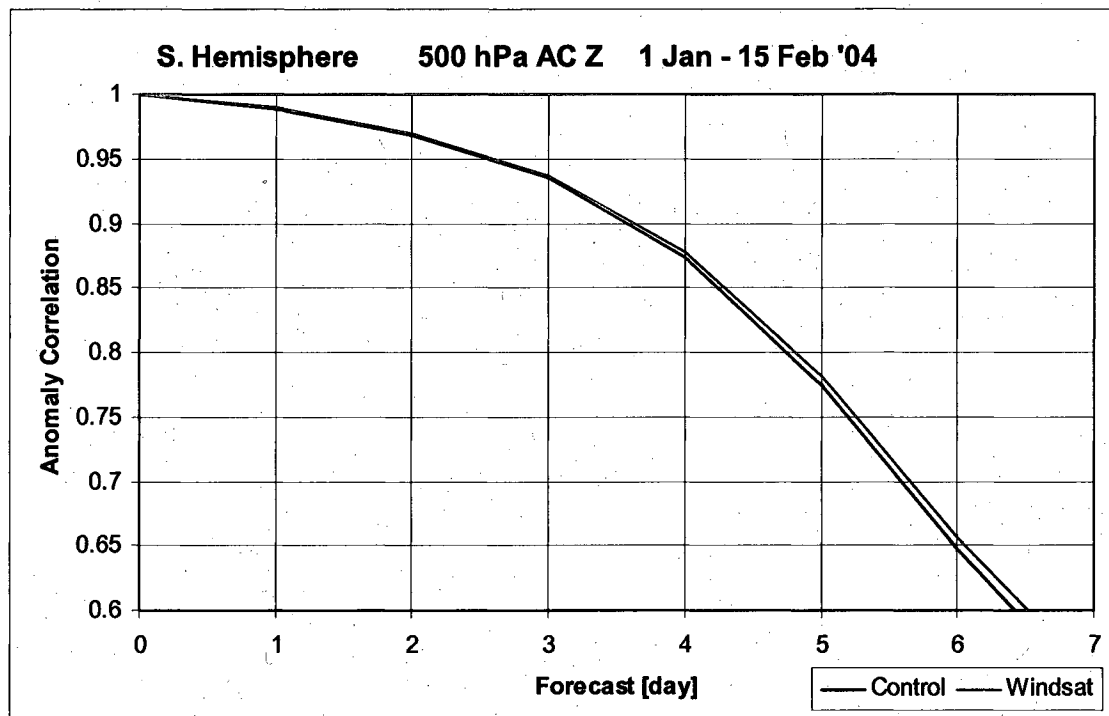
Figure 4.2. The 500HPa Geopotential Anomaly Correlations versus forecast period for GFS forecasts using the operational data base without QuikSCAT data (Control) and using the operational database without QuikSCAT data but with WindSat data (WindSat) over the Southern Hemisphere.
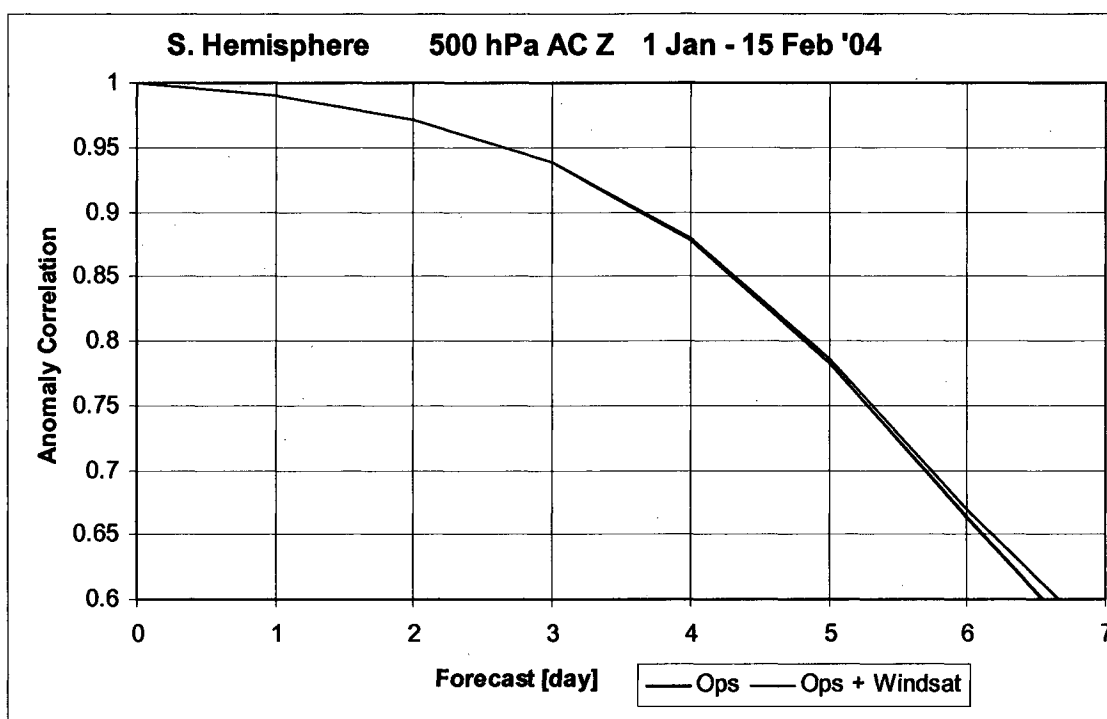
Figure 4.3. The 500HPa Geopotential Anomaly Correlation versus forecast period for GFS forecasts using the operational data base with QuikSCAT data (Ops) and for the operational data base with QuikSCAT data and WindSat data (WindSat) over the Southern Hemisphere.

N. Hemisphere   500 hPa AC Z   1 Jan - 15 Feb '04

(Graph: Anomaly Correlation vs Forecast [days], with legend "Ops" and "Ops + Windsat")
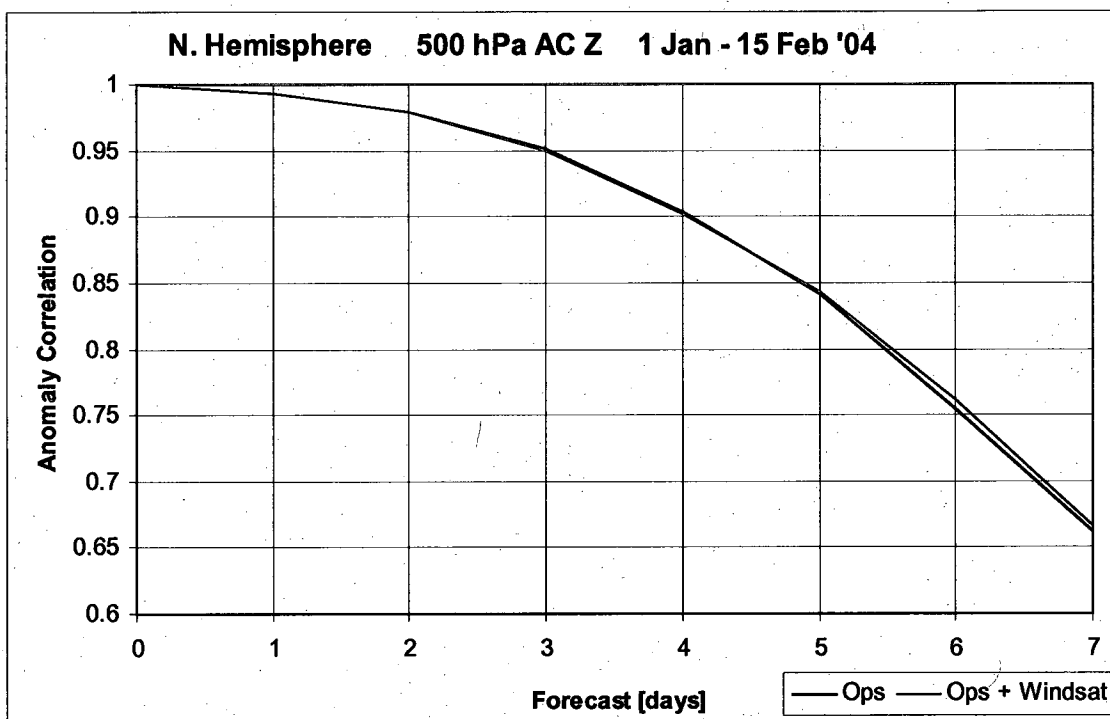
Figure 4.4. The 500HPa Anomaly Correlation versus forecast period for GFS forecasts using the operational data base with QuikSCAT data (Ops) and for the operational data base with QuikSCAT data and WindSat data (Ops + WindSat) over the Northern Hemisphere.

Chapter 5: A Two-Season Impact Study of the WindSat Surface Wind Retrievals in the NCEP Global Data Assimilation System

5.1 Introduction

Sea surface wind vectors have been estimated with active remote sensing instruments, such as QuikSCAT (Yu and McPherson 1984), and have been proven to have a positive impact on forecasts. Passive polarimetric microwave radiometry is being introduced as an alternative vector wind measurement approach to active sensors (e.g. QuikSCAT) and other instruments. WindSat is a space-based multi-frequency polarimetric microwave radiometer (Gaiser et al., 2004), that was developed by the Naval Research Laboratory (NRL) for use by the U.S. Navy and the National Polar-orbiting Operational Environmental Satellite System (NPOESS) Integrated Program Office (IPO).

One of the WindSat missions was to demonstrate spaceborne remote sensing of ocean surface wind vectors (speed and direction). Wind roughening of the ocean surface causes an increase in the microwave radiation emitted by the water's surface. Wind direction measurement with polarimetric instruments, which sense the polarity of light, also demonstrate how ocean surface properties change with wind and boundary layer conditions. WindSat also aids in forecasting short-term weather events, issuing timely warnings, and gathering general climate data. WindSat wind vectors have been proven to have a positive impact on forecasts in the Southern Hemisphere (Le Marshall et al.,

2006).

The paper is structured as follows. Section 2 briefly describes background information related to the WindSat instrument and the National Centers for Environmental Prediction (NCEP) Global Data Assimilation/Global Forecast System (GDAS/GFS) version used for this study. Section 3 discusses the diagnostic tools used to evaluate the forecast impacts. Section 4 presents the results for this forecast impact study through 7 days of model forecasts. Section 5 summarizes the overall experiment results.

5.2 Background

(a) WindSat

WindSat is on the Coriolis satellite which was launched on 6 January 2003. Coriolis was designed to have a three-year life span. Coriolis is in a 98.7^0 inclined orbit at an altitude of about 830km and with a local ascending node time near 1800 UTC. It completes about 14 orbits per day with each orbit requiring 102 minutes. WindSat records data on both the forward (fore) and back (aft) side of each spin of the conically scanning feedhorn structure. The on-Earth fore- and aft-viewing swath width encompasses 1025 and 350 km, respectively, as the sensor's conical scan spins counterclockwise (Gaiser et al., 2004).

The WindSat radiometer has polarimetric channels at 10.7, 18.7, and 37.0 GHz and dual-polarization (vertical and horizontal) channels at 6.8 and 23.8 GHz. These provide information related to surface wind vectors, sea surface temperature, atmospheric water vapor, integrated cloud liquid water and rain rate over the ocean. Measurements of

the modified Stokes vector provide sufficient information to retrieve the ocean wind vector. The 6.8 GHz dual-polarized channel is sensitive to sea surface temperature (SST) and is used to determine effects due to variations in SST. Similarly, the 23.8 GHz dual-polarized channel is highly sensitive to atmospheric water vapor. Consequently, measurements at 23.8 GHz help determine the effects of atmospheric attenuation on radiation from the ocean surface. The WindSat instrument channel characteristics are summarized in Table 1.

NRL has developed a nonlinear iterative algorithm for simultaneous retrieval of sea surface temperature, columnar water vapor, columnar cloud liquid water, and the ocean surface wind vector from WindSat measurements. The algorithm uses a physically based forward model for estimating the WindSat brightness temperature. From the measurements of the modified Stokes vector, which includes the vertical and horizontal polarizations and the third and fourth Stokes parameters, wind speed and direction can be retrieved (Bettenhausen et al., 2006). The ocean surface wind vectors have been determined using a non-linear iterative optimal estimation method. This method uses a one layer atmospheric and a sea surface emissivity model which is explained in Bettenhausen et al. (2006). WindSat wind speed retrieval processing also uses a median filtering technique to smooth the final wind field and applies empirical corrections to the vertically and horizontally polarized brightness temperature to the physically based model (Bettenhausen et al., 2006).

Various improvements to the WindSat wind vector retrieval algorithm were incorporated to derive the wind vectors (version 2) and used to generate the data in this

study (Peter Gaiser, personal communication). The wind data were delivered as Environmental Data Records (EDRs) and put into Binary Universal Form for the Representation of meteorological data (BUFR) format at the National Oceanic and Atmospheric Administration's (NOAA) NCEP in preparation for operational use.

(b) Global Data Assimilation System

A January 2007 version of the Gridpoint Statistical Interpolation (GSI) routine and GFS were used for these observing system experiments. The NCEP assimilation system consists of a first or "early" cycle with a 2.5 hour cut-off. The analyses for this cycle are centered on 0000, 0600, 1200. and 1800 UTC and are followed by a 384 hour forecast. Consistent with the operational GDAS/GFS, a model resolution of T382L64 (i.e., spectral triangular truncation 382 with 64 layers) is used through 168 hours. For this study, only the 0000 UTC forecasts were run. The analysis is repeated later (+6 hrs) to provide the "final" analysis for the six hour forecast for the next early cycle first guess. This "final" analysis includes data that had missed the previous "early" data cut-off.

The vertical domain of GFS model ranges from the surface to approximately 0.27 hPa and is divided into 64 unequally spaced sigma levels with enhanced resolution near the bottom and top of the model domain. There are 15 layers below 800 hPa and 24 layers above 100 hPa. The time integration is leapfrog for nonlinear advection terms and semi-implicit for gravity waves and the zonal advection of vorticity and moisture. Comprehensive documentation of the GFS was completed by the National Meteorological Center (NMC) (now NCEP) Development Division (1988) and can be

found online at http://wwt.emc.ncep.noaa.gov/gmb/wd23ja/doc/web2/tocold1.html. Subsequent model developments after completion of the above documentation have been summarized by Kanamitsu (1989), Kalnay (1990), and Kanamitsu et al. (1991). More recent updates to the radiation, surface layer, vertical diffusion, gravity wave drag, convective precipitation, shallow convection and non-convective precipitation can be found at http://sgi62.wwb.noaa.gov:8080/research/SONGYU/doc/physmrf1.html. The most recent description of the GFS atmospheric model (2003) is in NCEP Office Note No. 442. A summary of GFS changes and references up to and past the dates of this study are available in an "updates" log of changes online at both http://www.emc.ncep.noaa.gov/gmb/moorthi/gam.html and http://www.emc.ncep.noaa.gov/gmb/STATS/html/model_changes.html.

The GDAS utilizes a three-dimensional variational data assimilation (3DVAR) scheme to obtain an optimum initial state that fits the available observations and a short-range forecast (background). In this study, we use NCEP's GSI (Derber et al. 1991; Wu et al. 2002; Derber et al. 2003) 3DVAR system. With this type of analysis system, the incorporation of radiances directly into the analysis and assimilation system has become practical. The analysis is a three-dimensional retrieval of mass, momentum, and moisture fields derived from all available data including the radiances (Caplan et al. 1997). The GSI uses a thinning routine which identifies the optimal radiance profile for each satellite sensor type (AMSU, HIRS, MSU, etc.) in a pre-designated grid box. The optimal radiance profile is determined by its departure from the model background temperature, distance from the center of the grid box, temporal departure from the assimilation time,

and surface features (ocean, land, and ice).

5.3 Experimental design

The complete NCEP operational database of conventional and satellite data was used for this experiment in a manner reflective of the real-time data cut-off constraints for the early and late assimilation cycles produced at NCEP. The conventional data used included rawinsonde temperature, relative humidity and wind, aircraft observations of wind and temperature; land surface reports of surface pressure; and oceanic reports of surface pressure, temperature, horizontal wind and specific humidity. The satellite observations used in this work include operational Advanced Television Infrared Observation Satellite (TIROS-N) (NOAA 2000), Operational Vertical Sounder (TOVS) (Smith et al. 1979) radiances from the High Resolution Infrared Radiation Sounder (HIRS), the Microwave Sounding Unit (MSU) (Spencer and Christy 1990), the Advanced Microwave Sounding Unit (AMSU-A and AMSU-B) sensors (NOAA 2005), ozone information from the Solar Backscatter Ultraviolet (SBUV) sensors (Miller et al. 1997); Defense Meteorological Satellite Program (DMSP) Special Sensor Microwave Imager (SSM/I) surface wind speed (Alishouse et al. 1990); derived surface winds from QuikSCAT (Yu and McPherson 1984); atmospheric motion vectors from geostationary satellites (Velden et al. 1997; Menzel et al. 1998). Keyser (2001a, 2001b, 2003) provides an overview of data types provided to NCEP on a daily basis and used operationally for the experiments of this study. The conventional and satellite data used in these experiments are summarized in Tables 2 and 3, respectively.

(a) Data thinning

Data thinning was achieved using a technique similar to that used operationally for QuikSCAT wind vectors, namely the use of "super observations" (or "super-obs"). A super-ob is the average of all the observations in each 1°x1° thinning box with the averaged vector located in the center of the box. Observations which have a low confidence (determined by NRL) due to rain, ice, or land contamination are not used in the super-obing. Tests were run to determine whether one degree or one- half degree latitude, longitude averaging boxes were more effective. It was found that overall the one degree boxes gave the best forecast results. Two seasons were used for this study; 15 September to 30 October 2006 and from 15 February to 30 March 2007. The first two weeks of each time period were removed from these results to allow the assimilation system and forecast model to adjust to the new data.

(b) Quality Control

Most of the Quality Control (QC) of the WindSat data was accomplished in the retrieval process. Observations that fail the retrieval process or are flagged for rain, land, sun glint, Radio Frequency Interference (RFI), or sea ice contamination were flagged in the EDRs and omitted from the super-obs.

The preliminary statistical results from the 20-day test experiment indicated that there were problems associated with high wind speed. This contamination suggested there were still quality control problems with the observations even after the quality control

procedures were performed during the retrieval process. It is essential to investigate additional quality control procedures before the WindSat data are assimilated to the GFS system. Bases on the preliminary statistical results, a series of additional quality control procedures were added within GDAS/GFS. Additional quality control procedures were added within GDAS/GFS. Observations not within +/- 3 hours of the synoptic time and observations near coasts were not used. If the absolute value of the super-ob'd wind component differs from the corresponding background wind by more than $6ms^{-1}$ or the wind speed was not between $4ms^{-1}$ and $20ms^{-1}$, the super-ob wind vector removed.

(c) Diagnostics

Several diagnostics were performed using the control and WindSat experiment analyses and forecasts. The anomaly correlation statistics were performed using the traditional NCEP algorithms (NWS 2006) which are commonly used by other NWP centers worldwide. The computation of all anomaly correlations for forecasts produced by the GFS are completed using code developed and maintained at NCEP. NCEP (NWS 2006) provides a description of the method of computation while Lahoz (1999) provides an interpretation for the anomaly. The reanalysis fields from the National Center for Atmospheric Research (NCEP/NCAR) (Kistler 2001) are used for the climate component of the anomaly correlations. This reanalysis was run at a resolution of T62L28. The output grids were reduced to 2.5° x 2.5° horizontal resolution on mandatory rawinsonde levels. To calculate anomaly correlations the output grids from the control and both experiments were reduced to this 2.5° x 2.5° horizontal resolution using the GFS post-

processor. The fields being evaluated using anomaly correlations are truncated to only include spectral wave numbers 1 through 20. These fields are also limited to the zonal bands of 20°-80° in each hemisphere and a tropical belt within 20° of the equator (20°N to 20°S).

Another diagnostic used here is the modified forecast impact (FI), which is discussed further by Zapotocny et al. (2005). For this study, a series of two-dimensional FI results are presented as the positive/negative impact provided by the experiment of a particular data type. The geographic distributions of FI are shown in section 4.b and are evaluated using:

$$FI(x,y) = 100 \times \{[\sqrt{\frac{\sum_{i=1}^{N}(C_i - A_i)^2}{N}} - \sqrt{\frac{\sum_{i=1}^{N}(E_i - A_i)^2}{N}}]/\sqrt{\frac{\sum_{i=1}^{N}(E_i - A_i)^2}{N}}\} \quad (1)$$

The variables C and E are the control and experiment forecasts, respectively. The variable A is the 00-hr GDAS experiment analysis containing all data types which is valid at the same time as the forecasts. N is the number of diagnostic days.

The area ratio weights the grid points to account for the reduction in area as the grid boxes approach the poles. The area ratio weighting is defined as:

$$A_i' = A_i \times \frac{\sin(\phi_i + \frac{\Delta}{2}) - \sin(\phi_i - \frac{\Delta}{2})}{2\sin(\frac{\Delta}{2})} \quad (2)$$

Where ϕ is the latitude of grid point i and Δ is north/south resolution of the grid box. The numerator is the relative size of the grid box. The denominator is the relative size of a grid box at the equator.

The vertical cross section plots shown in section 4.c are evaluated using:

$$FI(t,z) = 100 \times \left[\frac{\sqrt{\frac{\sum_{i=1}^{X}(C_i' - A_i')^2}{X}} - \sqrt{\frac{\sum_{i=1}^{X}(E_i' - A_i')^2}{X}}}{\sqrt{\frac{\sum_{i=1}^{X}(E_i' - A_i')^2}{X}}} \right] \qquad (3)$$

Where X is the number of horizontal grid points. A', C' and E' are the area ratio weighted values of A, C and E defined in (1). The first term on the right enclosed by parentheses in (1) and (3) can be considered the error in the denied experiment. The second term enclosed by parentheses in (1) and (3) can be considered the error in the control forecast. Dividing by the error of the control forecast normalizes the results. Multiplying by 100 provides a percent improvement/degradation with respect to the RMS error of the control forecast. A positive forecast impact means the WindSat forecast compares more favorably to its corresponding analysis than the control.

The FI is then averaged over the number of days by using:

$$F_t = \frac{\sum_{i=1}^{N} FI(t,z)}{N} \qquad (4)$$

Where FI is from (3) and N is the number of diagnostic days.

All FI diagnostics were computed from grids generated by NCEP's post processing package. These grids have a 1° x 1° horizontal resolution on 26 vertical isobaric surfaces. None of the fields were smoothed during plotting. The forecast diagnostics for this paper were also terminated at 48 hours to concentrate on the short

term forecast impacts.

5.4 Results

Assimilation experiments were conducted to test and compare the attributes of using the WindSat data. Forecast impact comparisons are presented from assimilating WindSat data to a benchmark or control experiment. The control contains all the operational data used during the period and includes all of the real time data cutoff requirements. The impact of assimilating the WindSat data on the quality of forecasts made by the GFS for two time periods are explored in detail. The first time period covers 1 to 31 October 2006, the second covers 1 to 30 March 2007. The selection of these time periods enables the diagnostics to sample two seasons in each hemisphere. The fields diagnosed consist of geopotential height, temperature, and wind speed. Underground grid points on isobaric surfaces intersecting the earth's surface are not included in the evaluation.

(a) Data fitting statistics

Figure 5.1 displays a comparison of the bias, standard deviation, normalized observation wind speed histogram and wind speed innovation histogram for WindSat. Figures 5.1(a) – (d) show the analysis statistics for October and (e) – (h) show the analysis statistics for March. While there are large biases and standard deviations for observed wind speeds greater than $20ms^{-1}$, these observations account for less than 5% of the total number of observations (Figs. 5.1d and 5.1g), thus large biases are not a major

concern. Before the WindSat experiment began, a 20-day test run was performed. Based on the preliminary statistical results of this test, observed wind speeds that are greater than 20ms^{-1} have been tossed. Figure 5.1a and 5.1e show that there are large biases and standard deviations for observed wind speeds greater than 20ms^{-1} and in some cases biases and standard deviation for observation minus analysis (O-A) are even higher for observation minus background (O-B), these observations are rejected by the assimilation system. In the GSI assimilation system, there are three outer iteration loops; observations which passed the first outer loop may still be rejected in the second outer loop. The final analyses are results from the third outer loop. Figures 5.1c and 5.1g show that the majority of the counts are located within the wind speed range of 5-10 ms^{-1}. In Figs. 5.1d and 5.1h, the green curve shows the O-B and red curves represents O-A. The O-B histograms are skewed to the right for both seasons which suggests WindSat speeds are faster than the model background.

Figure 5.2 displays the geographic distribution of bias and standard deviation for wind speed at 10 meter near the surface for both O-B and O-A for October (a-d) and March (e-h). The largest biases with respect to the background are found over the central Pacific and Indian Ocean (Figs. 5.2a and 5.e). As expected the biases are significantly reduced in most regions after assimilating the data (Fig. 5.2b and 5.2f) but larger biases appear in the Southern Hemisphere near Antarctica. The standard deviations of O-B are quite similar for October (Fig. 5.2c) and March (Fig. 5.2g), large standard deviations are found in the tropical western Pacific and near Antarctica. Again, after WindSat data have been assimilated, decreases in the standard deviation are realized.

(b) Anomaly Correlations

Figure 5.3a and 5.3c present the mid-latitude 500 hPa Northern Hemisphere geopotential height anomaly correlations for days 0 to 7 for the WindSat and control simulations during October 2006 and March 2007 respectively. Figure 5.3b and 5.3d show the 500 hPa Southern Hemisphere geopotential height anomaly correlations for days 0 to 7 for the WindSat and control simulations during October 2006 and March 2007 respectively. The blue line is the control simulation which closely replicates NCEP operations and includes all data routinely used by the GDAS/GFS. The magenta line is the anomaly correlation diagnosed from the WindSat simulation. In these types of experiments, the larger the separation between anomaly correlations for the experiment and the control, the greater the impact the WindSat data has on the simulation. The results indicate that the control simulation anomaly correlations are close to the WindSat experiment anomaly correlations until day 6 then the improvements in the WindSat experiment become greater for both seasons and in most of the cases. The greatest improvement in the anomaly correlations are achieved in the Northern Hemisphere (500 hPa) during March 2007.

(c) Geographic distributions of forecast impacts

All the forecast impacts shown in this paper have been tested as significant differences between the control and experiment. The differences in the temperature and wind fields shown here are statistically significant with a confidence interval of 99% or

greater for forecasts as long as 36 hours. Figure 5.4 displays geographic distributions of average forecast impact, determined from using equation (1), for the 10m wind speed for October 2006 at forecast hours (a) 6, (b) 12, (c) 24, and (d) 48 and for March 2007 at forecast hours (e) 6, (f) 12, (g) 24, and (h) 48. The range of FI is from -50 to 100 percent. The 6-h results (Fig. 5.4a) show the largest FIs in Africa, Western Pacific, South America and Australia. By 12 hours (Fig. 5.4b), the FIs in the South Eastern Pacific are reduced, with the largest FI still realized over Africa, Australia and South America. The FIs are generally small by 24 hours (Fig. 5.4c) and become mostly neutral by 48 hours (Fig. 5.4d). Figure 4e-h presents the March 2007 WindSat 10m wind speed FIs at forecast hours 6, 12, 24, and 48 respectively. Consistent with the results in October, large positive FIs are seen over Africa, Australia, and South America at 6 hours (Fig. 4e), except over the Western Pacific. By 12 hours (Fig. 5.4f), the largest FIs are still found over Africa. Again, the FIs are generally small by 24 hours (Fig. 5.4g) and become mostly neutral by 48 hours (Fig. 5.4h).

The FIs for 500 hPa wind speed during October 2006 and March 2007 are shown in Figure 5.5a-d and e-h respectively. The greatest FIs are realized in the tropics for both seasons as shown by the 6 and 12 hour forecasts. By 24 hours (Fig. 5.5c and Fig. 5.5g), the FIs are reduced with small positive impacts still seen in the tropical region. By 48 hours (Fig. 5.5d and Fig. 5.5h) the FIs are mostly neutral with some small positive impacts remaining. Comparing Fig. 5.4 and 5.5 suggests that the WindSat data have a greater positive impact on the wind speed field through the 24-h forecast at 500hPa than at 10m.

Figure 5.6 presents the temperature geographic distribution of FI at 1000hPa for the two seasons at forecast times 6, 12, 24 and 48 hours. All points diagnosed as underground, were not used and are shaded black. The 6-h results (Fig. 5.6a and e) show the largest positive FIs in the tropics. Small areas of negative FI are noted near Antarctica during both seasons. After 12 hours, large areas of positive FIs are still realized over the Western Pacific and South Atlantic (Fig. 5.6b and f). Similar to the wind FIs at 48 hours (Fig. 5.6d and h), the FIs are mostly neutral with small areas of positive and negative impact remaining.

The FIs for temperature at 500hPa during both periods are shown in Figure 5.7. Similar to the 1000hPa temperature FIs, the largest impacts are found in tropics in the 6-h forecasts for both seasons (Fig. 5.7a and Fig. 5.7e). There is a marked decrease in forecast impact by 12 hour (Fig. 5.7b and Fig. 5.7F) with all of the largest impacts still realized in the tropics. The FIs are generally small by 24 hours (Figs. 5.7c and g) and becomes mostly neutral by 48 hours (Figs. 5.7d and h). Comparing Figs. 5.6 and 5.7 indicates that the WindSat data have a markedly more positive impact in magnitude on the temperature field through the 24-h period at 500hPa than at 1000hPa.

One potential explanation for why the large impacts are seen in the tropics at 500hPa for both wind speed and temperature fields is due to the deep convection associated with the convective scheme used in the GFS model which is based on Arakawa and Schubert (1974) scheme, in which mass fluxes induced in the convective updraft and the downdraft are allowed to transport momentum. The momentum exchange is calculated through the mass flux formulation in a manner similar to that for heat and

moisture. Fig. 5.8 shows the geographic distribution of Outgoing Longwave Radiation

(OLR) [w/m^2] mean using NCEP/NCAR reanalysis for the month of (a) October 2006,

and of (c) March 2007. Fig. 5.8a indicates that there is deep convection located in eastern

Pacific north of Australia, and north of Africa along the tropics. Fig. 5.8c shows similar

patter. The deep convection along the tropics is consistent with the largest FI which is

along the tropics for 500hPa wind speed field (Fig. 5.5a and Fig. 5.5e). Because of the

deep convection transport the momentum upward, the surface wind analysis increment

information propagates upward into the middle and upper-troposphere within the first 6

hours. Another approach is to look at the convective precipitation plots, geographic

distribution of convective precipitation scale of 10^{-9} [kg/m^2] from 0-6hr forecast of

WindSat assimilation for the month of (c) October 2006, and of (d) March 2007. It is

clear that the convective precipitation band is realized along tropics for both seasons, that

also explains why the largest FIs are seen along the tropics as early as 6 hour in the

middle and upper-troposphere. The 6-12hr, 18-24hr, 42-48hr convective precipitation

plots have similar pattern as the 0-6hr ones, they are not shown here.

Figure 5.9 presents the vertical time series of the horizontally averaged Forecast

Impacts from both seasons. This figure was computed using equation (2) and area

weighted using equation (3). Forecast impacts from the wind speed (Fig 5.9a and c), and

temperature (Fig 5.9b and d) fields are shown for both seasons. Inspection of the plots

reveals that the largest impacts are at the 500hPa level and is consistent with the

geographic Forecast Impacts in Fig. 5.5. Large impacts are also shows at 100hPa. Similar

patterns are found in the temperature fields in Fig. 5.9b where the greatest Forecast

Impacts are again at 500 and 100hPa. All four panels display a systematic decrease of FI with time. A final point about the vertical time series of Forecast Impact results is that the 6-h temporal resolution of the GFS archive used for these experiments is not adequate to resolve the rapid decrease in forecast impact that occurs in the first 12 h of these simulations.

5.5 Summary

Observing system experiments were conducted during two seasons to quantify the impacts of assimilating the surface wind retrievals from the WindSat microwave sensor on the Coriolis satellite. A January 2007 version of the NCEP GDAS/GFS was used for the assimilation system and forecast model. These experiments were conducted at the NCEP operational resolution of the time (T382 with 64 layers) and used the NCEP operational observation database.

Several verification techniques were used to measure the impact the WindSat wind retrievals made to the forecast. These techniques included: anomaly correlations, geographical forecast impact and vertical time series of forecast impact.

The results from the anomaly correlation show neutral to modest positive impacts at mid- latitudes in both seasons for most of the cases. Results from a modified forecast impact calculation reveals positive forecast impacts occurred in the wind, temperature through 48 hours. The greatest forecast impacts occurred in the tropics and at 500 hPa which appears to be attributable to the deep upward momentum transport in tropical

convection. It was also found in this study that small, positive forecast impacts are noted at all levels of the GFS through 48 hours.

Table 5.1 WindSat Characteristics

Frequency (GHz)	Polarization	Bandwidth (MHz)	Incidence Angle (deg)	Spatial Resolution (km)
6.8	V. H	125	53.5	40x60
10.7	V, H, ±45, L, R	300	49.9	25x38
18.7	V, H,± 45, L, R	750	55.3	16x27
23.8	V,H	500	53.0	12x20
37.0	V, H, ±45, L, R	2000	53.0	8x13

Table 5.2 In-Situ data used within the NCEP Global Data Assimilation System for this study. Mass observations (temperature and moisture) are shown in the left column and wind observations are shown in the right column.

Rawinsonde temperature and humidity	Rawinsonde u and v
AIREP and PIREP aircraft temperatures	AIREP and PIREP aircraft u and v
ASDAR aircraft temperatures	ASDAR aircraft u and v
Flight-level reconnaissance and dropsonde temperature, humidity and	Flight-level reconnaissance and dropsonde u and v
MDCARS aircraft temperatures	MDCARS aircraft u and v
Surface marine ship, buoy and c-man temperature, humidity and station	Surface marine ship, buoy and c-man u and v
Surface land synoptic and Metar temperature, humidity and station	Surface land synoptic and metar u and v
Ship temperature, humidity and station pressure	Wind Profiler u and v
Pibal u and v	NEXRAD Vertical Azimuth Display u and v

Table 5.3 Satellite data used within the NCEP Global Data Assimilation System for this study.

HIRS sounder radiances	SBUV ozone radiances
AIRS radiances	QuikSCAT surface winds
AMSU-A radiances	GOES atmospheric motion vectors
AMSU-B radiances	Atmospheric motion vectors from GMS-5 until May 2003 than GOES-9
TRMM precipitation rate	METEOSAT atmospheric motion vectors
SSM/I precipitation rate	SSM/I surface wind speed
WindSat surface winds	
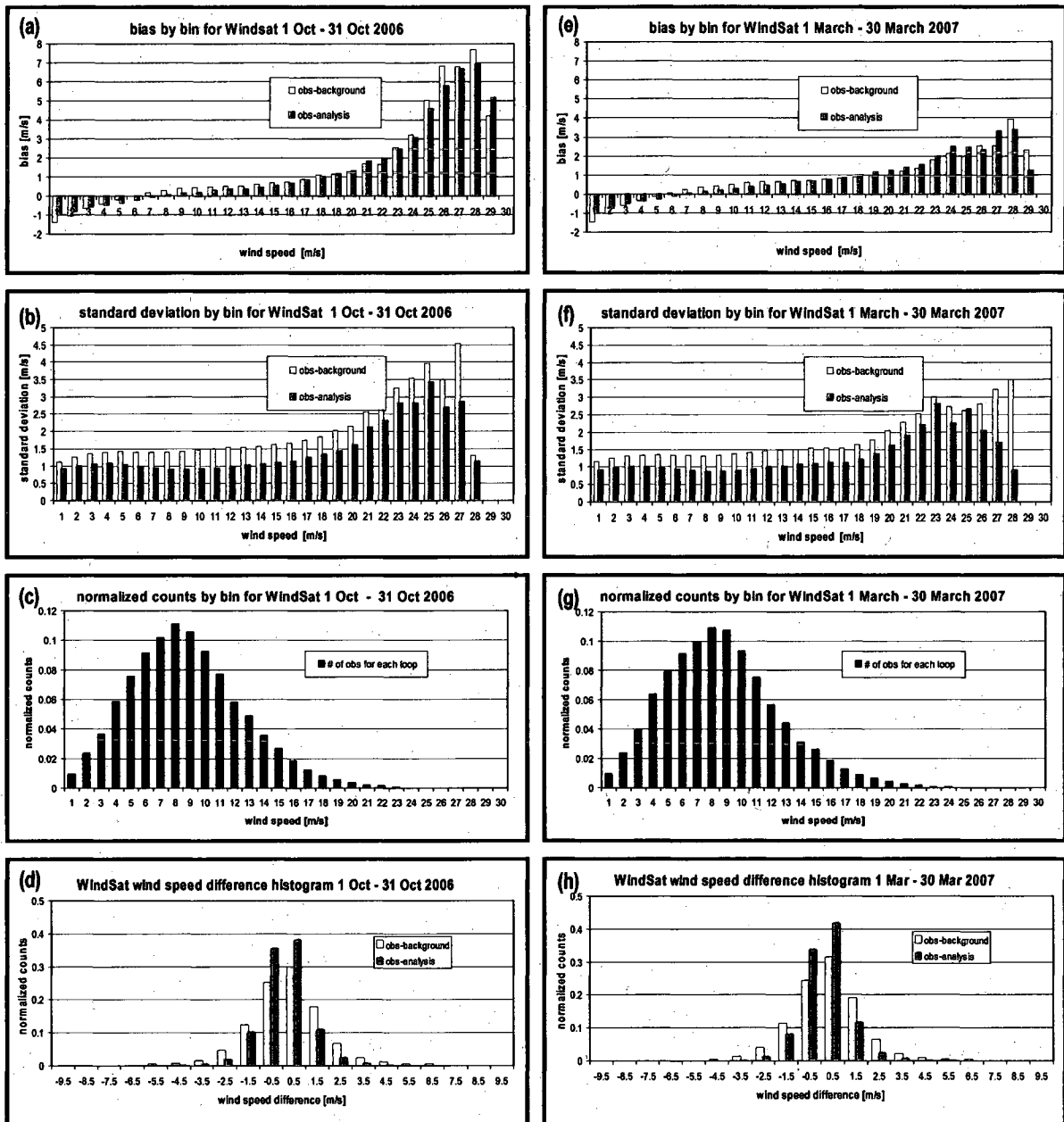
Figure 5.1. A comparison of the bias, standard deviation, normalized counts and WindSat wind speed difference histogram for WindSat data. Panels (a) – (d) show the results from October 2006 and panels (e) – (h) show the results from March 2007.
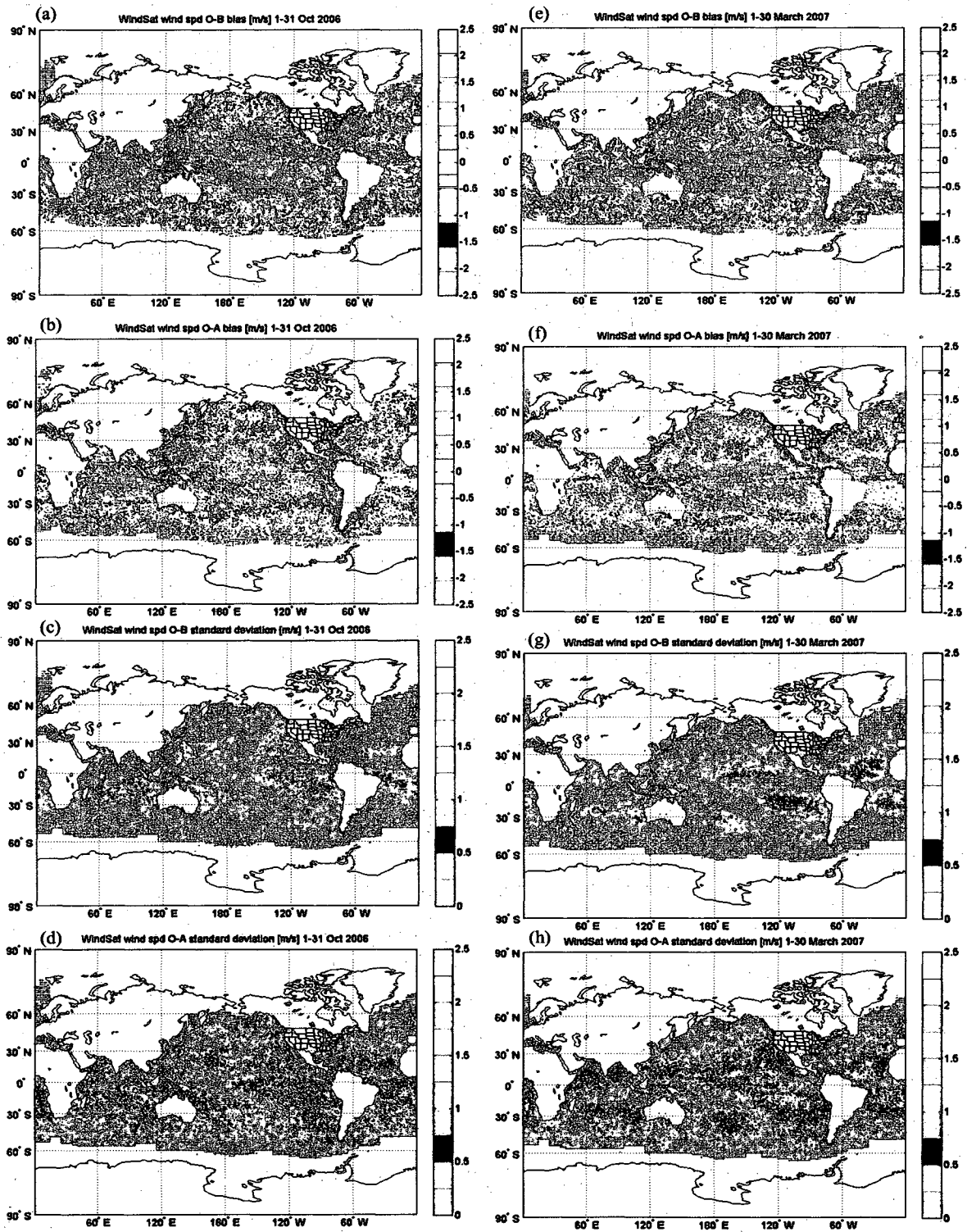
Figure 5.2. A comparison of the geographic distribution of bias, standard deviation (for both O-B and O-A) for WindSat. Panels (a) – (d) show the results from October 2006 and panels (e) – (h) show the results from March 2007.

(a) N. Hemisphere 500 hPa AC Z
20N - 80N   Waves 1-20
1 - 31 Oct 2006

(c) N. Hemisphere 500 hPa AC Z
20N - 80N   Waves 1-20
1- 30 Mar 2007

(b) S. Hemisphere 500 hPa AC Z
20S - 80S   Waves 1-20
1 - 31 Oct 2006

(d) S. Hemisphere 500 hPa AC Z
20S - 80S   Waves 1-20
1- 30 Mar 2007
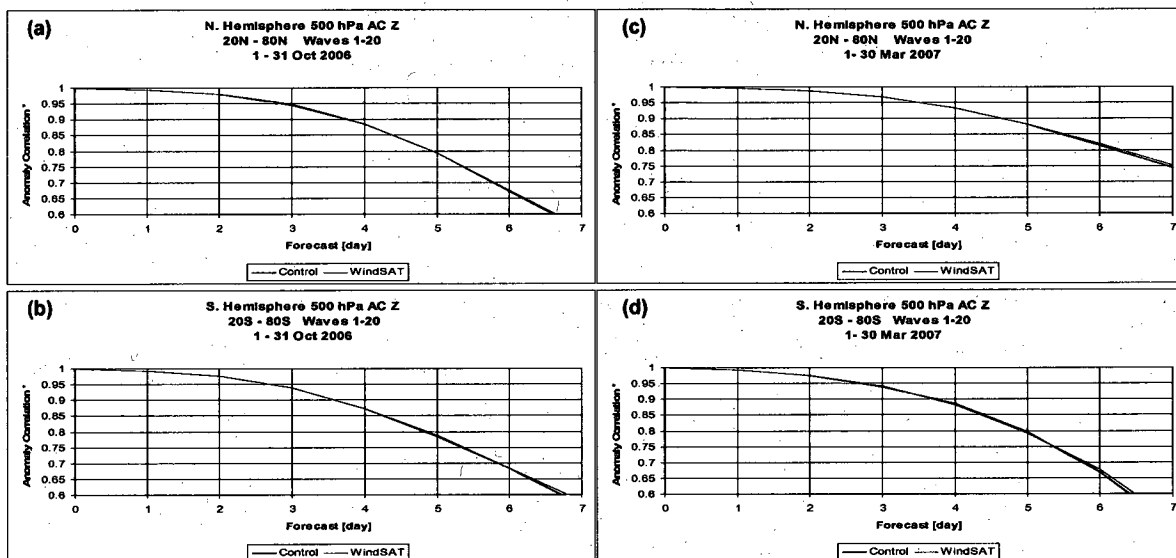
Figure 5.3. Anomaly correlation for days 0 to 7 for 500 hPa geopotential height and day 5 anomaly correlation bar charts of geopotential height in the regions 20°-80° in the Northern and Southern Hemisphere and for both seasons. Panels (a) and (b) show the result from October 2006. Panels (c) and (d) show the result from March 2007. For all panels the results have been truncated to only show results for waves 1 - 20.
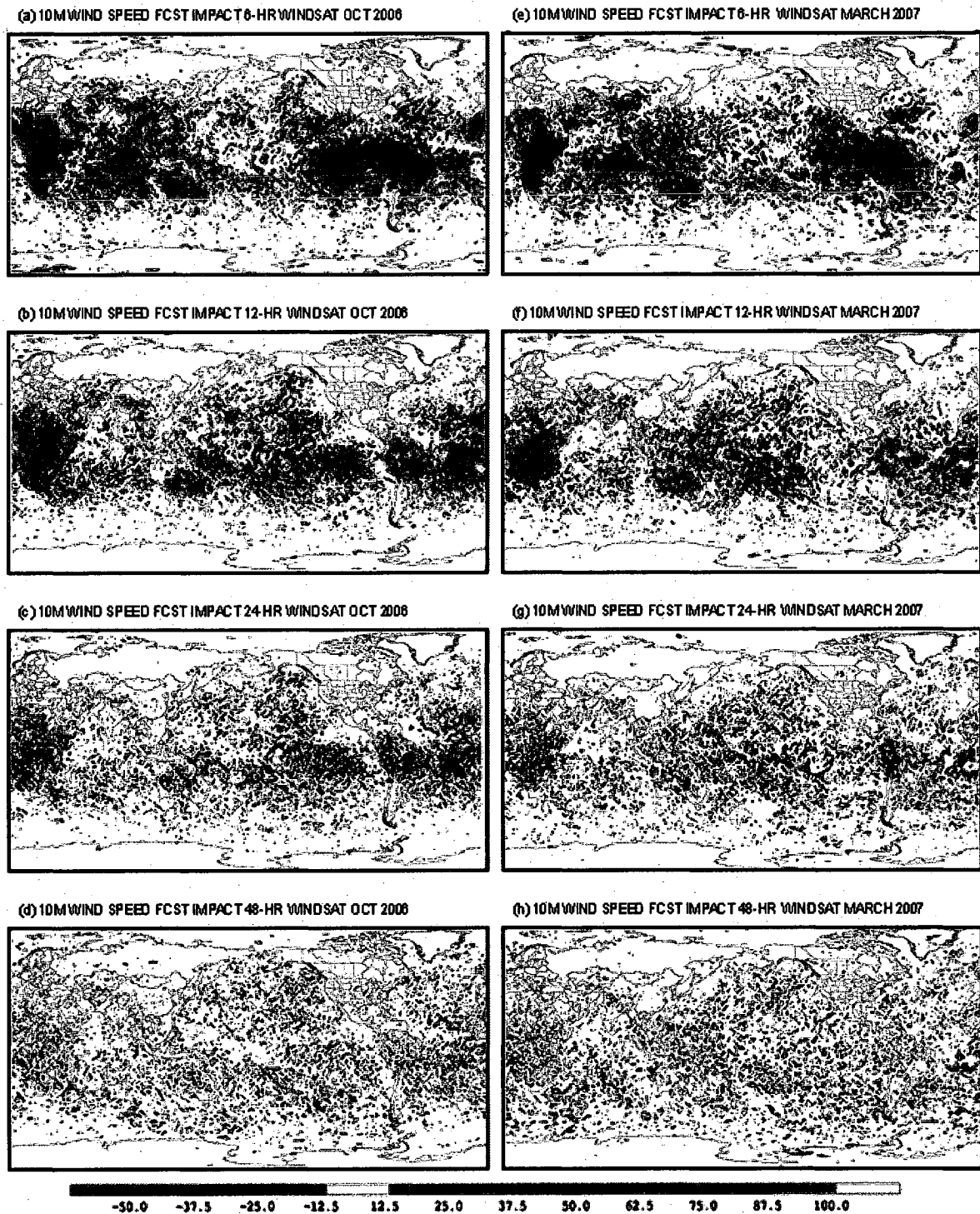
Figure 5.4. Geographic distribution of 10m wind speed Forecast Impact (%) at forecast hours (a) 6, (b) 12, (c) 24, and (d) 48 for October 2006 and forecast hours (e) 6, (f) 12, (g) 24, and (h) 48 for March 2007. The range of forecast impact is from -50 to +100.

(a) 500hPa WIND SPEED FCST IMPACT 6-HR WINDSAT OCT 2006
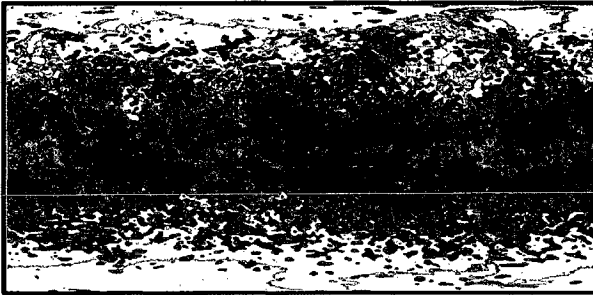
(e) 500hPa WIND SPEED FCST IMPACT 6-HR WINDSAT MARCH 2007
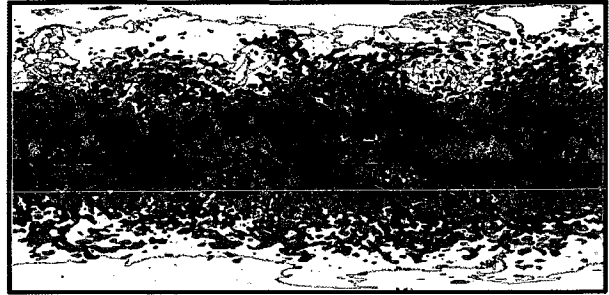
(b) 500hPa WIND SPEED FCST IMPACT 12-HR WINDSAT OCT 2006

(f) 500hPa WIND SPEED FCST IMPACT 12-HR WINDSAT MARCH 2007
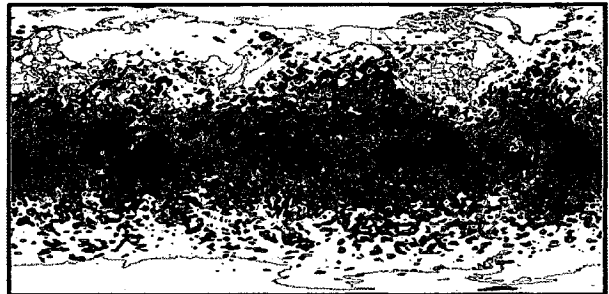
(c) 500hPa WIND SPEED FCST IMPACT 24-HR WINDSAT OCT 2006
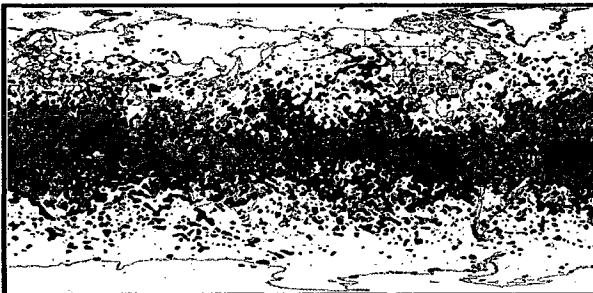
(g) 500hPa WIND SPEED FCST IMPACT 24-HR WINDSAT MARCH 2007

(d) 500hPa WIND SPEED FCST IMPACT 48-HR WINDSAT OCT 2006

(h) 500hPa WIND SPEED FCST IMPACT 48-HR WINDSAT MARCH 2007

-50.0   -37.5   -25.0   -12.5   12.5   25.0   37.5   50.0   62.5   75.0   87.5   100.0

Figure 5.5. Geographic distribution of 500 hPa wind speed Forecast Impact (%) at forecast hours (a) 6, (b) 12, (c) 24, and (d) 48 for October 2006 and at forecast hours (e) 6, (f) 12, (g) 24 and (h) 48 for March 2007. The range of forecast impact is from -50 to +100.

(a) 1000hPa TEMP FCST IMPACT 6-HR WINDSAT OCT 2006

(e) 1000hPa TEMP FCST IMPACT 6-HR WINDSAT MARCH 2007

(b) 1000hPa TEMP FCST IMPACT 12-HR WINDSAT OCT 2006

(f) 1000hPa TEMP FCST IMPACT 12-HR WINDSAT MARCH 2007

(c) 1000hPa TEMP FCST IMPACT 24-HR WINDSAT OCT 2006

(g) 1000hPa TEMP FCST IMPACT 24-HR WINDSAT MARCH 2007

(d) 1000hPa TEMP FCST IMPACT 48-HR WINDSAT OCT 2006

(h) 1000hPa TEMP FCST IMPACT 48-HR WINDSAT MARCH 2007

-50.0   -37.5   -25.0   -12.5   12.5   25.0   37.5   50.0   62.5   75.0   87.5   100.0
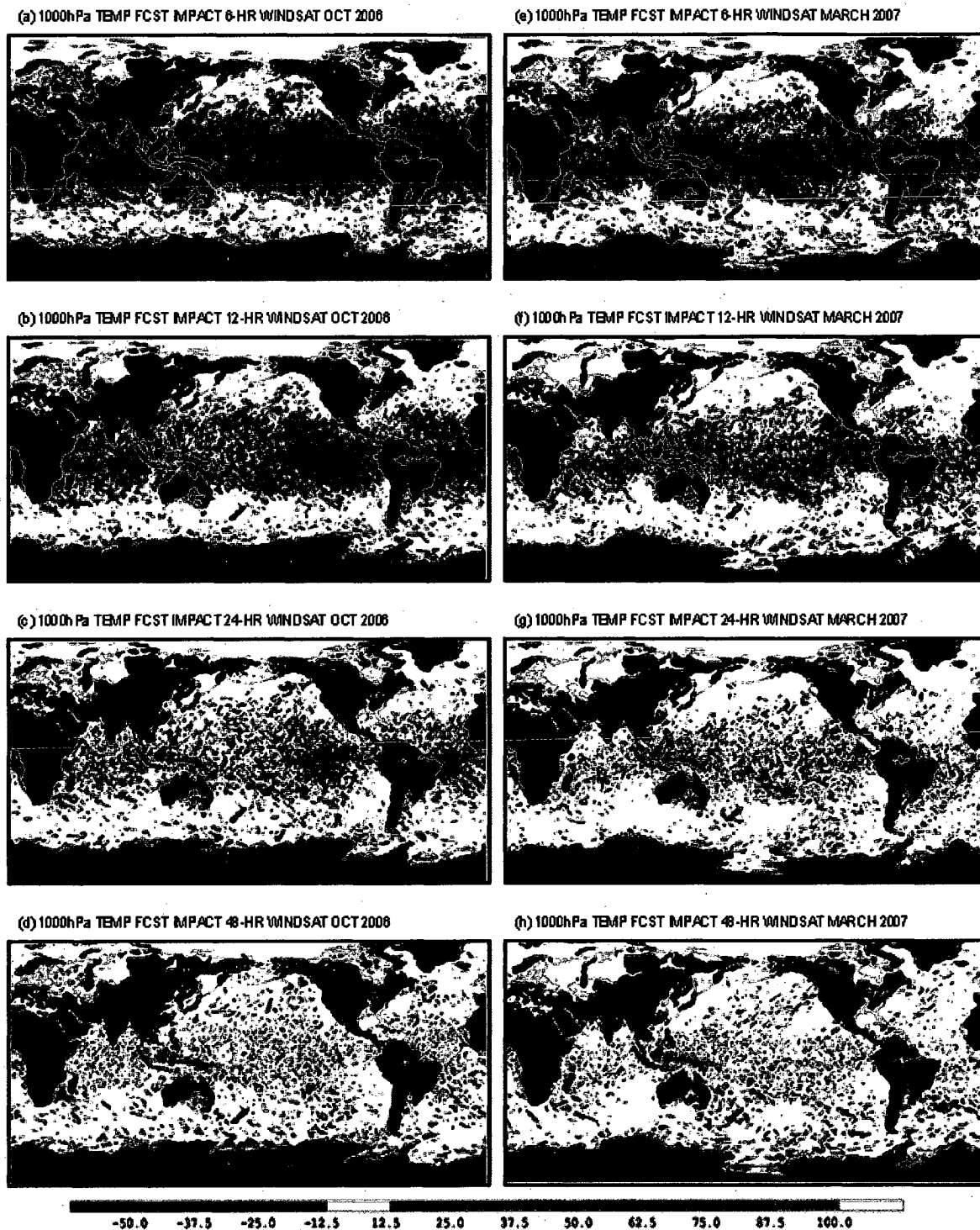
Figure 5.6. Geographic distribution of 1000 hPa temperature Forecast Impact (%) at forecast hours (a) 6, (b) 12, (c) 24, and (d) 48 for October 2006 and at forecast hours (e) 6, (f) 12, (g) 24, and (h) 48 for March 2007. The range of forecast impact is from -50 to +100. All points diagnosed as underground, were not used and are shaded black.

(a) 500hPa TEMP FCST IMPACT 6-HR WINDSAT OCT 2006

(e) 500hPa TEMP FCST IMPACT 6-HR WINDSAT MARCH 2007

(b) 500hPa TEMP FCST IMPACT 12-HR WINDSAT OCT 2006

(f) 500hPa TEMP FCST IMPACT 12-HR WINDSAT MARCH 2007

(c) 500hPa TEMP FCST IMPACT 24-HR WINDSAT OCT 2006

(g) 500hPa TEMP FCST IMPACT 24-HR WINDSAT MARCH 2007

(d) 500hPa TEMP FCST IMPACT 48-HR WINDSAT OCT 2006

(h) 500hPa TEMP FCST IMPACT 48-HR WINDSAT MARCH 2007

-50.0   -37.5   -25.0   -12.5   12.5   25.0   37.5   50.0   62.5   75.0   87.5   100.0

Figure 5.7. Geographic distribution of 500 hPa temperature Forecast Impact (%) at forecast hours (a) 6, (b) 12, (c) 24, and (d) 48 for October 2007 and at forecast hours (e) 6, (f) 12, (g) 24, and (h) 48 for March 2008. The range of forecast impact is from -50 to +100.
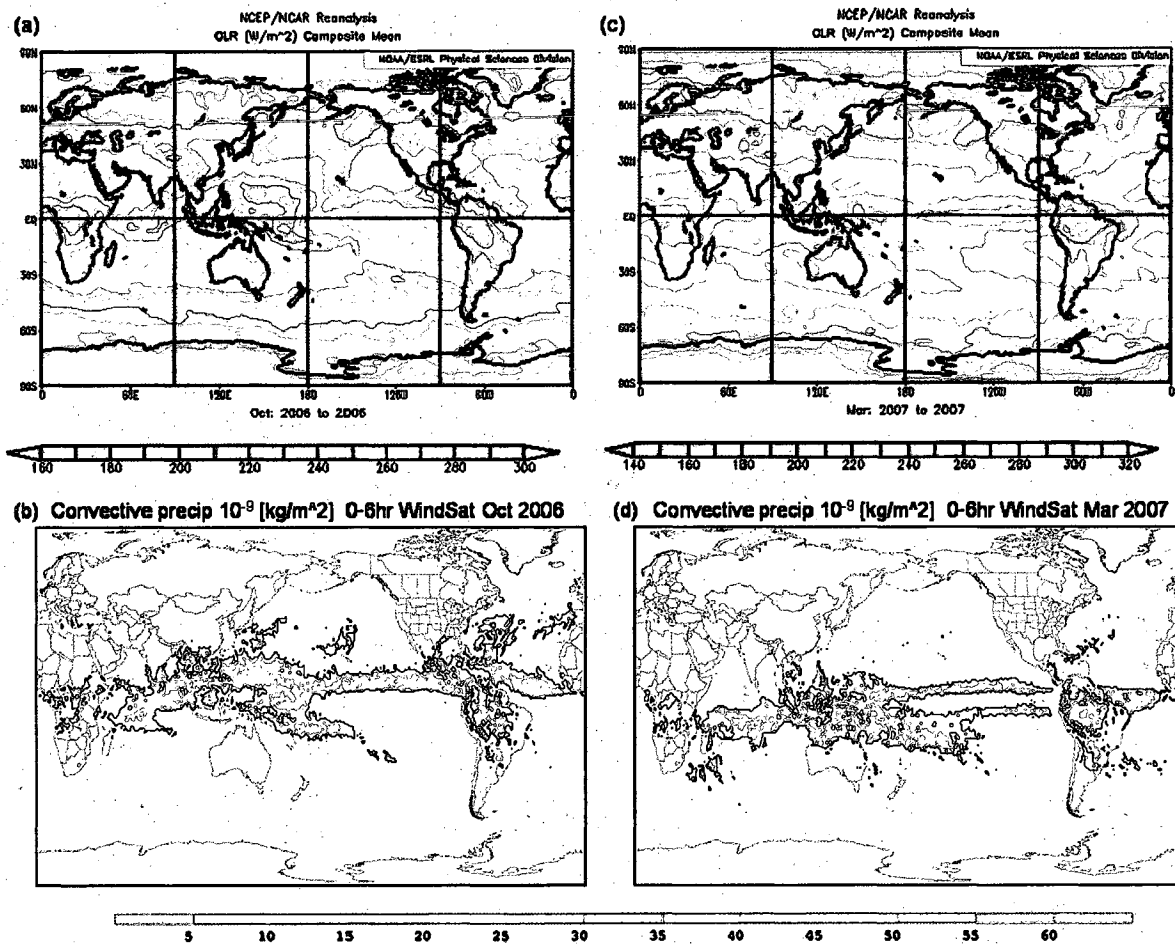
Figure 5.8. Geographic distribution of Outgoing Longwave Radiation (OLR) [w/m^2] mean using NCEP/NCAR reanalysis for the month of (a) October 2006, and of (c) March 2007. Geographic distribution of convective precipitation scale of 10^{-9} [kg/m^2] from 0-6hr forecast of WindSat assimilation for the month of (c) October 2006, and of (d) March 2007.
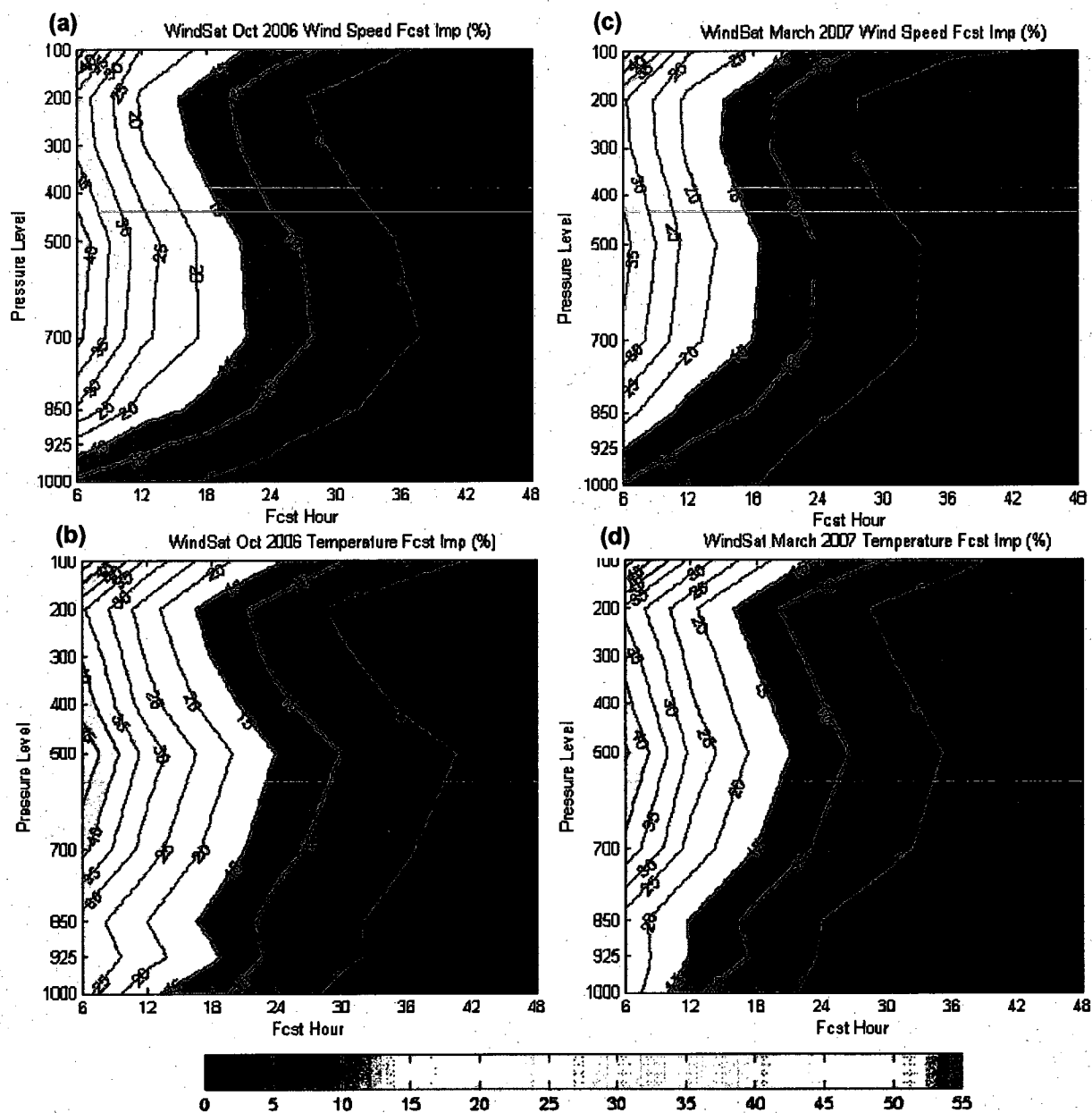
Figure 5.9. Vertical cross sections of Forecast Impact (%) on (a) wind speed and (b) temperature for October 2006 and Forecast Impact on (c) wind speed and (d) temperature for March 2007 as a function of pressure (hPa) and forecast time (hr) averaged over the globe. The colors have a uniform contour interval of 5%.

Chapter 6: ASCAT Surface Wind Retrievals Impacts Study in the NCEP Global Data Assimilation System

6.1 Introduction

Sea surface wind vectors have been estimated with active remote sensing instruments, such as QuikSCAT (Yu and McPherson 1984), and with passive polarimetric microwave radiometry, such as WindSat (Bettenhausen et al., 2006), and have been proven to have a positive impact on NCEP global forecasts (Le Marshall et al., 2006, Zapotocny et al., 2008, Bi et al., 2009). The latest remotely sensed surface wind-measuring instrument is the Advanced SCATterometer (ASCAT) (http://oiswww.eumetsat.org/WEBOPS/eps-pg/ASCAT/ASCAT-PG-index.htm). ASCAT is one of the instruments on the Meteorological Operational (MetOp) polar satellites launched by the European Space Agency (ESA) and operated by EUMETSAT. It is the first in a series of such instruments dedicated to provide routine surface wind observations over global oceans. ASCAT is an active microwave sensor designed to retrieve ocean surface vector winds. The mission of ASCAT is to enhance the spatial and temporal resolutions of surface winds at global and regional scales thereby allowing better characterization of the air-sea interaction process as well as ocean wind forcing.

ASCAT surface wind data are used in daily weather forecast operations at the European Centre for Medium-Range Weather Forecasts (ECMWF). Assimilation experiments of ASCAT surface wind vectors in the ECMWF analysis and forecast system

showed a positive effect on forecast skill over the Southern Hemisphere (http://www.ecmwf.int/publications/newsletters/pdf/113.pdf).

In this study, two seasons of ASCAT data have been assimilated into the National Centers for Environmental Prediction (NCEP) Global Data Assimilation/Global Forecast System (GDAS/GFS) model, the forecast impact of assimilating the ASCAT surface winds was assessed by comparing the forecast results with and without assimilating the ASCAT winds through 168 hours for the months of August 2007 and January 2008. Quality control procedures required to assimilate the surface winds are discussed. The geographical distribution of the anomaly correlations and forecast impacts are also presented.

The paper is structured as follows. Section 2 briefly describes background information related to the ASCAT instrument and the NCEP GDAS/GFS version used for this study. Section 3 discusses the diagnostic tools used to evaluate the forecast impacts. Section 4 presents the results for this forecast impact study through 7 days of model forecasts. Section 5 summarizes the overall results of these experiments.

6.2 Background

(a) ASCAT

ASCAT is a real aperture radar using vertically polarized antennas on the MetOP-A satellite which was launched on 19 October 2006. MetOp-A is the first in series of three satellites developed to provide meteorological data until 2020. MetOp is in a

circular orbit (near sun synchronous orbit) for a period of about 101 minutes, at an inclination of 98.59^0 and at a nominal height of 800km with a 29-day repeat cycle. The ascending equatorial times occur approximately at 09:30 p.m. local time for MetOp. ASCAT has two swaths 550 km wide, located on each side of the satellite track, separated by 700km. It operates at 5.3 GHz (C band) (Bentamy, 2008).

Two sets of three antennas are used to generate radar beams looking 45° forward, sideways, and 45° backwards with respect to the satellite's flight direction, on both sides of the satellite ground track. These beams illuminate 550 km-wide swaths (separated by about 700km) as the satellite moves along its orbit, and each provides measurements of radar backscatter from the sea surface on a 25 km or 12.5 km grid. The ASCAT beams measure normalized radar cross sections with vertical polarization, which are a dimensionless property of the surface, describing the ratio of the effective echoing area per unit area illuminated. The result of three independent backscatter measurements for each wind vector cell are obtained using the three different viewing directions separated by a short time delay. As backscatter depends on the sea surface roughness as a function of the wind speed and direction at the ocean surface, it is possible to calculate the surface wind speed and direction by using these 'triplets' within a mathematical model (http://www.knmi.nl/scatterometer/publications/pdf/ASCAT_Product_Manual.pdf).

The Koninklijk Nederlands Meteorologisch Instituut (KNMI) (Royal Netherlands Meteorological Institute) processes and makes available surface wind vector data derived from the ASCAT backscatter coefficient. For the KNMI ASCAT wind product, the CMOD5.5 geophysical model function (GMF) is used

http://www.knmi.nl/scatterometer/publications/pdf/ASCAT_Product_Manual.pdf). The GMF has two unknowns, namely wind speed and wind direction, so, if more than two backscatter measurements are available then these two unknowns may by estimated using a maximum-likelihood estimator (MLE) as the objective function for determining wind vector solutions (http://www.knmi.nl/scatterometer/publications/pdf/ASCAT_Product_Manual.pdf). The MLE is defined by the squared difference of the misfit between the transformed backscatter observations, $\sigma_0^{0.625}$, and the model backscatter values, $\sigma_m^{0.625}$:

$$J = (\sigma_0^{0.625} - \sigma_m^{0.625})^2.$$

The local minimum of J corresponds to the wind vector solution. The three independent measurements (fore, mid, and aft beam), sample the azimuth variation of the GMF so that at the wind direction may be determined with ambiguity (two solutions). These ambiguities are removed by applying constraints on the spatial characteristics of the output wind field, such as on rotation and divergence. The solution selection is performed based on the 2D-VAR method (Stoffelen et al., 2002).

The ASCAT data flow from the MetOp satellite to the National Oceanic and Atmospheric Administration's (NOAA) processing system and are converted into the Binary Universal Form for the Representation of meteorological data (BUFR) format at the NOAA NCEP in preparation for operational use.

(b) Global Data Assimilation System

The NCEP assimilation system consists of a first or "early" cycle with a 2.5 hour

cut-off. The analysis for this cycle is centered on 0000, 0600, 1200, and 1800 UTC and is followed by a 384 hour forecast. Consistent with the operational GDAS/GFS, a model resolution of T382L64 (i.e., spectral triangular truncation 382 with 64 layers) is used through 168 hours. For this study, only the 0000 UTC forecasts were run and only out to 168 hours. The analysis is repeated later (+6 hrs) to provide the "final" analysis for the six hour forecast for the next early cycle first guess. This "final" analysis includes data that had missed the previous "early" cut-off.

The vertical domain of GFS model ranges from the surface to approximately 0.27 hPa and is divided into 64 unequally spaced sigma levels with enhanced resolution near the bottom and top of the model domain. There are 15 layers below 800 hPa and 24 layers above 100 hPa. The time integration is leapfrog for nonlinear advection terms and semi-implicit for gravity waves and the zonal advection of vorticity and moisture. Comprehensive documentation of the GFS was completed by the National Meteorological Center's (now NCEP's) Development Division (1988) and can be found online at http://wwt.emc.ncep.noaa.gov/gmb/wd23ja/doc/web2/tocold1.html. Subsequent model developments after completion of the above documentation have been summarized by Kanamitsu (1989), Kalnay (1990), and Kanamitsu et al. (1991). More recent updates to the radiation, surface layer, vertical diffusion, gravity wave drag, convective precipitation, shallow convection, and non-convective precipitation can be found at http://sgi62.wwb.noaa.gov:8080/research/SONGYU/doc/physmrf1.html. The most recent information about the global atmospheric forecast model (2003) is in NCEP Office Note No. 442 or online at

http://emc.ncep.noaa.gov/officenotes/newernotes/OF442.pdf.   A summary of model

changes and references up to and past the dates of this study are available in an "updates"

log of changes online at both http://www.emc.ncep.noaa.gov/gmb/moorthi/gam.html and

http://www.emc.ncep.noaa.gov/gmb/STATS/html/model_changes.html.

The GDAS/GFS analysis utilizes a three-dimensional variational data assimilation

(3DVAR) scheme to obtain an initial state that optimally fits the available observations

and a short-range forecast (background). In this study, we used NCEP's Gridpoint

Statistical Interpolation (GSI) (Derber et al. 1991; Wu et al. 2002; Derber et al. 2003)

3DVAR system. With this type of analysis system, the incorporation of radiances directly

into the analysis and assimilation system has become practical. The analysis is a 3D

retrieval of mass, momentum, and moisture fields derived from all available data

including the radiances (Caplan et al. 1997). The GSI uses a thinning routine which

identifies the optimal radiance profile for each satellite sensor type (AMSU, HIRS, MSU,

etc.) in a pre-designated grid box. The optimal radiance profile is determined by its

departure from the model background temperature, distance from the center of the grid

box, temporal departure from the assimilation time, and surface features (ocean, land, and

ice). The December 2007 version of the GDAS/GFS was used for these observing system

experiments.

6.3 Experimental design

The complete NCEP operational database of conventional and satellite data was

used for this experiment. This reflected the real-time data cut-off constraints for the early

and late assimilation cycles produced at NCEP. The conventional data used included rawinsonde temperature, relative humidity and wind, aircraft observations of wind and temperature; land and oceanic reports of surface pressure, temperature, horizontal wind, and specific humidity. The satellite observations used in this work include the operational Advanced Television Infrared Observation Satellite (TIROS-N) (NOAA 2000), Operational Vertical Sounder (TOVS) (Smith et al. 1979) radiances from the High Resolution Infrared Radiation Sounder (HIRS), the Microwave Sounding Unit (MSU) (Spencer and Christy 1990), the Advanced Microwave Sounding Unit (AMSU-A and AMSU-B) sensors (NOAA 2005), ozone information from the Solar Backscatter Ultraviolet (SBUV) sensors (Miller et al. 1997); Defense Meteorological Satellite Program (DMSP) Special Sensor Microwave Imager (SSM/I) surface wind speed (Alishouse et al. 1990); derived surface winds from Quikscat (Yu and McPherson 1984); derived surface winds from WindSat (Bettenhausen et al. 2006); atmospheric motion vectors from geostationary satellites (Velden et al. 1997; Menzel et al. 1998). Keyser (2001a, 2001b, 2003) provides an overview of data types provided to NCEP on a daily basis and used operationally for the experiments of this study. The conventional and satellite data used in these experiments are summarized in Tables 2 and 3, respectively.

Parts of two seasons were used for this study; summer 2007 (15 July to 30 August 2007) and winter 2007/2008 (15 December 2007 to 30 January 2008). The first two weeks of each time period were removed from these results to allow the assimilation system and forecast model to adjust to the new data.

(a) Data thinning

Instead of using the thinning technique that is used operationally for QuikSCAT wind and WindSat vectors, namely the use of "super observations" (or "super-obs"), a new thinning technique was used for ASCAT winds. The main idea of this thinning technique is that wind vectors which are closest to the center of the thinning box (100km) are chosen over all others. In comparison, a super-ob is the average of all the observations in each thinning $1° \times 1°$ box with the resulting observation located in the centroid of the observations. Observations which have a low confidence (determined by KNMI) due to rain, ice, or land contamination are not used in the super-ob. Tests were run to determine whether 100km or 50km thinning boxes were more effective. It was found that overall the 100km thinning box gave the best forecast results in terms of the anomaly correlation scores.

(b) Quality Control

Most of the quality control (QC) of the ASCAT data was accomplished in the retrieval process. Observations that fail the retrieval process or are flagged for rain, land, or sea ice contamination were flagged and omitted from the observations as outlined in (http://www.knmi.nl/scatterometer/publications/pdf/ASCAT_Product_Manual.pdf).

The preliminary statistical results from the 20-day test experiment indicated that there were problems near the Antarctica regions which were contaminated by sea-ice. This contamination suggested there were still quality control problems with the observations even after the quality control procedures were performed during the retrieval

process. It is essential to investigate additional quality control procedures before the ASCAT data are assimilated to the GFS system. Bases on the preliminary statistical results, a series of additional quality control procedures were added within GDAS/GFS. To remove additional data suspect of being contaminated by sea ice, a Sea Surface Temperature (SST) of 273K was used as a criteria . Observations near coastlines were also not used. If the absolute value of the thinned wind component differs from the corresponding background wind by more than $5ms^{-1}$ or the observed or model background wind speeds were greater than $20ms^{-1}$, the wind vector was removed.

(c) Diagnostics

Several diagnostics were performed using the control and ASCAT experiment analyses and forecasts. The anomaly correlation statistics were performed using the traditional NCEP algorithms (NWS 2006) which are similar to those used by NWP centers worldwide. NCEP (NWS 2006) provides a description of the method of computation while Lahoz (1999) provides an interpretation for the anomaly. The reanalysis fields from the National Center for Atmospheric Research (NCEP/NCAR) (Kistler 2001) are used for the climate component of the anomaly correlations. To calculate anomaly correlations the output grids from the control and both experiments were reduced to this 2.5° by 2.5° horizontal resolution and interpolated to mandatory rawinsonde levels using the GFS post processor. The fields being evaluated using anomaly correlations are then truncated to only include spectral wave numbers 1 through 20. These fields are also limited to the zonal bands of 20°-80° in each Hemisphere and a

tropical belt within 20° of the equator.

In addition to the traditional AC statistics, geographic distributions of the AC for the 1000hPa and 500hPa geopotential height fields are performed. The fields being evaluated using geographic AC distributions include all spectral wave numbers. These fields are not limited to the zonal bands or the tropical belt.

Another diagnostic used here is the modified forecast impact (FI), which is discussed further by Zapotocny et al. (2005). For this study, a series of two-dimensional FI results are presented as the positive/negative impact provided by the experiment of a particular data type. The geographic distributions of FI are shown in section 4.b and are evaluated using:

$$FI(x,y) = 100 \times \left\{ \left[\sqrt{\frac{\sum_{i=1}^{N}(C_i - A_i)^2}{N}} - \sqrt{\frac{\sum_{i=1}^{N}(E_i - A_i)^2}{N}} \right] / \sqrt{\frac{\sum_{i=1}^{N}(E_i - A_i)^2}{N}} \right\} \quad (1)$$

The variables C and E are the control and experiment forecasts, respectively. The variable A is the 00-hr GDAS experiment analysis containing all data types which is valid at the same time as the forecasts. N is the number of diagnostic days.

The area ratio weights the grid points to account for the reduction in area as the grid boxes approach the poles. The area ratio weighting is defined as:

$$A_i' = A_i \times \frac{\sin(\phi_i + \frac{\Delta}{2}) - \sin(\phi_i - \frac{\Delta}{2})}{2\sin(\frac{\Delta}{2})} \quad (2)$$

Where ϕ is the latitude of grid point i and Δ is north/south resolution of the grid box. The numerator is the relative size of the grid box. The denominator is the relative size of a

grid box at the equator.

The vertical cross section plots shown in section 4.c are evaluated using:

$$FI(t,z) = 100 \times \left[\frac{\sqrt{\dfrac{\sum\limits_{i=1}^{X}(C_i' - A_i')^2}{X}} - \sqrt{\dfrac{\sum\limits_{i=1}^{X}(E_i' - A_i')^2}{X}}}{\sqrt{\dfrac{\sum\limits_{i=1}^{X}(E_i' - A_i')^2}{X}}} \right] \qquad (3)$$

Where X is the number of horizontal grid points. A', C' and E' are the area ratio weighted values of A, C and E defined in (1). The first term on the right enclosed by parentheses in (1) and (3) can be considered the error in the denied experiment. The second term enclosed by parentheses in (1) and (3) can be considered the error in the control forecast. Dividing by the error of the control forecast normalizes the results. Multiplying by 100 provides a percent improvement/degradation with respect to the RMS error of the control forecast. A positive forecast impact means the WindSat forecast compares more favorably to its corresponding analysis than the control.

The FI is then averaged over the number of days by using:

$$F_t = \frac{\sum\limits_{i=1}^{N} FI(t,z)}{N} \qquad (4)$$

Where FI is from (3) and N is the number of diagnostic days.

All FI diagnostics were computed from grids generated by NCEP's post processing package. These grids have a 1° x 1° horizontal resolution on 26 vertical isobaric surfaces. None of the fields were smoothed during plotting. The forecast

diagnostics for this paper were also terminated at 48 hours to concentrate on the shorter term forecast impacts.

6.4 Results

Assimilation experiments were conducted to test and compare the attributes of using the ASCAT data. Forecast impact comparisons are presented from assimilating the ASCAT data to a benchmark or control experiment. The control contains all the operational data used during the period and includes all of the real-time data cutoff requirements. The impact of assimilating the ASCAT data on the quality of forecasts made by the GFS for two time periods are explored in detail. The first time period covers 1 to 31 August 2007, the second covers 1 to 30 January 2008. The selection of these time periods enables the diagnostics to sample the extreme seasons in each hemisphere. The fields diagnosed consist of geopotential height, temperature, and wind speed. Underground grid points on isobaric surfaces intersecting the earth's surface are not included in the evaluations.

(a) Analysis statistics

Figure 6.1 displays a comparison of the bias, standard deviation, ASCAT wind speed histogram and wind speed innovation histogram for ASCAT. Figures 6.1 (a) – (d) show the analysis statistics for August and (e) – (h) show the analysis statistics for January. While there are relatively large biases for observed wind smaller than $2ms^{-1}$ for both seasons, these observations account for less than 5% of the total number of

observations (Figs. 6.1d and 6.1g), thus large biases are not a major concern. Before the ASCAT experiment began, a 20-day test run was performed. Based on the preliminary statistical results of this test, observed wind speeds that are greater than 20ms^{-1} have been tossed. Figure 6.1a and 6.1e show that there are also large biases and standard deviations for observed wind speeds greater than 20ms^{-1} and in some cases biases and standard deviation for observation minus analysis (O-A) are even higher for observation minus background (O-B), these observations are rejected by the assimilation system. In the GSI assimilation system, there are three outer iteration loops; observations which passed the first outer loop may still be rejected in the second outer loop. The final analyses are results from the third outer loop. Figures 6.1c and 6.1g show that the majority of the counts are located within the wind speed range of 5-10 ms^{-1}. In Figure 6.1d and 6.1h, the green curve shows the observation minus background (O-B) and red curves represents the observation minus analysis (O-A). The O-B histograms are slightly skewed to the left for both seasons which suggests ASCAT speeds are a little slower than the model background.

Figure 6.2 displays the geographic distribution of bias and standard deviation for wind speed at 10 meter near the surface for both O-B and O-A for August (a-d) and January (e-h). In the August experiment, the largest biases with respect to the background are found in the tropical Western Pacific, and in bands extend westward from the Mexican coast to the central Pacific and to the east-southeast south of central America (Fig. 6.2a). In the January experiment, the largest biases were found over the central Pacific and Indian Ocean (Fig. 6.2e). As expected the biases are significantly reduced in

most regions after assimilating the data (Fig. 6.2b and 6.2f) but larger biases appear in the Southern Hemisphere near Antarctica. The standard deviations of O-B are quite similar to the January experiment for August (Fig. 6.2c), with the largest standard deviations are found in the tropical western Pacific and near Antarctica. For the January experiment, the largest standard deviations are found over the northern Pacific, in the topical western Pacific, and north Atlantic. Again, after ASCAT data have been assimilated, decreases in the standard deviation are realized.

(b) Geographic distribution of Anomaly Correlations (AC)

Figures 6.3a and 6.3e present the global geographic distribution of 1000 hPa geopotential height anomaly correlations for the control simulations during August 2007 and January 2008 respectively.   Figure 6.3b and 6.3f show the global geographic distribution of 1000 hPa geopotential height anomaly correlations for the ASCAT experiment simulations during August 2007 and January 2008 respectively. The geographic distribution of the difference between the control and ASCAT experiment anomaly correlation are presented in Figure 6.3c and Figure 6.3g during August 2007 and January 2008 respectively. For the anomaly correlation difference distribution, the largest negative difference are realized over the Arctic and Antarctic , the largest positive difference are located over Russia (Fig. 6.3c) for August. The patterns are quite different for January, with the largest positive difference realized over the western Indian Ocean and the large negative differences along the coasts of the Antarctic continent (Fig. 6.3g). Figures 6.3d   and h show the anomaly correlation for days 0 to 7 for 1000hPa

geopotential height in the regions 20^0 - 80^0 in the Southern Hemisphere for August and Northern Hemisphere for January respectively. The green line is the control simulation which closely replicates NCEP operations and includes all data routinely used by the GDAS/GFS. The red line is the anomaly correlation diagnosed from the ASCAT simulation. In these types of experiments, the larger the separation between anomaly correlations for the experiment and the control, the greater the skill of the forecasts using ASCAT data compared with the control forecasts. The results indicate that the control simulation anomaly correlations are close to the ASCAT experiment anomaly correlations until day 5, then the improvements in the ASCAT experiment become greater for both seasons and in most of the cases.

As it is commonly presented, the AC is just a single number representing the skillfulness of a forecast relative to climatology. By definition, AC scores are calculated as the correlation between the predicted and analyzed anomalies of the variables over region and over time. AC scores cannot reveal anything about how the skill is manifest (small improvements, on average each day, *vs.* a few large improvements related to a particular event), the geographic distribution of forecast skill, or whether the diagnosed skill is realized in regions of low or high observed anomalies as calculated from the NCEP/NCAR reanalysis data. In order to understand how the improvements are realized on a day to day basis, in a preliminary study, instead of calculating the time mean of the AC, the fraction of daily AC score over the time mean has been calculated. This day by day improvement *vs.* degraded forecast assessment provided insight into whether the factors governing the average AC score are dominated by greatly improved specific

forecast busts or small improvement on average each day. Although not shown in here, our study indicates that the governing factor of AC score is dominated by small improvement on average each day.

In order to have a better understanding about the geographic distribution of AC and the corresponding observed anomalies as calculated from the reanalysis data, we inspect the geographic distribution of AC along with the distribution of observed anomalies. We identify four possible scenarios or categories:

- Category I: Large AC coincides with small monthly mean anomalies. Results in this category show good medium range forecast skill in capturing small amplitude and/or low frequency anomalies as calculated from the climatology data.

- Category II: Large AC coincides with large anomalies. This is also a good example shows the forecast is capable of forecasting significant height anomalies at the medium range.

- Category III: Small AC coincides with small anomalies. Cases shown in this category indicate low forecast skill for small amplitude anomalies or lack of medium range skill in transitions between weather regimes.

- Category IV: Small AC coincides with large anomalies. This is the scenario which indicates regions with large anomalies report as small AC coeffieicient. Based on the assumption that the monthly mean anomalies is representative of daily anomalies, it suggests that cases falling in this category lack medium range forecast skill in predicting low frequency patterns.

Figures 6.4a and c show the geographic distribution of 500hPa geopotential height

anomaly using NCEP/NCAR reanalysis for the month of (a) August 2007, and of (c) January 2008. Panels (b) and (d) show the geographic distribution of anomaly correlation of day 5 for 500hPa geopotential height from the ASCAT experiment from (b) August 2007 and from (d) January 2008. Regions can be identified where large monthly mean anomalies do not coincide with the regions of greatest forecast anomaly correlation. Figure 6.4a can be compared with Fig. 6.4b, same applies for Fig 6.4c and Fig. 6.4d. In Fig. 6.4a, the largest height anomalies for August 2007 are noted in Arctic Ocean and in a band in the south Pacific off South America. In the two-dimensional AC plot (Fig. 6.4b), it is seen that in the south Pacific regions, the AC scores are quite large with values close to 0.9. On the other hand, the large observed anomalies located in the Arctic north of Alaska are in regions of low forecast skill as measured by the AC scores. (with small AC value around 0.4). For the month of January 2008, the largest anomalies were observed in north Pacific, western Russian, and in the Arctic north of Siberia. The height anomalies over the Arctic and north Pacific coincided with high AC scores, while the eastern most portion of the positive height anomaly in western Russia was in a region of low forecast skill.

(c) Geographic distributions of forecast impacts

All the forecast impacts shown in this paper have been tested as significant differences between the control and experiment. The differences in the temperature and wind fields shown here are statistically significant with a confidence interval of 99% or greater for forecasts out to 36 hours. Figure 6.5 displays geographic distributions of

Reproduced with permission of the copyright owner. Further reproduction prohibited without permission.

average forecast impact, determined from using equation (1), for the 10m wind speed for August 2007 at forecast hours (a) 6, (b) 12, (c) 24, and (d) 48 and for January 2008 at forecast hours (e) 6, (f) 12, (g) 24, and (h) 48. The range of FI is from -60 to 200 percent. The 6-h results (Fig. 6.5a) show the largest FIs in Africa, Western Pacific, South America and China. By 12 hours (Fig. 6.5b), the FIs in the South America are reduced, with the largest FI still realized over Africa and China. The FIs are generally small by 24 hours (Fig. 6.5c) and become mostly neutral by 48 hours (Fig. 6.5d). Figure 4e-h presents the January 2008 ASCAT 10m wind speed FIs at forecast hours 6, 12, 24, and 48 respectively. Large positive FIs are seen over Africa, Australia, and South America at 6 hours (Fig. 6.5e). By 12 hours (Fig. 6.5f), the largest FIs are still found over Africa. Again, the FIs are generally small by 24 hours (Fig. 6.5g) and become mostly neutral by 48 hours (Fig. 6.5h).

The FIs for 500 hPa wind speed during August 2007 and January 2008 are shown in Figure 6.6a-d and e-h respectively. The greatest FIs are realized in the tropics for both seasons as shown by the 6 and 12 hour forecasts. By 24 hours (Fig. 6.6c and Fig. 6.6g), the FIs are reduced with small positive impacts still seen in the tropical region. By 48 hours (Fig. 6.6d and Fig. 6.6h) the FIs are mostly neutral with some small positive impacts remaining. Comparing Fig. 6.5 and 6.6 suggests that the ASCAT data have a greater positive impact on the wind speed field through the 24-h forecast at 500hPa than at 10m.

Figure 6.7 presents the temperature geographic distribution of FI at 1000hPa for the two seasons at forecast times 6, 12, 24 and 48 hours. All points diagnosed as

underground, were not used and are shaded black. The 6-h results (Fig. 6.7a and e) show the largest positive FIs in the tropics. Small areas of negative FI are noted near Antarctica during both seasons. After 12 hours, large areas of positive FIs are still realized over the Western Pacific and South Atlantic (Fig. 6.7b and f). Similar to the wind FIs at 48 hours (Fig. 6.7d and h), the FIs are mostly neutral with small areas of positive and negative impact remaining. With the exception of the region around Antarctica, the FI is largely positive or neutral over a significant portion of the globe.

The FIs for temperature at 500hPa during both periods are shown in Figure 6.8. Similar to the 1000hPa temperature FIs, the largest impacts are found in tropics in the 6-h forecasts for both seasons (Fig. 6.8a and Fig. 6.8e). There is a marked decrease in forecast impact by 12 hour (Fig. 6.8b and Fig. 6.8F) with all of the largest impacts still realized in the tropics. The FIs are generally small by 24 hours (Figs. 6.8c and g) and becomes mostly neutral by 48 hours (Figs. 6.8d and h). Comparing Figs. 6.7 and 6.8 indicates that the ASCAT data have a markedly more positive impact in magnitude on the temperature field through the 24-h period at 500hPa than at 1000hPa.

One potential explanation for why the large impacts are seen in the tropics at 500hPa for both wind speed and temperature fields is due to the deep convection associated with the convective scheme used in the GFS model which is in based on Arakawa and Schubert (1974) scheme, in which mass fluxes induced in the convective updraft and the downdraft are allowed to transport momentum. The momentum exchange is calculated through the mass flux formulation in a manner similar to that for heat and moisture. Fig. 6.9 shows the geographic distribution of Outgoing Longwave Radiation

(OLR) [w/m^2] mean using NCEP/NCAR reanalysis for the month of (a) August 2007, and of (c) January 2008. Fig. 6.9a indicates that there is deep convection located in Indian, and eastern Pacific along the tropics. Fig. 6.9c shows deep convection located in the north-east of Australia in the pacific, Indian and South America. The deep convection along the tropics is consistent with the largest FI which is along the tropics for 500hPa wind speed field (Fig. 6.6a and Fig. 6.6e). Because of the deep convection transport the momentum upward, the surface wind analysis increment information propagates upward into the middle and upper-troposphere within the first 6 hours. Another approach is to look at the convective precipitation plots, geographic distribution of convective precipitation scale of 10^{-8} [kg/m^2] from 0-6hr forecast of ASCAT assimilation for the month of (c) August 2007, and of (d) January 2008. It is clear that the convective precipitation band is realized along tropics for both seasons, that also explains why the largest FIs are seen along the tropics as early as 6 hour in the middle and upper-troposphere. The 6-12hr, 18-24hr, 42-48hr convective precipitation plots have similar pattern as the 0-6hr ones, they are not shown here.

Figure 6.10 presents the vertical time series of the horizontally averaged Forecast Impacts from both seasons. This figure was computed using equation (2) and area weighted using equation (3). Forecast impacts from the wind speed (Fig 6.10a and 6.10c), and temperature (Fig 6.10b and d) fields are shown for both seasons. Inspection of the plots reveals that the largest impacts are at the 500hPa level and is consistent with the geographic Forecast Impacts in Fig. 6.6. Large impacts are also shows at 100hPa. Similar patterns are found in the temperature fields in Fig. 6.10b where the greatest

Forecast Impacts are again at 500 and 100hPa. All four panels display a systematic decrease of FI with time, with the decreases being somewhat slower in January than in August. A final point about the vertical time series of Forecast Impact results is that the 6-h temporal resolution of the GFS archive used for these experiments is not adequate to resolve the rapid decrease in forecast impact that occurs in the first 12 h of these simulations.

Figure 6.11 presents the vertical time series of the horizontally averaged forecast impacts for both seasons. Wind speed forecast impacts from the fields averaged for Northern Hemisphere (NH) (Fig. 6.11a and Fig. 6.11d), for Southern Hemisphere (SH) (Fig. 6.11b and Fig. 6.11e), and for tropics (Fig. 6.11c and Fig. 6.11f) are shown for both seasons. Inspection of summer hemisphere plots (Fig. 6.11a and Fig. 6.11e) reveals similarities with maximum impacts are found at 500hPa with amplitude of 25%. Inspection of winter hemisphere plots (Fig. 6.11b and Fig. 6.11d) also reveals similarities with maximum impacts are found at 500hPa with amplitude of 15%. An explanation for the maximum FI realized at 500hPa is due to the upward momentum transport in the parameterized convection of the GFS model. In general, the summer hemisphere has far more convective activity than the winter hemisphere, this explains why the amplitude of FIs are greater in the summer hemisphere. Comparing the winter hemisphere plots (Fig. 6.11b and Fig. 6.11d), it is also noted that for NH the FIs are not seen in the surface after 12 hrs (Fig. 6.11d); for SH the FIs are still seen in the surface till 18 hrs (Fig. 6.11b). This is because SH is data sparse region, more new data assimilated in the ocean will lead to greater impacts. It is also noted that the greatest impacts are occurred in the tropics with

the maximum magnitude over 100% (Fig. 6.11c and f). This is consistent with the largest impacts we have seen along the tropics. In general, the maxima in fractional area coverage of the convective activity are typically centered off the equator. Because of the deep convection transport the momentum upward, the surface wind analysis increment information propagates upward into the middle and upper-troposphere with the first 6 hour. The surface are within the boundary layer, with all the mixing and friction, the impacts get lost very soon. This may explain why the greatest impacts are not seen near the surface. All panels reveals that the FIs decrease with time very fast, by 24 hours, most of the impacts are not seen.

6.5 Summary

Observing system experiments were conducted during two seasons to quantify the impacts of assimilating the surface wind retrievals from the ASCAT microwave scatterometer on the Met-Op satellite. A December 2007 version of the NCEP GDAS/GFS was used for the assimilation system and forecast model. These experiments were conducted at the NCEP operational resolution of the time (T382 with 64 layers) and used the NCEP operational observation database.

Several verification techniques were used to measure the impact the ASCAT wind retrievals made on the forecast. These techniques included: geographical anomaly correlations, geographical forecast impact and vertical time series of forecast impact.

The results from the anomaly correlation calculations show neutral to modest

improvements in forecast skill in mid-latitudes in both seasons for most of the cases. The largest anomaly is consistent with where the anomaly correlation score is high for the case of January 2008, discrepancy occurs in Arctic ocean for the case of August 2007. Results from a modified forecast impact calculation reveals positive forecast impacts for the wind, temperature through 48 hours. The greatest forecast impacts occurred in the tropics and at 500 hPa which appears to be attributable to the deep upward momentum transport in tropical convection. It was also found in this study that small, positive forecast impacts are realized at all levels of the GFS through 48 hours.

Table 6.1. In-Situ data used within the NCEP Global Data Assimilation System for this study. Mass observations (temperature and moisture) are shown in the left column and wind observations are shown in the right column.

Rawinsonde temperature and humidity	Rawinsonde u and v
AIREP and PIREP aircraft temperatures	AIREP and PIREP aircraft u and v
ASDAR aircraft temperatures	ASDAR aircraft u and v
Flight-level reconnaissance and dropsonde temperature, humidity and station pressure	Flight-level reconnaissance and dropsonde u and v
MDCARS aircraft temperatures	MDCARS aircraft u and v
Surface marine ship, buoy and c-man temperature, humidity and station pressure	Surface marine ship, buoy and c-man u and v
Surface land synoptic and Metar temperature, humidity and station pressure	Surface land synoptic and metar u and v
Ship temperature, humidity and station pressure	Wind Profiler u and v
Pibal u and v	NEXRAD Vertical Azimuth Display u and v

Table 6.2. Satellite data used within the NCEP Global Data Assimilation System for this study.

HIRS sounder radiances	SBUV ozone radiances
AIRS radiances	QuikSCAT surface winds
AMSU-A radiances	GOES atmospheric motion vectors
AMSU-B radiances	Atmospheric motion vectors from GMS-5 until May 2003 than GOES-9 (MTSAT)
TRMM precipitation rate	METEOSAT atmospheric motion vectors
SSM/I precipitation rate	SSM/I surface wind speed
WindSat surface winds	ASCAT surface winds
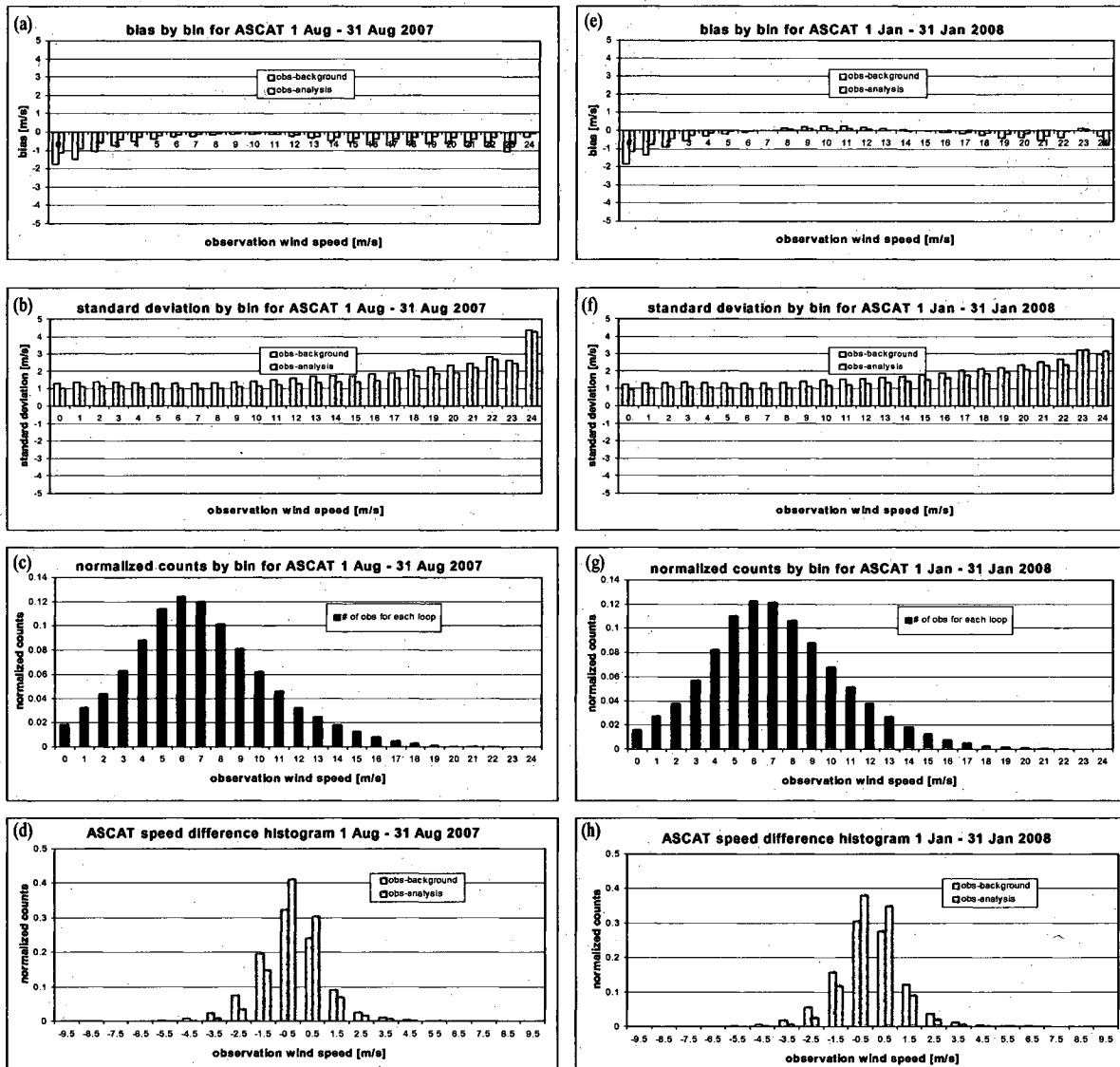
Figure 6.1. A comparison of the bias, standard deviation, wind speed histogram and ASCAT wind speed difference histogram for ASCAT data. Panels (a) – (d) show the results from August 2007 and panels (e) – (h) show the results from January 2008.
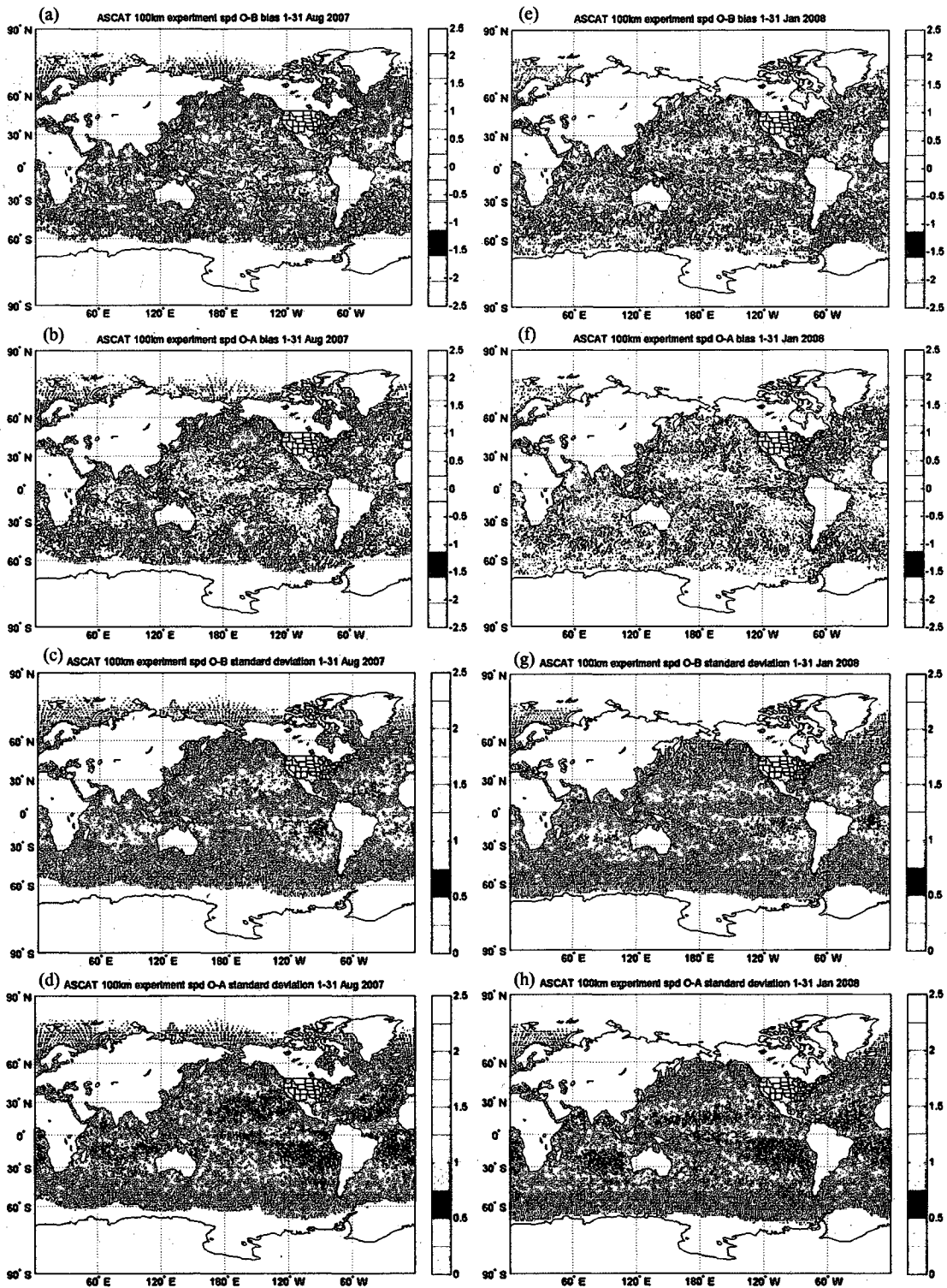
Figure 6.2. A comparison of the geographic distribution of bias, standard deviation (for both O-B and O-A) for ASCAT. Panels (a) – (d) show the results from August 2007 and panels (e) – (h) show the results from January 2008.

(a) 1000hPa AC Z day 5 control 1 Aug – 31 Aug 2007

(e) 1000hPa AC Z day 5 control 1 Jan – 31 Jan 2008
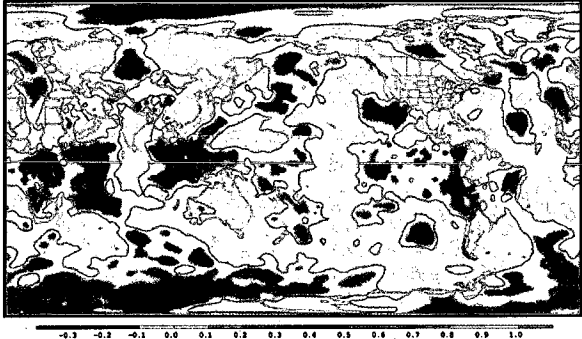
(b) 1000hPa AC Z day 5 ASCAT 1 Aug – 31 Aug 2007

(f) 1000hPa AC Z day 5 ASCAT 1 Jan – 31 Jan 2008
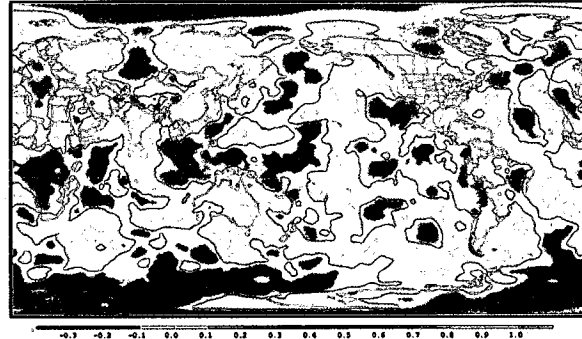
(c) 1000hPa AC Z day 5 ASCAT – control 1 Aug – 31 Aug 2007
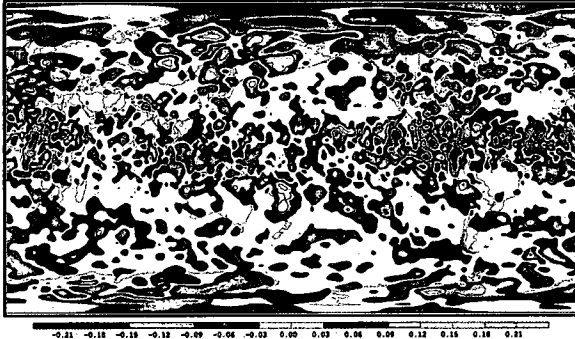
(g) 1000hPa AC Z day 5 ASCAT – control 1 Jan – 31 Jan 2008
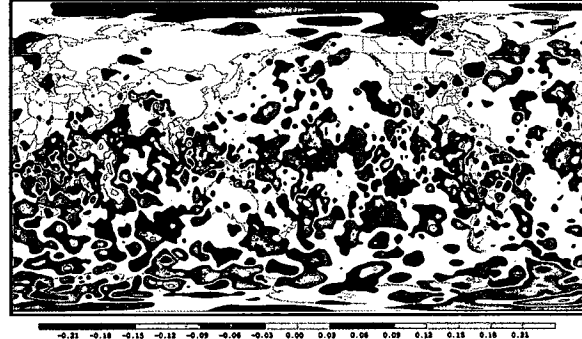
(d)

S. Hemisphere 1000 hPa AC Z 20S - 60S Waves 1-20
1 Aug - 31 Aug 2007

Control — ASCAT

Anomaly Correlation

Forecast [day]
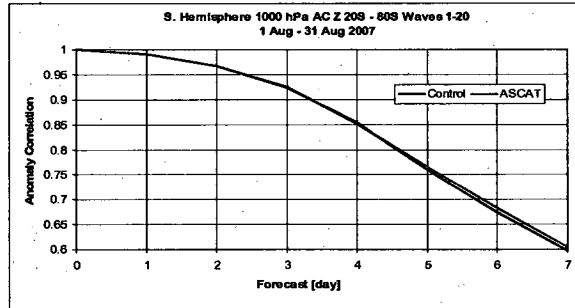
(h)

N. Hemisphere 1000 hPa AC Z 20N - 60N Waves 1-20
1 Jan - 31 Jan 2008

Control — ASCAT

Anomaly Correlation

Forecast [day]
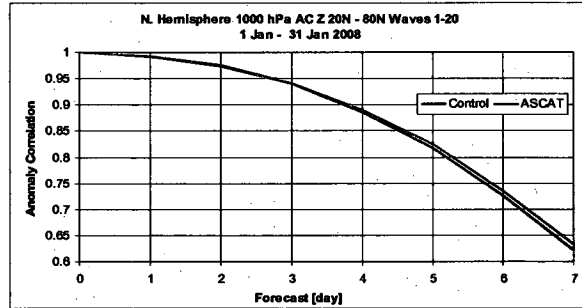
Figure 6.3. Panels (a) and (b) show the geographic distribution of anomaly correlation of day 5 for 1000hPa geopotential height from the control experiment and ASCAT experiment from August 2007. Panel (c) shows the difference between panels (a) and (b) using ASAT minus control. Panel (d) shows the anomaly correlation for days 0 to 7 for 1000 hPa geopotential height in the regions 20°-80° in the Southern Hemisphere. Panels (e) – (f) show the results from January 2008. For panels (d) and (h) the results have been truncated to only show results for waves 1 - 20.

(a) NCEP/NCAR Reanalysis
500mb Geopotential Height (m) Composite Anomaly 1968–1996 climo
Aug: 2007 to 2007

(c) NCEP/NCAR Reanalysis
500mb Geopotential Height (m) Composite Anomaly 1968–1996 climo
Jan: 2008 to 2008

(b) 500mb Geopotential Height 2D AC day 5 ASCAT Aug 2007

(d) 500mb Geopotential height 2D AC day 5 ASCAT Jan 2008
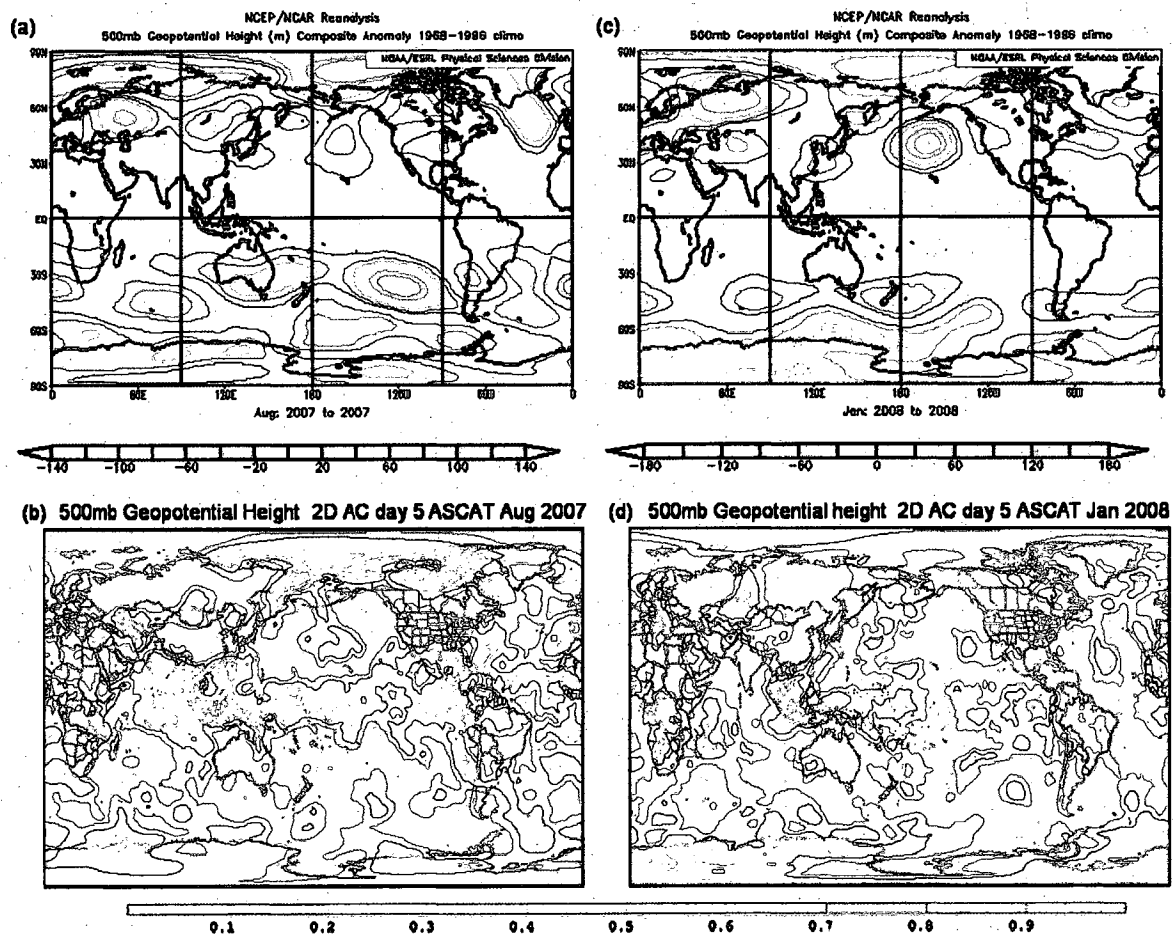
Figure 6.4. Panels (a) and (c) show the geographic distribution of 500hPa geopotential height (m) anomaly using NCEP/NCAR reanalysis for the month of (a) August 2007, and of (c) January 2008. Panels (b) and (d) show the geographic distribution of anomaly correlation of day 5 for 500hPa geopotential height from the ASCAT experiment from (b) August 2007 and from (d) January 2008.

(a) 10M WIND SPEED FCST IMPACT 6-HR ASCAT AUGUST 2007

(e) 10M WIND SPEED FCST IMPACT 6-HR ASCAT JANUARY 2008

(b) 10M WIND SPEED FCST IMPACT 12-HR ASCAT AUGUST 2007

(f) 10M WIND SPEED FCST IMPACT 12-HR ASCAT JANUARY 2008

(c) 10M WIND SPEED FCST IMPACT 24-HR ASCAT AUGUST 2007

(g) 10M WIND SPEED FCST IMPACT 24-HR ASCAT JANUARY 2008

(d) 10M WIND SPEED FCST IMPACT 48-HR ASCAT AUGUST 2007

(h) 10M WIND SPEED FCST IMPACT 48-HR ASCAT JANUARY 2008
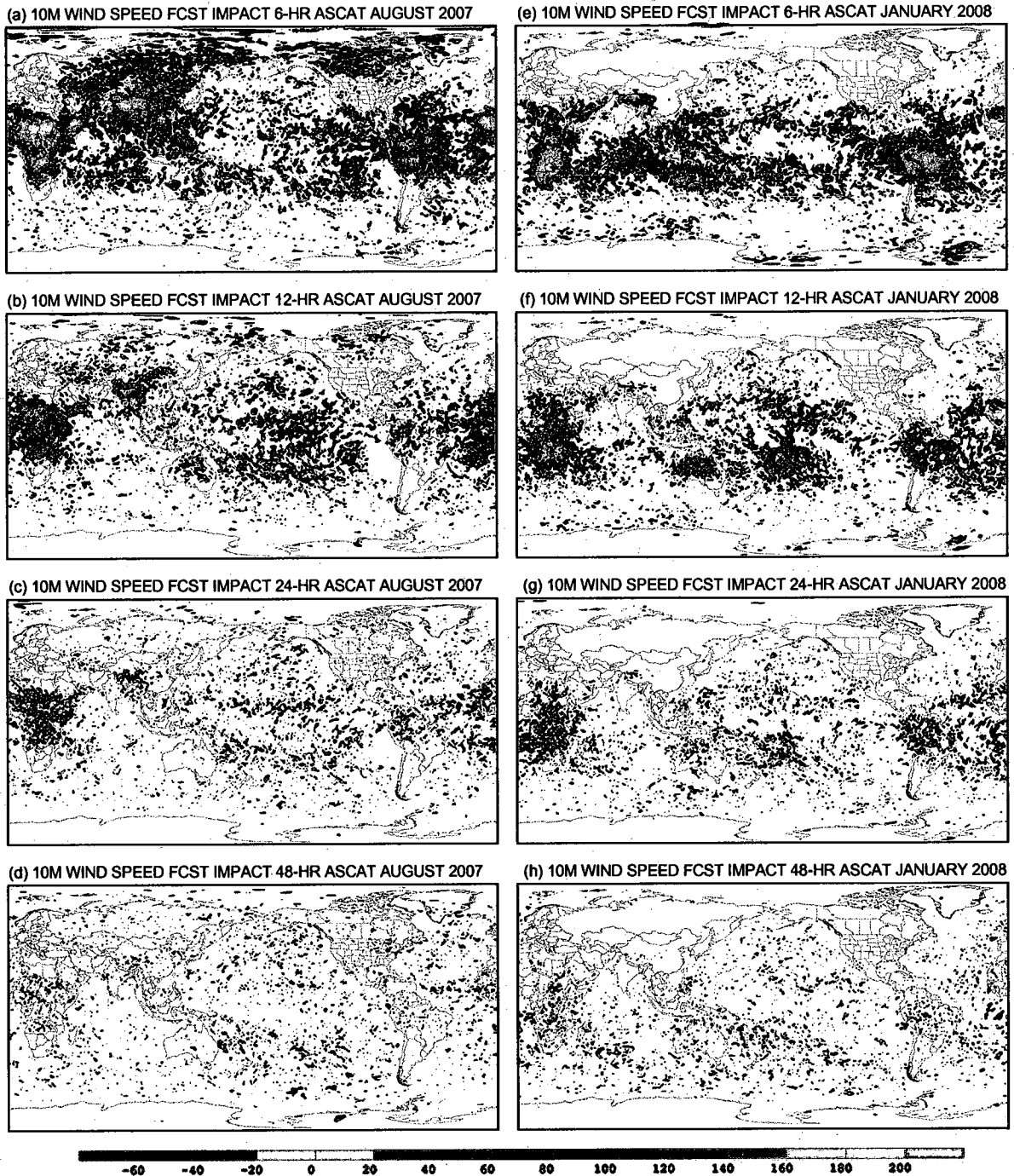
Figure 6.5. Geographic distribution of 10m wind speed Forecast Impact (%) at forecast hours (a) 6, (b) 12, (c) 24, and (d) 48 for August 2007 and forecast hours (e) 6, (f) 12, (g) 24, and (h) 48 for January 2008. The range of forecast impact is from -60 to +200.

(a) 500hPa WIND SPEED FCST IMPACT 6-HR ASCAT AUGUST 2007

(e) 500hPa WIND SPEED FCST IMPACT 6-HR ASCAT JANUARY 2008

(b) 500hPa WIND SPEED FCST IMPACT 12-HR ASCAT AUGUST 2007

(f) 500hPa WIND SPEED FCST IMPACT 12-HR ASCAT JANUARY 2008

(c) 500hPa WIND SPEED FCST IMPACT 24-HR ASCAT AUGUST 2007

(g) 500hPa WIND SPEED FCST IMPACT 24-HR ASCAT JANUARY 2008

(d) 500hPa WIND SPEED FCST IMPACT 48-HR ASCAT AUGUST 2007

(h) 500hPa WIND SPEED FCST IMPACT 48-HR ASCAT JANUARY 2008
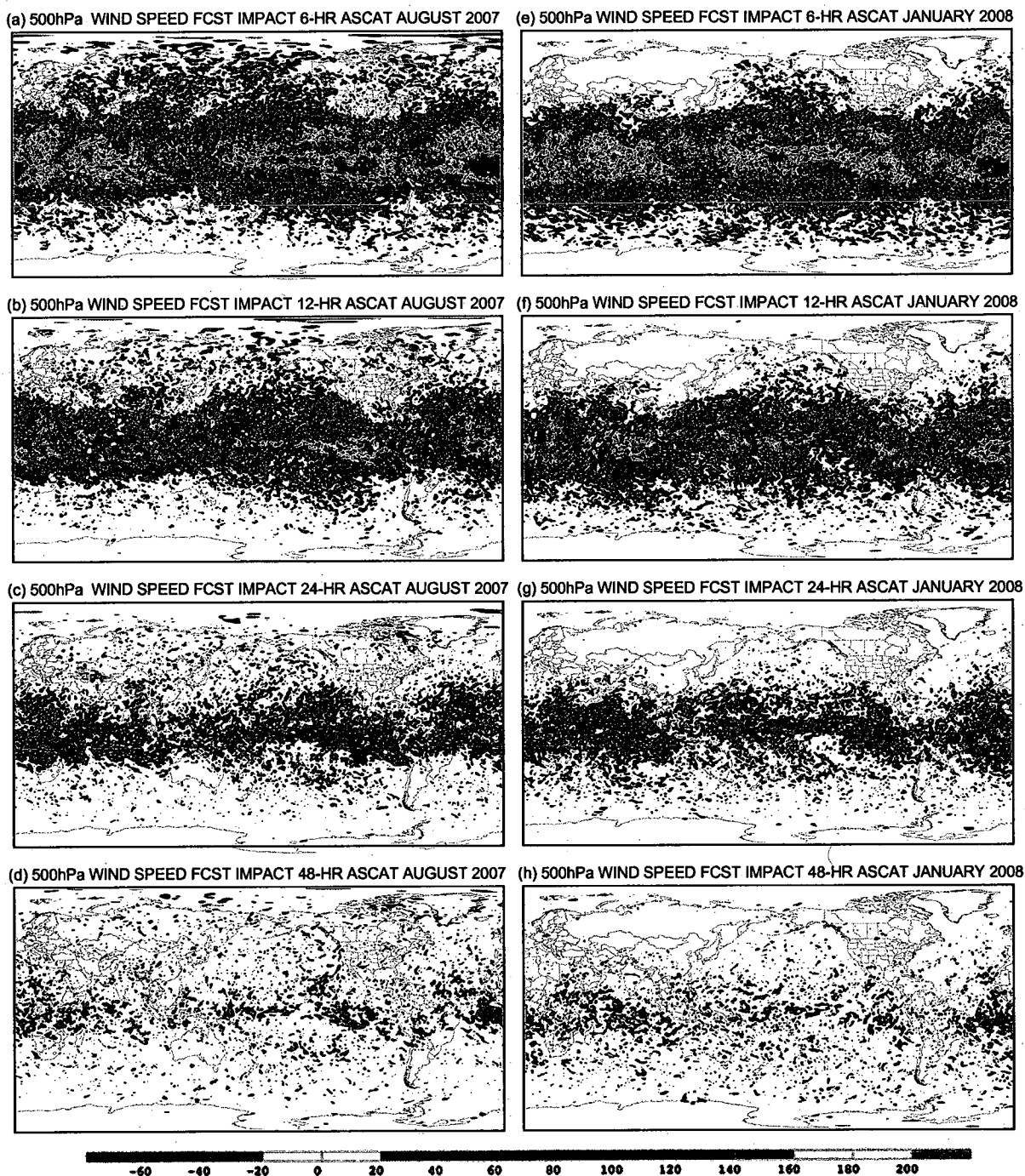
Figure 6.6. Geographic distribution of 500 hPa wind speed Forecast Impact (%) at forecast hours (a) 6, (b) 12, (c) 24, and (d) 48 for August 2007 and at forecast hours (e) 6, (f) 12, (g) 24 and (h) 48 for January 2008. The range of forecast impact is from -60 to +200.

(a) 1000hPa TEMP FCST IMPACT 6-HR ASCAT AUGUST 2007

(e) 1000hPa TEMP FCST IMPACT 6-HR ASCAT JANUARY 2008

(b) 1000hPa TEMP FCST IMPACT 12-HR ASCAT AUGUST 2007

(f) 1000hPa TEMP FCST IMPACT 12-HR ASCAT JANUARY 2008

(c) 1000hPa TEMP FCST IMPACT 24-HR ASCAT AUGUST 2007

(g) 1000hPa TEMP FCST IMPACT 24-HR ASCAT JANUARY 2008

(d) 1000hPa TEMP FCST IMPACT 48-HR ASCAT AUGUST 2007

(h) 1000hPa TEMP FCST IMPACT 48-HR ASCAT JANUARY 2008
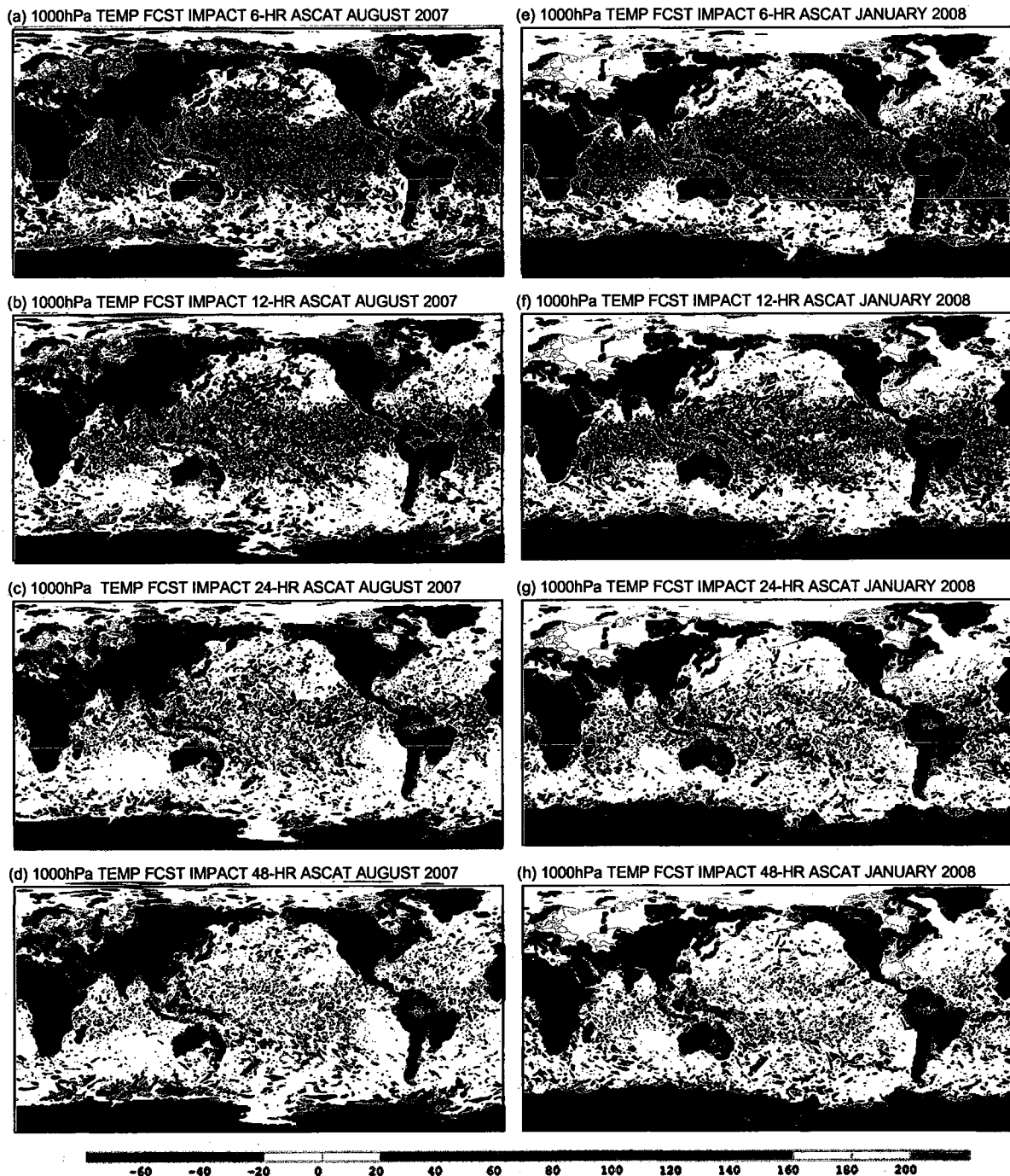
Figure 6.7. Geographic distribution of 1000 hPa temperature Forecast Impact (%) at forecast hours (a) 6, (b) 12, (c) 24, and (d) 48 for August 2007 and at forecast hours (e) 6, (f) 12, (g) 24, and (h) 48 for January 2008. The range of forecast impact is from -60 to +200.
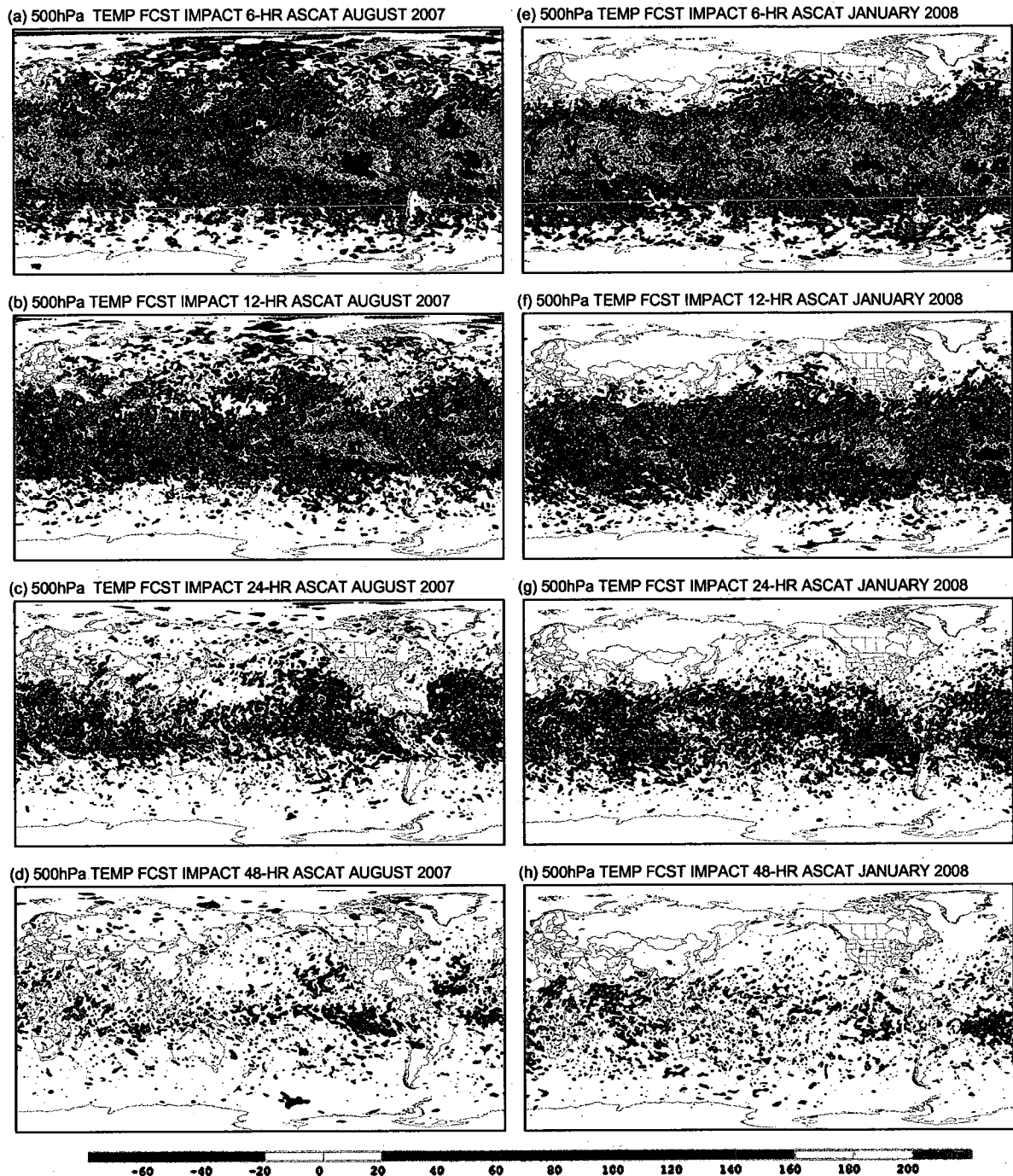
Figure 6.8. Geographic distribution of 500 hPa temperature Forecast Impact (%) at forecast hours (a) 6, (b) 12, (c) 24, and (d) 48 for August 2007 and at forecast hours (e) 6, (f) 12, (g) 24, and (h) 48 for January 2008. The range of forecast impact is from -60 to +200.
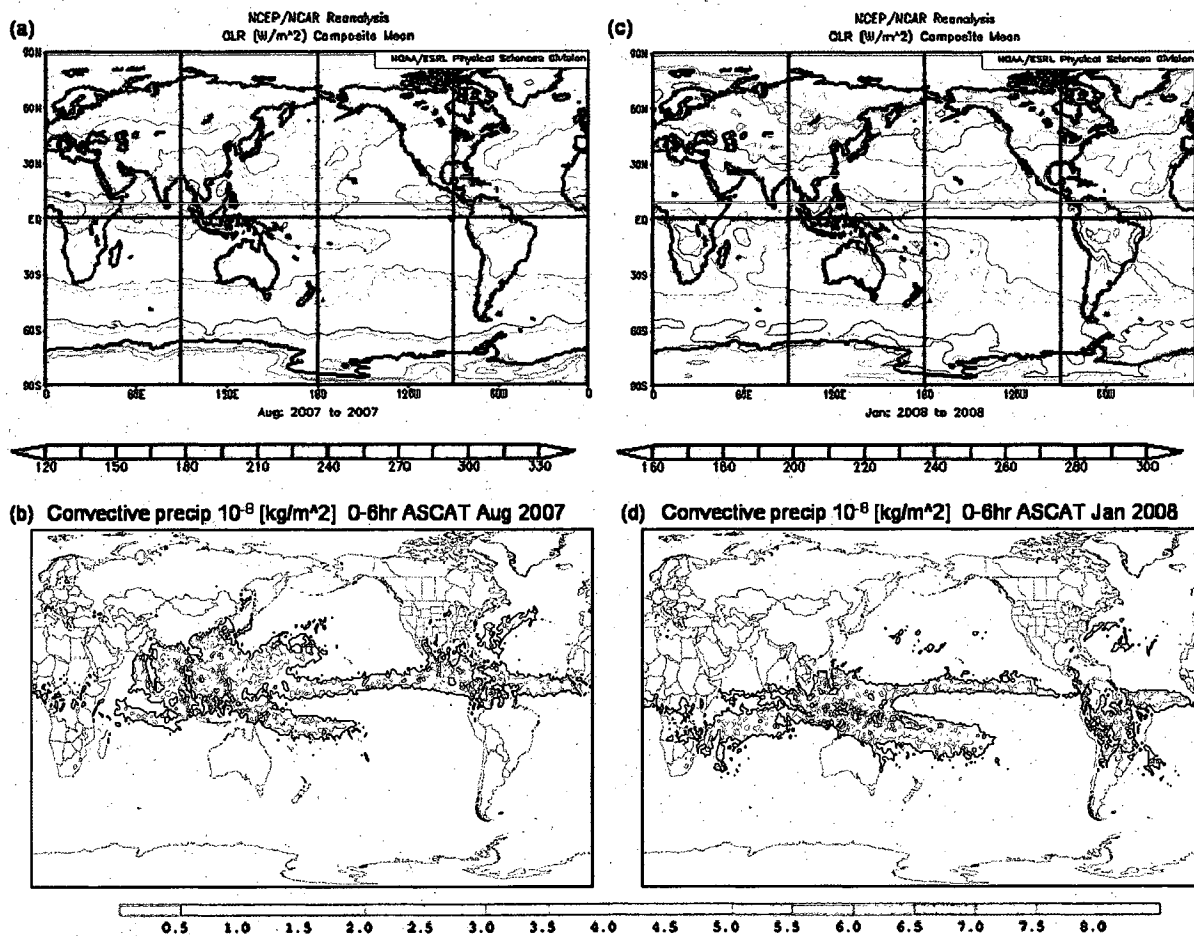
Figure 6.9. Geographic distribution of Outgoing Longwave Radiation (OLR) [w/m^2] mean using NCEP/NCAR reanalysis for the month of (a) August 2007, and of (c) January 2008. Geographic distribution of convective precipitation scale of 10^{-8} [kg/m^2] from 0-6hr forecast of ASCAT assimilation for the month of (c) August 2007, and of (d) January 2008.
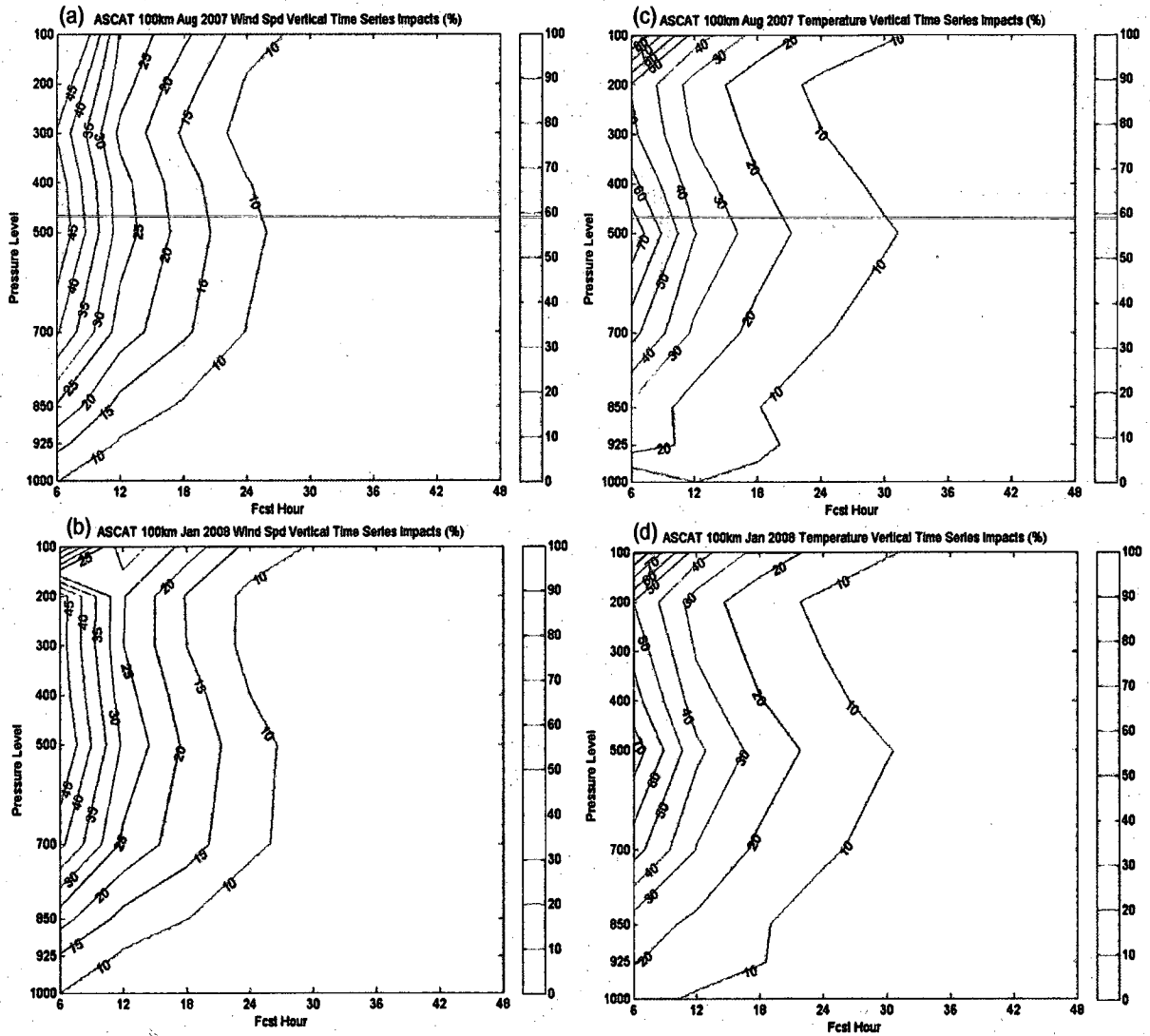
Figure 6.10. Vertical cross sections of Forecast Impact (%) on (a) wind speed and (b) temperature for August 2007 and Forecast Impact on (c) wind speed and (d) temperature for January 2008 as a function of pressure (hPa) and forecast time (hr) averaged over the globe. The colors have a uniform contour interval of 10%.
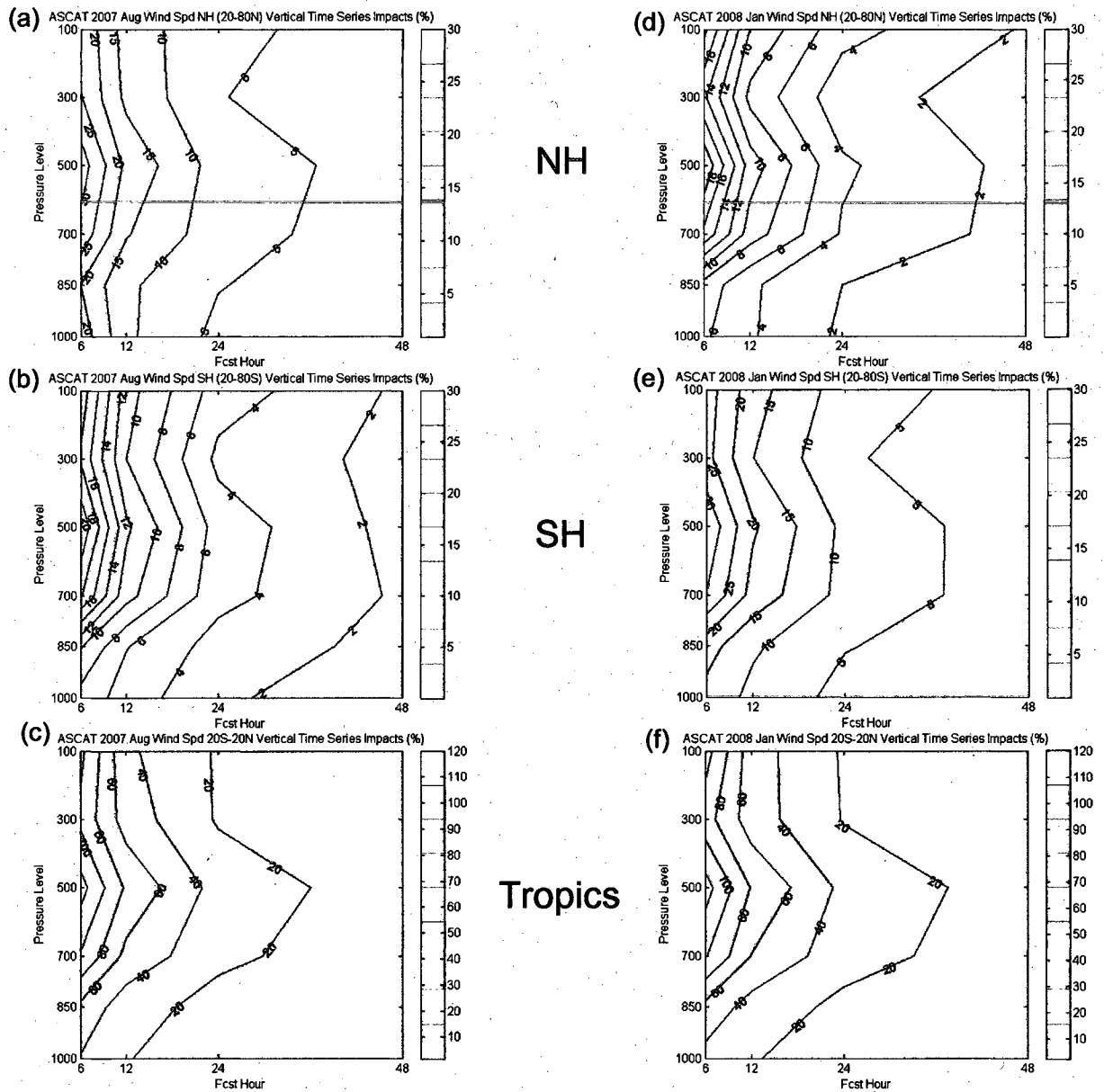
Figure 6.11. Vertical cross sections of Forecast Impact (%) for wind speed field over (a) Northern Hemisphere for August 2007 and (d) Northern Hemisphere for January 2008; (b) Southern Hemisphere for August 2007 and (e) Southern Hemisphere for January 2008; (c) tropics for August 2007 and (f) tropics for January 2008 as a function of pressure (hPa) and forecast time (hr).

Chapter 7: Case Assessments

In an operational setting, the evaluation of the impact of particular observations on numerical weather prediction model forecast skill must necessarily be viewed through the prism of statistical measures of forecast performance and not the data's impact on the success or failure of an individual forecast. The standard means of assessing a data set's operational utility involves calculating the statistical measures of forecast performance averaged over many time periods from parallel model runs in an quasi-operational environment. The data to be evaluated in these assessments "competes" with other operational data sets and the statistical diagnoses are used to determine whether assimilation of the new dataset improves the skillfulness of the forecast. If these statistical measures of forecast performance, like the anomaly correlation coefficient or forecast impact suggest neutral or increased skill and positive impact on prediction, the data is added to the mix of observations to be assimilated – perhaps without cognizance of why that data has the observed impact. The need to answer this question is not purely an academic one, as the answer could possibly suggest more efficient uses of the observational platform (i.e., reduced sampling), identify redundancies in the types of observations being assimilated, inform instrument designers of deficiencies in the observing system, or identify problems with the quality control and assimilation of the observations.

For this dissertation we attempted to perform diagnostic case studies to assess the forecast impact of assimilation of various data types for selected cases from the hundreds of model assimilation and forecast cycles considered in the earlier chapters of this dissertation. At the outset, the shear volume of output generated in the statistical assessment of skill would suggest a unique opportunity to study a number of cases in considerable depth; however, as will be seen in this chapter, the experimental design of the earlier work restricts our ability to directly determine how the assimilation of near-surface wind data influences a particular forecast. Specifically, the principal problem is that each experiment is essentially a comparison of two parallel runs of the GSI/GFS system: one using the operational data stream (the control), the other using the operational data stream in addition to the new observation (the experiment). The month-long, parallel, 6-hourly cycling of the analysis/forecast system virtually guarantees that the analyses and forecasts generated in the experiment are "saturated" with the new data. Any forecast improvement detected after the runs have spun up cannot be traced readily to the assimilation of a specific subset of observations. Moreover, simple differences between control and experiment analyses (and forecasts) are not useful as the differences represent not only differences in the differences between assimilated data but also accumulated differences between the parallel control and experiment runs. The denial of a request for additional resources to conduct conventional case studies relegated the work presented in this chapter to a limited assessment of forecast impact.

We chose the August 2007 control and experimental forecasts for the ASCAT near-surface winds study as the data set to use. The phenomenon chosen was the African

easterly wave. In this chapter we briefly describe the characteristics of these waves and why they would be a worthy phenomena to study. We then present two case assessments of the forecast impact of ASCAT and conclude with recommendations for what sorts of further tests could be performed.

7.1 Background on African easterly waves

African easterly waves (AEWs) are lower-tropospheric disturbances that travel westward across western Africa and the tropical Atlantic during the Northern Hemisphere summer. While these systems are widely believed to originate from both barotropic and baroclinic growth mechanisms within the West African Mid-tropospheric Easterly Jet (Burpee 1972; Rennick 1976; Thorncroft and Hoskins 1994; and references therein), more recent studies have suggested AEWs are in fact coherent vortical remnants of organized mesoscale convective systems originating over north Africa. Radiosonde observations from Dakar, Senegal and global meteorological analyses from the ECMWF indicate that these disturbances cross the west African coast approximately every 3-5 days (Burpee 1972; Reed et. al. 1988). Spectral analyses of the meridional-wind variance throughout the depth of the troposphere, based on time series at various radiosonde stations across central and western Africa, suggest that the AEW amplitude is strongest near 700 hPa and weakens with height (e.g., Burpee 1972). The meridional width of the vorticity perturbations typically extends across 20° of latitude, while the zonal length scale of these perturbations is of order 1000 km (Reed et al. 1977). These waves are of considerable importance as about 60% of the Atlantic tropical storms and minor

hurricanes (Saffir-Simpson Scale categories 1 and 2) arise from easterly waves, and nearly 85% of the intense (or major) Atlantic basin hurricanes have their origins from AEWs.

While an AEW is identified with a coherent (potential) vorticity maximum located at or near 700 hPa, the wave's influence extends down to the surface and is manifest as a sea level pressure trough and concomitant surface vorticity maximum. The circulation must necessarily reach the surface as the only viable mechanism for these waves to strengthen into tropical cyclones is through an air-sea interaction - as the winds associated with the AEWs access the energy existing in the thermodynamic disequilibrium between the ocean surface and the air just above the ocean surface. Given the importance of AEWs as seeds for Atlantic tropical cyclones and AEW's having a signature in the surface wind field, AEWs would seem to be a suitable candidate phenomena to study the potential impact of assimilation of ASCAT (and other near-surface winds).

We examine two cases of tropical cyclogenesis arising from AEWs from August 2007: the AEWs that eventually became Hurricanes Dean and Felix. While there are many analysis and forecast levels that could be considered in this assessment, we choose to focus on the surface (10 m) winds and associated vorticity for reasons of brevity and because it is anticipated that these levels are most readily impacted in the analysis.

7.2 Hurricane Dean

Major Hurricane Dean originated from a well-defined tropical wave that crossed the west coast of Africa on 11 August 2007. The wave was associated with a closed surface low even before entering the Atlantic, but strong easterly shear kept the system's convection displaced from an elongated circulation center for a couple of days. By about 0600 UTC 13 August, however, the circulation had become better defined and sufficiently connected to the deep convection for the National Hurricane Center (NHC) to consider the low a tropical depression about 350 n mi west-southwest of Praia in the Cape Verde Islands. At 0600 UTC 13 August, NHC's "best track" position of the newly declared depression was 12.2N, 28.9W with a minimum central pressure of 1006 hPa and maximum sustained winds of 30 kts. We consider three available analysis/forecast cycles (0000 UTC[1] on 10, 11, and 12 August 2007) prior to the declaration of depressions status.

Figure 7.1 shows the control (left panels) and experiment analyses (right panels) of surface (10 m) wind and vorticity calculated from that 10m wind for three separate model initializations valid 0000 UTC 10 August, 0000 UTC 11 August, and 0000 UTC 12 August. Inspection of each time reveals extremely small differences in wind speed and direction over the domain shown. On 0000 11 August, at the time the tropical wave moved off the west African coast, the vorticity maximum located at 10N 15 W defines the wave position. The experiment analysis has a slightly more intense vortex at this time. By 0000 UTC 12 August, the strengthened wave has moved westward to about 11N, 21.5

---

[1] Recall that the experimental design only allows for forecast to be generated beyond 6 hours for the 0000 UTC analysis. All other forecasts are 6 hours in length to provide for a background field for the next analysis cycle.

W. There are slight differences in the position of the vorticity maximum associated with the robust wave.

It is not obvious that the slight differences in the analyses could be attributed to differences in the data assimilated at the times shown in the Fig. 7.1. This is due to the incipient cyclone center's not being located in the data swath of ASCAT. Figure 7.2 shows the distribution of wind vectors from ASCAT swaths for all three analysis times shown in Fig. 7.1. In addition, the plots show the position of the wave on the 11th and 12th at 0000 UTC once it had moved offshore. It is clear from the position of the wave that the ASCAT passes did not directly contribute to informing the analysis of the structure of the wave, but may have helped define the environment surrounding the wave. Unfortunately, there were no nearby QuickSCAT swaths at these times to compare with the ASCAT data.

The forecasts, all valid at 0600 UTC 13 August, from the analyses in Fig. 7.1 are shown in Fig. 7.3. The verifying analyses are shown in the Fig. 7.4 along with the NHC best track position of the newly declared depression. All of the forecasts move the wave westward to near 12N, 30W. With the exception of the 78h experimental (ASCAT) forecast (Fig. 7.3d), all forecasted surface vorticity maximum are west of 30W by declaration time. As the wave was just emerging from the African coast at 0000 UTC 11 August, it is interesting to note that the forecast initialized at this time is an improvement over the forecast generated 24h earlier in terms of position and structure of the depression at declaration time – even though the ASCAT surface wind data did not sample the full structure of the wave (recall Fig. 7.2 b). We further note that the forecast generated

forecasts with lead times shorter than 30h appeared to have the position of the depression better than did the analyses at the declaration time.

7.3 Tropical Cyclone Felix

Felix formed from a tropical wave that moved off the coast of Africa on 24 August 2007. According to the NHC's Tropical Cyclone Report for AL062007, the wave moved westward across the Atlantic for several days while producing a persistent area of disorganized cloudiness and showers. The shower activity increased in organization beginning on 29 August accompanied by a gradual increase in low-level vorticity. It was estimated that a tropical depression formed around 1200 UTC 31 August about 195 n mi east-southeast of Barbados. The "best track" statistics for the depression that became Felix at declaration time placed the depression at 11.5N, 56.6W with a central pressure of 1009 hPa and maximum sustained winds of 25 kts.

The wave that would eventually become Felix was far weaker than the wave from which Dean developed. Figure 7.5 shows the surface winds and vorticity for the wave at one day intervals several days prior to tropical cyclogenesis. The wind field associated with the wave does not indicate an unambiguous closed circulation in either the control of experiment analysis (Figs. 7.5a and d). A day later, evidence for an unambiguous increase in organization is seen as a closed circulation and increase in vorticity is seen (Figs. 7.5b and e). The wave loses its closed circulation but maintains its intensity in the control analysis, while it has weakened considerably in the experiment analysis. (Figs. 7.5c and f).

The data swaths of the ASCAT data assimilated into the experiment run are shown in Fig. 7.6 for the analysis times shown in Fig. 5. Extrapolating backward the position of the vorticity maximum associated with the wave from the 29th and 30th backward to 0000 UTC the 28th, places the wave near or within an ASCAT data void. A day later, the wave remains along the edge of the data void, but east of the vorticity maximum there is clear evidence for cyclonic flow (Fig. 7.6b). By 0000 UTC 30 August, the ASCAT and QUIKSCAT data swaths overlap. An inspection of the wind field in the swaths near the alleged vorticity maximum, reveals more of an open wave in the wind field rather than a closed circulation. This data suggests that the ASCAT experiment analysis is closer to the observations. In particular note the southerly winds south of the control analysis vorticity maximum (Fig. 7.5c) at 10N, 47W. Neither the QUIKSCAT nor the ASCAT data support such a wind.

The forecasts generated from the analyses in Fig. 7.5 and valid at the time of tropical cyclogenesis (1200 UTC 31 August) are shown in Fig. 7.7. The verifying analyses are shown in Fig. 7.8. In general, all forecasts improve in terms of wave intensity and position as the lead time shortens. The control forecasts are generally more intense than the verifying analysis. The 84h experiment forecast has no cyclone or wave at genesis. At first glance, it might seem that the ASCAT data swath not resolving the wave at the initial time (recall Fig. 7.6a) led to this forecast "bust." Recall however that both forecasts, control and experiment, were initialized using the same observations, but had a different background (because of the many prior analysis cycles). Thus, while not conclusive, it may be that information from prior analysis cycles contributed to this poor

forecast. Subsequent experiment forecasts show increasingly better agreement with the verifying analysis (Fig. 7.8b).

Figure 7.8c shows the near-surface wind estimates from QUIKSCAT and ASCAT. The portions of the data swaths that appear to be missing observations are the regions for which the observations were rejected because of quality control requirements – most likely due to rain contamination. The lack of data in precipitating (likely convective) regions of the wave may reduce the usefulness of scatterometer data for developing tropical cyclones as the circulation of the wave may not be well sampled due to discarded, rain contaminated wind vectors.

7.4 Discussion

Comparisons between control and experiment analyses for two cases of tropical cyclogenesis emerging from African easterly waves reveals subtle differences. From these subtle differences, forecast differences do emerge, and in some cases the differences are striking (e.g., Figs. 7.7 a and d). That these differences are small and cannot be directly attributable to specific data assimilated during a particular assimilation time suggests that synoptic diagnoses of forecast impact for particular events, using the output from the skill/impact assessment experiments, remains a challenge. The questions that one would like to address is "How are the skill improvements and forecast impacts described in earlier chapters manifest for particular weather systems?" and "What new information does assimilation of the near surface winds bring to an analysis?" These data collected in the evaluation of the WindsSat and ASCAT retrieved winds cannot answer

these questions. However, an exciting "middle-ground" possibility exists: a seasonal evaluation of forecast skill for tropical cyclogenesis (measured by false alarm rate statistics) could be conducted to compare the skill of forecasts with and without the ASCAT data. The existing data is ideal for such a statistical study, but also provides information useful in looking at an ensemble of realizations of tropical cyclogenesis. Composites of the forecast "successes" and "busts" could be performed to determine the characteristics of the environment within which the tropical cyclones are favored (or not favored) to form. If adjoints of the GFS and GSI were to exist, one could use differences in the forecasts to track down differences in the analyses, and ultimately evaluate sensitivity of the forecast differences to the input data *for a particular assimilation time*. The small difference observed in the analyses will be see to be not necessarily be relevant for the forecasts. Ultimately, however, if one wished to perform a meaningful synoptic diagnosis of the impact of the near-surface wind assimilation, a data denial experiment would be required. It is recommended that computer resources be increased modestly to allow for proper case studies to be conducted.

CONTROL   **EXPERIMENT**

Figure 7.1. Control (left panels) and experiment (right panels) analyses of 10m wind and 10m vorticity valid at 0000 UTC 10 August 2007 (a) and (d); 0000 UTC 11 August 2007 (b) and (e); and 0000 UTC 12 August 2007 (c) and (f).

Figure 7.2 ASCAT wind vector estimates at (a) 0000 UTC 10 August 2007, (b) 0000 UTC 11 August 2007, and (c) 0000 UTC 12 August 2007. The 'L' indicates the location of the vorticity maxima associated with the easterly save in the analysis.

CONTROL **EXPERIMENT**
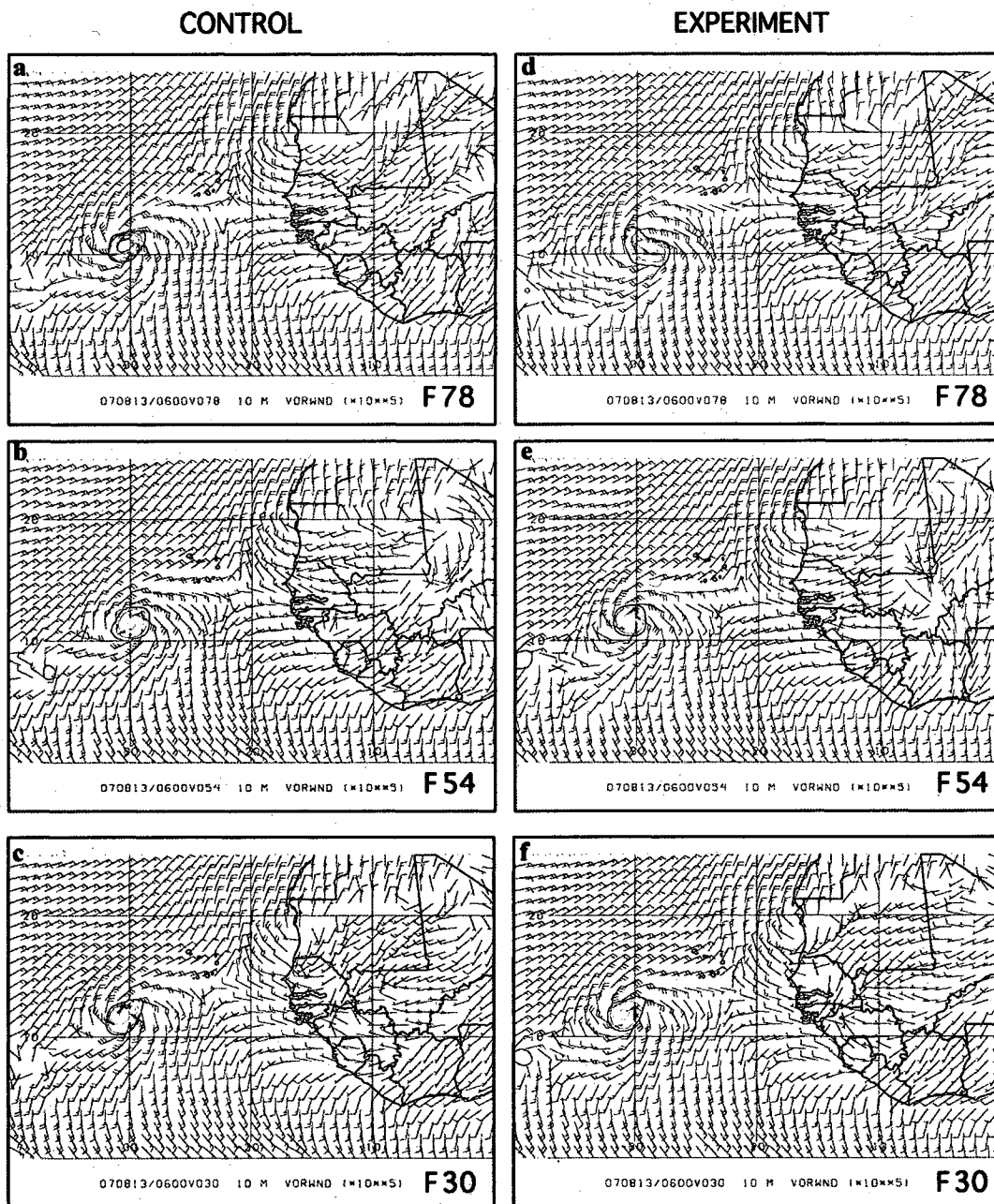
Figure 7.3. Control (left panels) and experiment (right panels) forecasts of 10m wind and 10m vorticity all valid for 0600 UTC 13 August 2007 initialized at (a) and (d) 0000 UTC 10 August 2007; (b) and (e) 0000 UTC 11 August 2007; and (c) and (f) 0000 UTC 12 August 2007.

Figure 7.4. (a) Control and (b) experiment analysis valid 0600 UTC 13 August 2007. 'X' marks NHC position for tropical depression that would eventually become Dean.

CONTROL **EXPERIMENT**
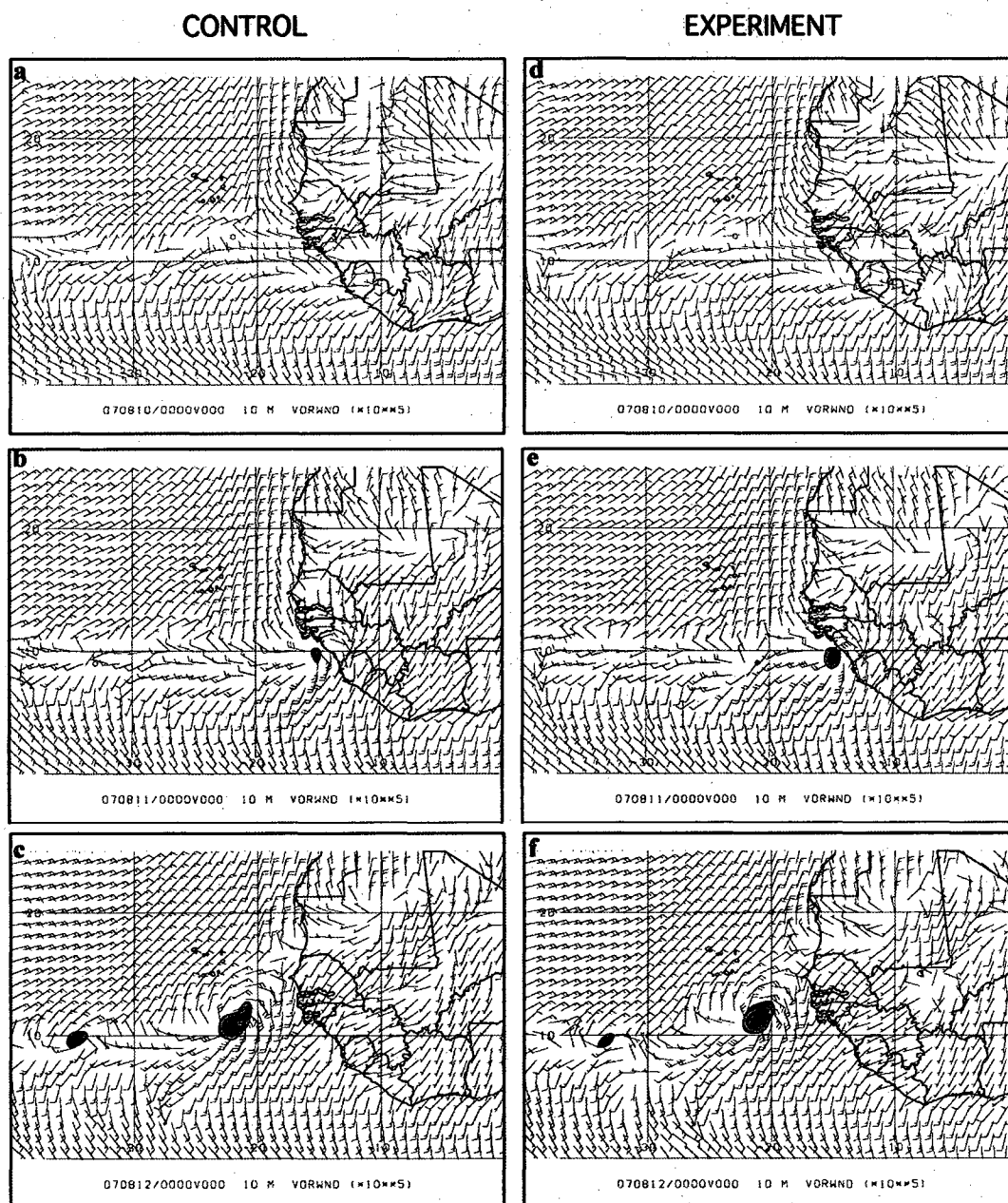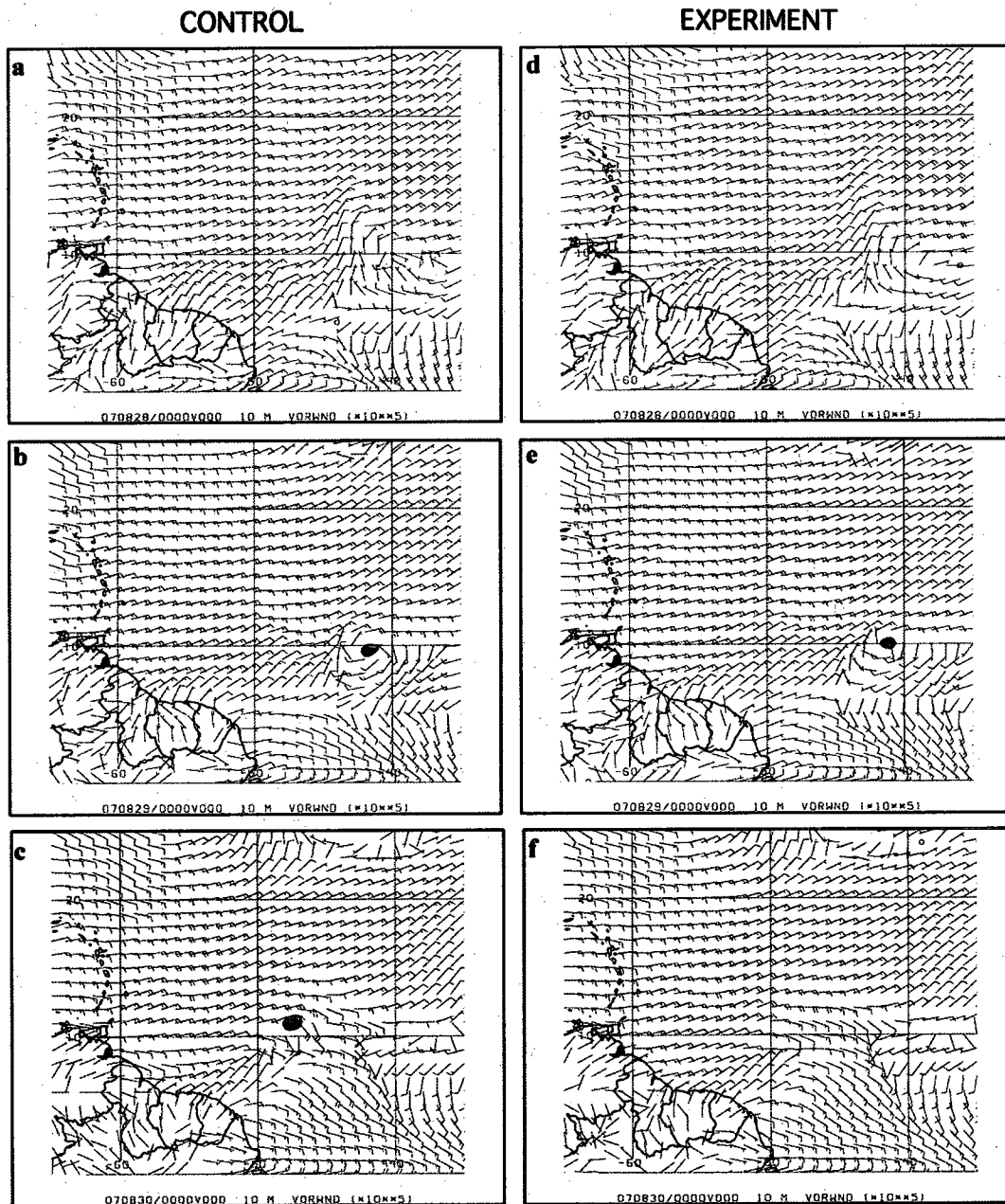

Figure 7.5. Control (left panels) and experiment (right panels) analyses of 10m wind and 10m vorticity at 0000 UTC on (a) and (d) 28 August 2007; (b) and (e) 29 August 2007; and (c) and (f) 30 August 2007.
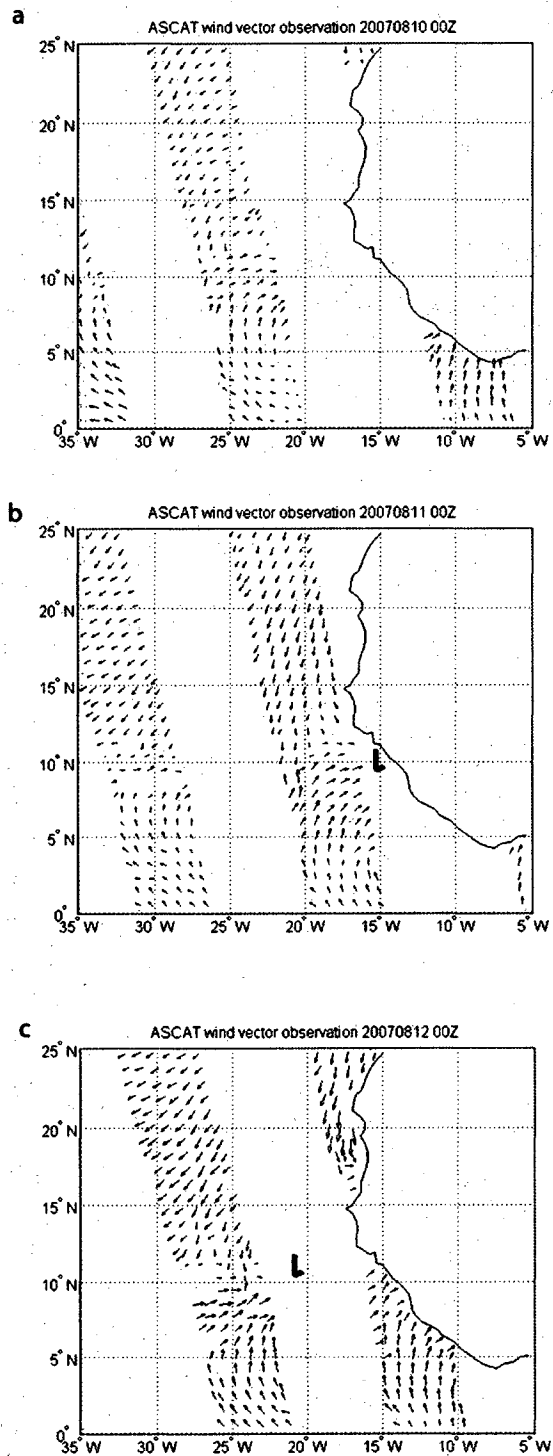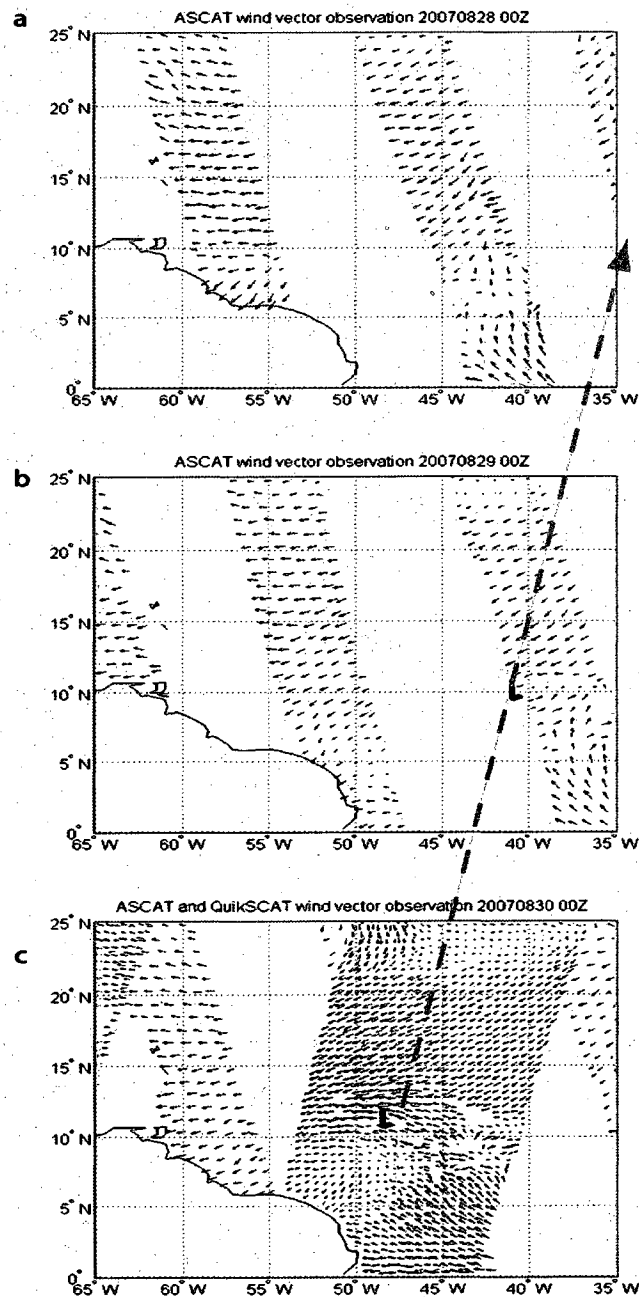
Figure 7.6. ASCAT wind vector estimates at (a) 0000 UTC 28 August 2007, (b) 0000 UTC 29 August 2007, and (c) 0000 UTC 30 August 2007. The 'L' indicates the location of the vorticity maximum in the experiment analysis, while in (c) the 'L' indicates the location of the vorticity maximum in the control analysis. Dashed arrow used to extrapolate wave position backward in time.

CONTROL
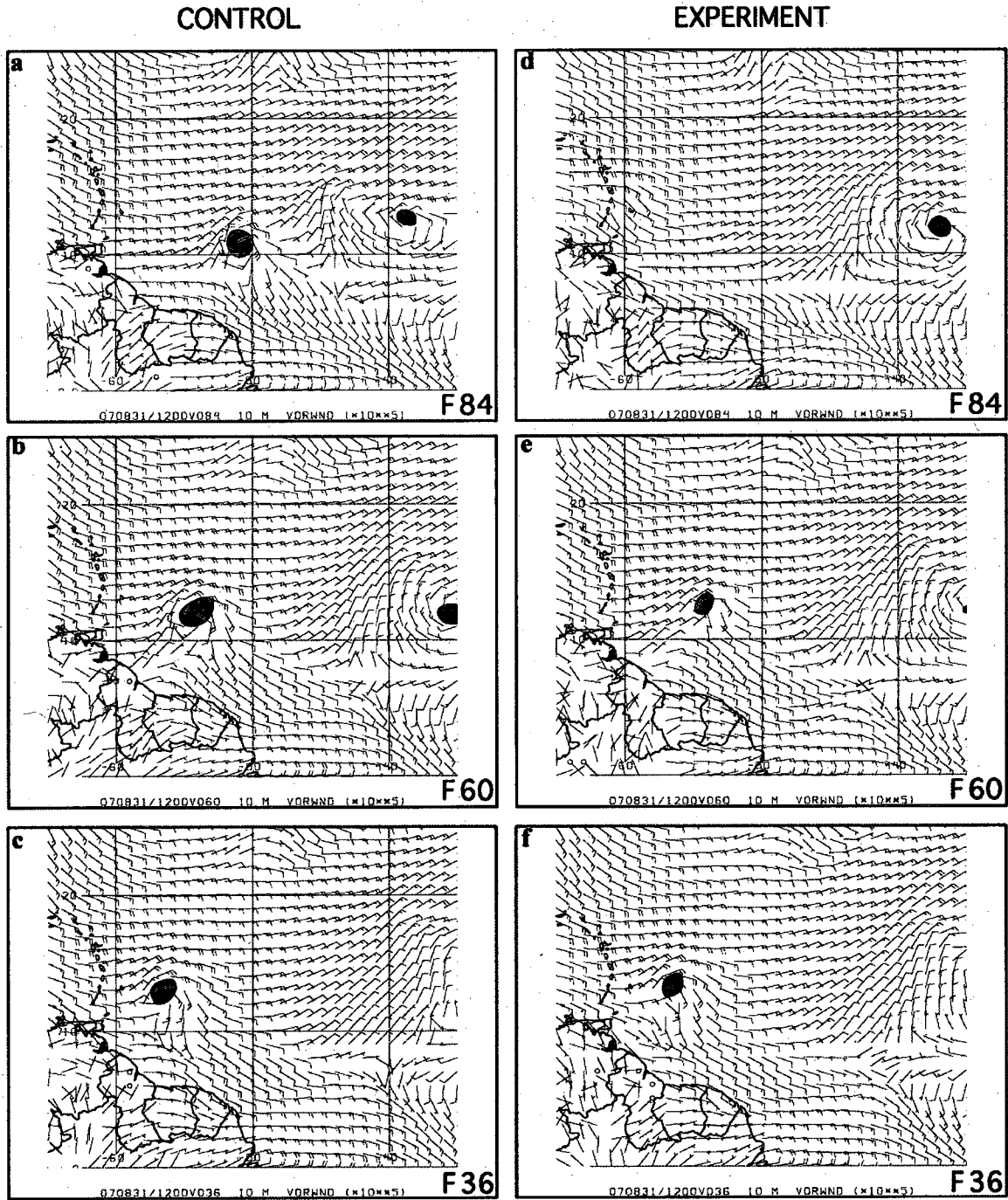
EXPERIMENT

Figure 7.7. Control (left panels) and experiment (right panels) forecasts of 10m wind and 10m vorticity all valid for 1200 UTC 31 August 2007 initialized at (a) and (d) 0000 UTC 28 August 2007; (b) and (e) 0000 UTC 29 August 2007; and (c) and (f) 0000 UTC 30 August 2007.
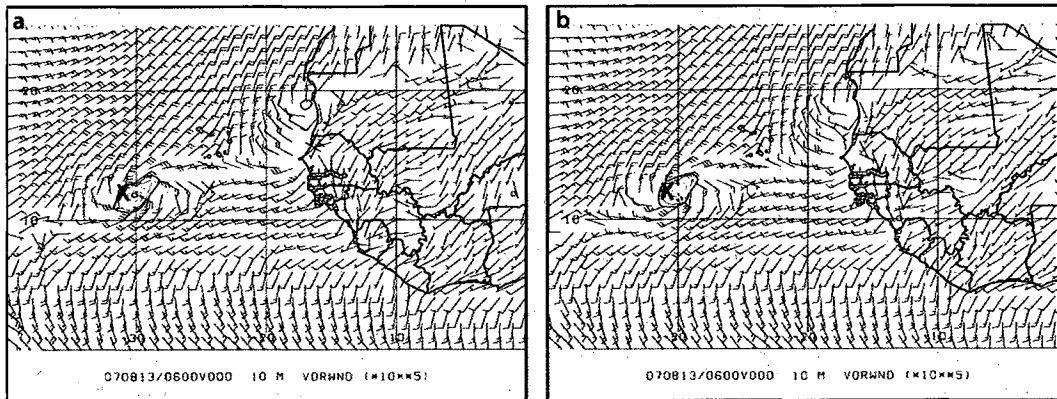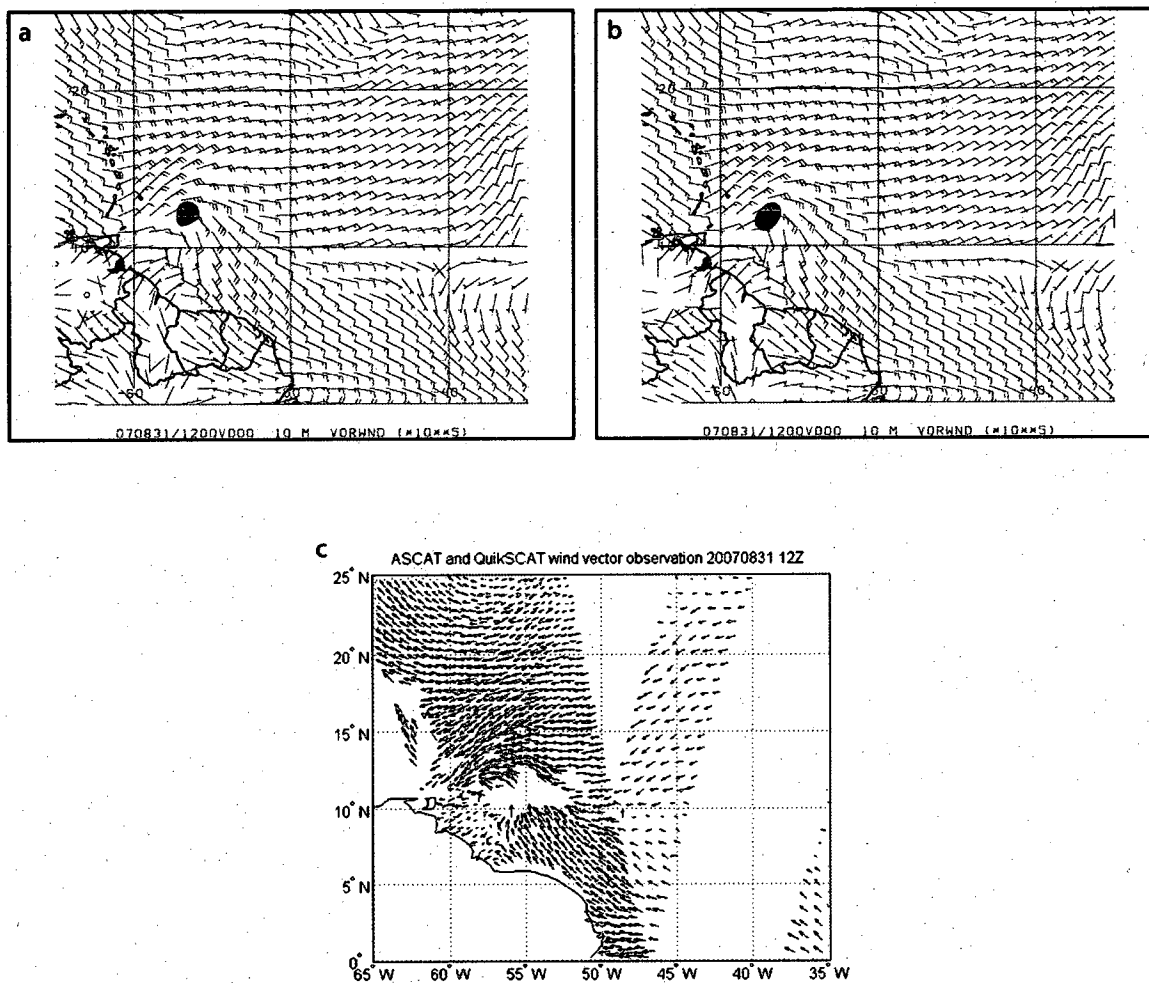
Figure 7.8. (a) Control and (b) experiment analyses of 10m wind and 10m vorticity valid for 1200 UTC 31 August 2007; (c) QuikSCAT (green) and ASCAT (red) wind vector estimates also valid 1200 UTC 31 August.

Chapter 8 Summary and Conclusions

8.1 Summary of ASCAT/WindSat Assimilation

We have worked with JCSDA (Joint Center for Satellite Data Assimilation) personnel to evaluate assimilation techniques and the forecast impact of assimilating ASCAT and WindSat data into the National Center for Environmental Prediction (NCEP) Global Data Assimilation/Global Forecast System (GDAS/GFS). We have developed the quality control (QC) procedures for the assimilation of ASCAT and WindSat data and modified NCEP's Gridpoint Statistical Interpolation (GSI) software to test a thinning routine for the ASCAT winds. We have conducted a two season ASCAT and WindSat assimilation experiment, testing and comparing the attributes of using the ASCAT and WindSat data. We have been working with JCSDA on thinning resolution selection and assimilation weights for the ASCAT and WindSat data. After the two season surface winds experiments were completed, we compared the attributes of forecasts using the ASCAT and WindSat data to a set of control forecast experiments by computing the geographic distribution of Forecast Impact (FI) in addition to using NCEP's verification software to quantify forecast impacts. Ultimately these efforts have lead to operational implementation of WindSat data in the NCEP weather forecast models in the Fall 2008 GSI release and will lead to operational implementation of ASCAT data in the NCEP weather forecast models in the 2009 GSI release.

8.2 Summary of Accomplishments

Procedures outlined by NCEP to transition new data types into operations were used for the performed experiments. The transition steps are outlined as follows (http://www.emc.ncep.noaa.gov/TransitionToOp/TransitionProcess/Transition_Steps_(M odeling).pdf):

- Identification for selection

- Code/Algorithm assessment and/or development

- Interface with operational codes

- Level I: Preliminary testing (lower resolution)

- Level II: Preliminary testing (higher resolution)

- Environmental Modeling Center (EMC) pre-implementation testing (packaging/calibration)

- NCEP Central Operations (NCO) pre-implementation testing

- Implementation/delivery

WindSat and ASCAT sensors have been selected by NCEP as potential substitutes for the QuikSCAT sensor. In this study, our efforts on the code assessment and QC development as well as the interface with operations codes have lead to the operational implementation of WindSat and ASCAT data in the NCEP weather forecasting model. We performed both level I (lower resolution) and level II (higher resolutions) experiments, all software used by the WindSat and ASCAT quality control and other work that help with the WindSat and ACSAT assimilation were made available to NCEP for the purpose of EMC/NCO pre-implementation testing. As aforementioned,

these efforts have lead to operational implementation of WindSat data in the Fall 2008 GSI release and will lead to operational implementation of ASCAT data in the 2009 GSI release.

The operational version of NCEP's global forecast model at the current operational resolution was used. The December 2007 version of NCEP's GSI and its associated scripts were modified to read, spatially thin, and assimilate the ASCAT data and January 2007 version for WindSat data. The control simulation contains all of the NCEP operational data. The experiment simulation contains all of the NCEP operational data and includes the ASCAT/WindSat sea surface wind observations. Quality Control (QC) and thinning procedures were derived. These QC procedures for ASCAT and WindSat data are similar. Most of the QC of the WindSat and ASCAT data was accomplished in the retrieval process. Observations that fail the retrieval process or are flagged for rain, land, sun glint, Radio Frequency Interference (RFI), or sea ice contamination were flagged in the EDRs and omitted from the super-obs. Additional quality control procedures were added within GDAS/GFS and includes:

- Observations not within +/- 3 hours of the synoptic time and observations near coasts were not used.

- For the WindSat winds, if the absolute value of the super-ob'd wind component differs from the corresponding background wind by more than $6ms^{-1}$ or the wind speed was not between $4ms^{-1}$ and $20ms^{-1}$, the super ob wind vector was removed.

- For the ASCAT winds, to remove additional data suspect of being contaminated by sea ice, a Sea Surface Temperature (SST) of 273K was used as a criteria. Observations near coastlines were also not used.

- For the ASCAT winds, if the absolute value of the thinned wind component differs from the corresponding background wind by more than $5ms^{-1}$ or the observed or model background wind speeds were greater than $20ms^{-1}$, the wind vector was removed.

The two periods used for these simulations were from 1 July to 31 August 2007 and from 1 December to 31 January 2008 for the ASCAT experiment, and from 1 October to 31 October 2006 and from 1 March to 31 March 2007 for the WindSat experiment.

For WindSat winds assimilation, data thinning was achieved using "super observations" (or "super-obs"). Tests were run to determine whether one degree or one-half degree latitude, longitude averaging boxes were more effective. It was found that overall the one degree boxes gave the best forecast results in terms of the anomaly correlation statistics. The largest biases with respect to the background are found over the Central Pacific and Indian Ocean, as expected the biases are significantly reduced in most regions after assimilating the data.

For ASCAT winds assimilation, data thinning experiments were conducted at 150, 100, and 50 km resolutions. ASCAT thinned to 100 km had the best overall results. Large observational errors were found in the ASCAT data near coasts and in regions of sea ice. These observations were rejected by our QC criteria. Various assimilation

weights were also tested. Observational errors of 3.5 ms^{-1} produced the best overall results. All software modifications made to assimilate ASCAT are available to NCEP and other operational centers.

8.3 Summary of Findings

Observing system experiments were conducted during two seasons to quantify the impacts of assimilating the surface wind retrievals from the WindSat microwave sensor on the Coriolis satellite. A January 2007 version of the NCEP GDAS/GFS was used for WindSat assimilation and a December 2007 version was used for ASCAAT assimilation. These experiments were conducted at the NCEP operational resolution of the time (T382 with 64 layers) and used the NCEP operational observation database.

The results of these experiments were:

- Anomaly correlation show neutral to modest increase in forecast skill at mid-latitudes in both seasons for wind and temperature from 6 hour forecast and beyond.

- The 500mb geopotential height monthly anomaly plots for ASCAT August 2007 plots shows the largest anomalies are noted in Arctic Ocean, a band in the south Pacific off South America. The largest anomalies in the south Pacific region coincide with the large values of AC in the same region, while the large anomalies do not correspond with the large values in Arctic Ocean in the 2D AC plot. For the month of January 2008, largest anomaly is noted in north Pacific and east Russian, where the 2D AC plot also shows large AC.

- Large forecast impacts for both sensors occurred in the tropics and at 500 hPa for the wind speed and temperature field.

- Inspection of the vertical time series of the horizontally averaged forecast impacts from both seasons for WindSat and ASCAT experiment reveals similar results. Forecast impacts from the wind speed and temperature fields are shown for both seasons. Inspection of the plots reveals that the largest impacts are at the 500hPa level and is consistent with the geographic Forecast Impacts. Large impacts are also shows at 100hPa. All panels display a systematic decrease of FI with time.

- The largest anomaly is consistent with where the anomaly correlation score is high for the case of January 2008, discrepancy occurs in Arctic ocean for the case of August 2007.

8.4 Problems with this approach

There are problems with this approach in terms of experimental design. Due to the very limited computer resources in the NCEP machine, we are unable to perform necessary denial experiments (i.e., turning off all the other surface winds including QuikSCAT winds and near surface GOES winds), so that it is difficult to distinguish the impacts from WindSat/ASCAT alone with the effects from QuikSCAT winds. Additional computing resources have been requested to conduct a series of denial experiments. We think it would be a better approach to "turn off" all the other surface wind vectors including QuikSCAT and WindSat winds, to perform an impact experiment with ASCAT winds only. One of the major comments from the reviewers of our WindSat manuscript is the requirement for synoptic case studies to directly assess the impact from assimilating surface winds. It is worthwhile to evaluate the impacts of the ASCAT winds in the hurricane season by evaluating the impact of assimilating ASCAT data on tropical cyclogenesis from African easterly waves. Given that easterly waves are lower tropospheric features, and that some analysts have suggested that lower tropospheric winds derived from scatterometer data are helpful in tracking such disturbances, we feel that case studies evaluating the genesis of tropical cyclones from easterly waves may allow us to understand the impact of these winds on the forecast fields of other variables at other levels.

In the current set up for the experiment design, the first two weeks of model spin-up have been eliminated. This strategy works may be suitable for long term evaluation of

model performance statistics for a given data set, but are insufficient for evaluating and understanding the day to day impact of a given data set on forecast skill. Problems associated with this two weeks model spin up time is that for the purpose of case study, since we are not running a single assimilation, information from the previous cycles is carried over and spread out. It is difficult to distinguish impacts from assimilating wind observations at a particular time and the impacts from previous assimilations. One possible means to address this problem is by turning off all the other surface winds observations, assimilate the ASCAT data two or three days before a particular synoptic development (i.e., tropical depression genesis), running the model forward until the time of tropical storm dissipated. It will be ideal to have parallel runs suggested as follows:

- Normal control runs with all the data included from the operational database.

- Denial experiment without QuikSCAT data.

- Denial experiment without QuikSCAT data and lower GOES winds.

- Experiment runs with control database plus surface winds observations (ASCAT or WindSat winds).

By performing the aforementioned parallel denial experiments, we can assess better what is the impact of assimilating ocean surface winds observations from a particular instrument on the GFS model. Analysis from each denial experiment can be interpolated to the observation location, O-A can be calculated for a particular instrument without the influence of other sensors. Better quality control for the wind observations can be evaluated after the proposed denial experiment, problems like wind speed ambiguity removal, land-sea flag can also be addressed and resolved better. By

evaluating the influence of a particular sensor's observation to the analysis can also aid with the determination of observation error coefficient weighting and establish the bias correction for each sensor.

8.5 Future work

We plan to accomplish the following task objectives in 2009:

We propose to continue developing the quality control (QC) procedures for ASCAT retrieved winds. From our experience in working with QuikSCAT and WindSat retrieved winds, the cut-off criteria in the quality control for the retrieved winds should be determined based on the statistical results of rms or bias of the innovation (observation minus background) data. The results from our ASCAT assimilation indicated that it is essential to evaluate raw observations and perform rigorous data quality control before the data are ingested into the assimilation system. The current quality control we used for ASCAT winds is: if a retrieved wind deviates from the corresponding background wind field by more than $5ms^{-1}$, the wind vector will be rejected. This QC removes the data that deviates significantly from the background field. But there are still problems with some wind vectors. As an example, consider Fig. 8.1a which displays the ASCAT (in red) and QuikSCAT (in green) wind vector observations at 1200 UTC 31 August 2007. The retrieved 10 meter winds from ASCAT and QuikSCAT are in good agreement in terms of wind speed and wind direction for most of the overlap tracks, but discrepancies occur in the band of 55°-60° west and 5°-10° north. In this region, we find directional differences

of as much as 90° in co-located ASCAT and QuikSCAT wind vectors. This time period is coincident with the genesis of a tropical depression which eventually became Hurricane Felix. Some wind observations may be contaminated by rain, proximity to coast, etc. Although there are quality control procedures in the retrieval process to reject some of these data, it seems more QC should be used before the data are assimilated.

Another important data quality control problem for the ASCAT, QuikSCAT, and WindSat retrieved vector winds is removal of the wind direction ambiguity. Currently, the ambiguity removal for the wind vector retrieval algorithm is based on the model forecast. In particular, the NCEP GFS forecast has been used for the ambiguity removal at the National Environmental Satellite, Data, and Information Service (NESDIS). Figure 8.1b displays the analysis wind field at 10 meter for 1200 UTC 31 August 2007. In Fig. 8.1a the surface wind field from the ASCAT/QuikSCAT observation and GFS analysis agree well except in the vicinity of the likely vorticity maximum at 12°N 56°W. The analysis wind field shows southeasterly winds which converge to the center of the low, even along the coast line. There is no clear southerly component of the wind from the ASCAT or QuikSCAT observations from 57°-60° west, 6°-10° north. To have a better understanding of this, we propose to look at all the wind vectors retrieved from the ASCAT and QuikSCAT wind, and thereby find an optimal way to guide the wind vector selection.

From our earlier work, it has been demonstrated that the influence of assimilation of ASCAT surface winds propagates upward through the depth of the troposphere in the GFS. We will focus on identifying why this upward propagation occurs. If time permits,

as the next step to better understanding how the surface wind vectors are assimilated into the GSI system. We propose to work on the GSI code to investigate if the interpolation of the surface observation to the model background (both vertically and horizontally) is working appropriately and vice versa.

We request computing resources to conduct a series of denial experiments. We propose to turn off all the other surface wind vectors including QuikSCAT and WindSat winds, to perform an impact experiment with ASCAT winds only. We propose to evaluate the impacts of the ASCAT winds in the hurricane season by evaluating the impact of assimilating ASCAT data on tropical cyclogenesis from African easterly waves.

While we view making the most use of the retrieved scatterometer winds and evaluating and interpreting their impact on GFS forecasts as our highest priorities for future reseach, given sufficient resources and time, we believe that the direct assimilation of scatterometer reflectivity measurements from ASCAT is a next important step in extracting the most from these sensor data.

At present, these measurements are not in BUFR format and considerable work must be performed to prepare this data before work on assimilating this data can be started. The goal for direct backscatter assimilation is to develop and implement a forward model for simulating ASCAT measurements from GFS first guess and to conduct assimilation experiments comparing results obtained from the project retrieval with the direct assimilations. There are several advantages of using direct backscatter assimilation which includes that the consistent changes in near-surface wind induced roughness and foam effects are produced through the forward models. Also, the improved

quality control and observation error specification comparing to the product assimilation is another advantage for this innovative idea. The backscatter assimilation component requires the development of the forward and its adjoint models and it requires working with NESDIS Center for Satellite Applications and Research (STAR) closely. Depending on the time constraint for operational milestones requirement and the compatibility of the GSI and JCSDA CRTM, this component will require work through 2010.

For all of the data assimilation experiments presented here, we propose to use the latest versions of NCEP's GDAS/GFS when possible. The latest version includes using the GSI and the global forecast model in hybrid sigma-p coordinates. As resources permit we will conduct experiments during two seasons at the current operational resolution of T382L64. We have been upgrading our algorithms to work in the latest releases of NCEP's GSI and will continue to do so. JCSDA computer resources capable of running and archiving the GDAS/GFS at the operational resolution will be required during 2009 for all experiments outlined in this section.
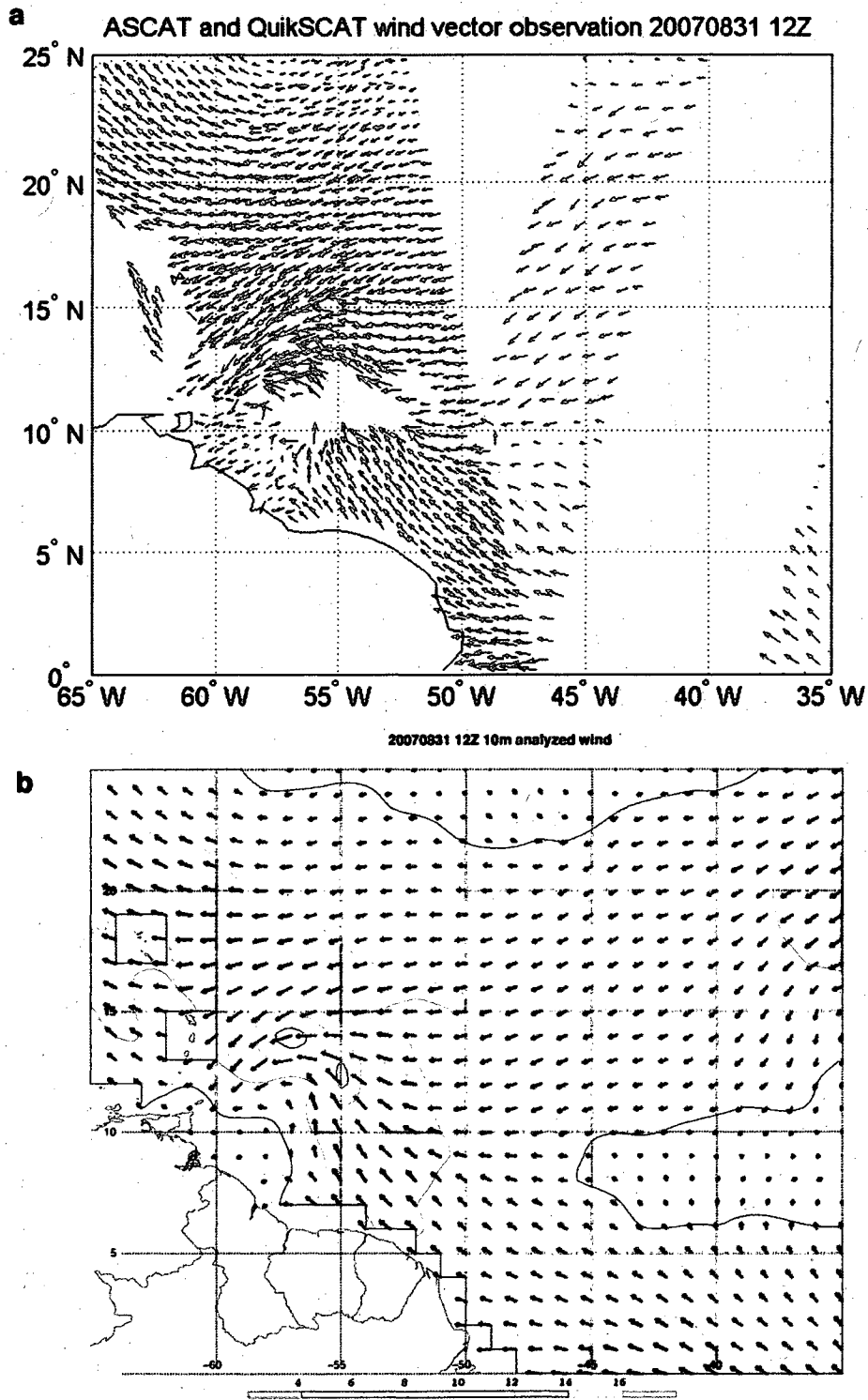
Figure 8.1. (a) ASCAT and QuikSCAT wind vector observation at 1200 UTC 31 August 2007 and (b) 10m wind from 1200 UTC 31 August 2007 GFS analysis.

References

Alishouse, J. C., S. Snyder, J. Vongsathorn, and R. R. Ferraro, 1990: Determination of oceanic total precipitable water from the SSM/I. *IEEE Trans. Geosci. Remote Sens.*, **28**, 811-816.

Arakawa, A. and W. H. Shubert, 1974: Interaction of a Cumulus Ensemble with the Large-Scale Environment, Part I. J. Atmos. Sci., 31, 674-704.

Bi, L., J. A. Jung, M. C. Morgan and J. F. Le Marshall 2008: A Two-Season Impact Study of the WindSat Surface Wind Retrievals in the NCEP Global Data Assimilation System. Submitted to *Wea. Forecasting*.

Bentamy, A., 2008: Characterization of ASCAT measurements based on buoy and QuikSCAT wind vector observations. *Ocean Sci. Discuss.*, **5**, 77-101.

Bettenhausen, M.H., Smith, C.K., Bevilacqua, R.M., Wang, N., Gaiser, P.W., and S. Cox, 2006: A Non-linear Optimization Algorithm for Wind sat Wind Vector Retrievals. *IEEE Trans. Geosci. Remote Sens.*, **44**, 597-610.

Burpee, R. W., 1972: The origin and structure of easterly waves in the lower troposphere of North Africa. *J. Atmos. Sci.*, **29**, 77-90.

Caplan, P., J. C. Derber, W. Gemmill, S. Hong, H. Pan, and D. F. Parrish, 1997: Changes

to the 1995 NCEP Operational Medium-Range Forecast Model Analysis-Forecast

System. *Wea. Forecasting*, **12**, 581-594.

Derber, J. C., D. F. Parrish, and S. J. Lord, 1991:The New Global Operational Analysis

System at the National Meteorological Center. *Wea. Forecasting*, **6**, 538-547.

Derber , J. C., Van Delst, P., Su, X. J., Li, X., Okamoto, K. and Treadon, R. 2003:

Enhanced use of radiance data in the NCEP data assimilation system. *Proceedings*

of the 13th International TOVS Study Conference. Ste. Adele, Canada, 20 October

– 4 November, 2003.

Derber, J.C. and W.S. Wu. 1998. The Use of TOVs cloud cleared radiances in the NCEP

SSI Analysis system. Mon. Weath. Rev. **126**, 2287-2299.

Figa, J. and Stoffelen, A. 2000: On the assimilation of Ku-band scatterometer winds for

weather analysis and forecasting. *IEEE Trans. Geosci. Remote Sens.*, **38**, 1893-

1902.

Gaiser, P.W., St. Germain , K.M., Twarog, E.M., Poe, G.A., Purdy, W., Richardson,

D., Grossman, W., Jones, W.L., Spencer, D., Golba, G., Cleveland, J., Choy, L.,

Bevilacqua, R.M., and P.S. Chang, 2004: The WindSat spaceborne polarimetric

microwave radiometer: Sensor description and early orbit performance. *IEEE Trans. Geosci. Remote Sens.,* **42,** 2347-2361.

Kalnay, E., M. Kanamitsu, and W. E. Baker, 1990: Global Numerical Weather Prediction at the National Meteorological Center. *Bull. Amer. Meteor. Soc.,* **71,** 1410-1428.

Kanamitsu, M., 1989: Description of the NMC Global Data Assimilation and Forecast System. *Wea. Forecasting,* **4,** 335-342.

Kanamitsu, M., J.C. Alpert, K.A. Campana, P.M. Caplan, D.G. Deaven, M. Iredell, B. Katz, H.-L. Pan, J. Sela, and G.H. White, 1991: Recent Changes Implemented into the Global Forecast System at NMC. *Wea. Forecasting,* **6,** 425-435.

Katsaros, K. B. , Forde. E. B ., Chang, P., and Liu, W. T. 2001: QuikSCAT facilitates early identification of tropical depressions in 1999 hurricane season. *Geophys. Res. Lett.,* **28,** 1043-1046.

Keyser, D., cited 2001a: Code table for PREPBUFR report types used by the ETA/3DVAR. [Available online from http://www.emc.ncep.noaa.gov/mmb/papers/keyser/prepbufr.doc/table_4.htm.]

_____, cited 2001b: Summary of the current NCEP analysis system usage of data types that do not pass through PREPBUFR processing. [Available online from http://www.emc.ncep.noaa.gov/mmb/papers/keyser/prepbufr.doc/table_19.htm.]

_____, cited 2003: Observational data processing at NCEP. [Available online from http://www.emc.ncep.noaa.gov/mmb/papers/keyser/data_processing/.]

Kistler, R., E. Kalnay, W. Collins, S. Saha, G. Withe, J. Woollen, M. Chelliah, W. Ebisuzaki, M. Kanamitsu, V. Kousky, H. Van den Dool, R. Jenne and M. Fiorino, 2001: The NCEP-NCAR 50-Year Reanalysis: Monthly Means CD-ROM and Documentation. *Bull. Amer. Meteor. Soc*, **82**, 247-267.

Lahoz, W. A., 1999: Predictive Skill of the UKMO Unified Model in the Lower Stratosphere. *Quart. J. Roy. Meteor. Soc.*, **125**, 2205-2238.

Le Marshall, J., Bi, L., Jung, J., Zapotocny, T. and Morgan, M. 2006: WindSat Polarimetric Microwave Observations Improve Southern Hemisphere Numerical Weather Prediction. *Aust. Meteor. Mag.* **56**, 35-40.

Le Marshall, J., Leslie, L., Morison, R., Pescod, N., Seecamp, R., and Spinoso, C. 2000: Recent Developments in the Continuous Assimilation of Satellite Wind Data for Tropical Cyclone Track Forecasting. *Adv. Space Res.*, **25**, 1077-1080.

Liu, W.T., and W. Tang, 1996: Equivalent neutral wind. JPL Publication 96-17, Pasadena, CA, 8pp.

Menzel, W. P., F. C. Holt, T. J. Schmit, R. M. Aune, A. J. Schreiner, G. S. Wade, and D. G. Gray, 1998: Application of GOES-8/9 Soundings to Weather Forecasting and Nowcasting. *Bull. Amer. Meteor. Soc.*, **79**, 2059-2077.

Miller, A.J., L.E. Flynn, S.M. Hollandsworth, J.J. DeLuisi, I.V. Petropavlovskikh, G.C. Tiao, G.C. Reinsel, D.J. Wuebbles, J. Kerr, R.M. Nagatani, L. Bishop, and C.H. Jackman, 1997: Information Content of Umkehr and SBUV(2) Satellite Data for Ozone Trends and Solar Responses in the Stratosphere. *J. Geophys. Res.*, **102**, 19,257-19,263.

Naderi, F.M., M.H. Freilich, and G.D. Long, Spaceborne radar measurements of wind velocity over the ocean: An overview of the NSCAT scatterometer system, *Proc. IEEE*, **79**, 850-866, 1991.

NOAA, cited 2000: NOAA KLM Users Guide, September 2000 revision. [Available online from http://www2.ncdc.noaa.gov/docs/klm/cover.htm .]

NOAA, cited 2005: NOAA Polar Orbiter Data (POD) User's Guide, November 1998 revision. [Available online from http://www2.ncdc.noaa.gov/docs/klm/html/c3/sec3-3.htm .]

NWS, cited 2006: NCEP Anomaly Correlations. [Available online from http://wwwt.emc.ncep.noaa.gov/gmb/STATS/STATS.html .]

QuikSCAT Science Data Product – User's Manual, September 2006 Version 3.0:

[Available online from

ftp://podaac.jpl.nasa.gov/ocean_wind/quikscat/L2B/doc/QSUG_v3.pdf]

Reed, R. J., D. C. Norquist, and E. E. Recker, 1977: The structure and properties of African wave disturbances as observed during Phase III of GATE. *Mon. Wea. Rev.*, **105**, 317-333.

Reed, R. J., E. Klinker, and A. Hollingsworth, 1988: The structure and characteristics of African easterly wave disturbances as determined from the ECMWF operational analysis/forecast system. *Meteor. Atmos. Phys.*, **38**, 22-33.

Rennick, M. A., 1976: The generation of African waves. *J. Atmos. Sci.*, **33**, 1955-1969.

Rogers, C. D. 2000. Inverse Methods for Atmospheric Sounding: Theory and Practice, *Singapore: World Scientific, 2000.*

Smith, W. L., H. M. Woolf, C. M. Hayden, D. Q. Wark, and L. M. McMillin, 1979: The TIROS-N Operational Vertical Sounder. *Bull. Amer. Meteor. Soc.*, **60**, 1177-1187.

Spencer, R.W., and J.R. Christy, and N. C. Grody, 1990: Global Atmospheric Temperature Monitoring with Satellite Microwave Measurements: Method and Results. *J. Climate*, **3**, 1111-1128.

Stoffelen, A., S. De Haan, Y. Quilfen, and H. Schyberg, 2002 : ERS Scatterometer

Ambiguity Removal Comparison, OSI SAF report, available at :

http://www.knmi.nl/scatteromter/publications/pdf/SAFOSI_W_ARcomparison.pd

f.

Thorncroft, C. D., and B. J. Hoskins, 1994: An idealized study of African easterly waves:

A linear view. *Quart. J. Roy. Meteor. Soc.*, **120**, 953-982.

Velden, C. S., C. M. Hayden, S. J. Nieman, W. P. Menzel, S. Wanzong and J. S. Goerss

1997: Upper-Tropospheric Winds Derived from Geostationary Satellite Water

Vapor Observations. Bull. *Amer. Meteor. Soc.*, **78**, 173-195.

Wu, W.-S., D. F. Parrish and R. J. Purser, 2002: Three-dimensional Variational Analysis

with Spatially Inhomogeneous Covariances. *Mon. Wea. Rev.*, **130**, 2905-2916.

Yu, T.-W., and R. D. McPherson, 1984: Global Data Assimilation Experiments with

Scatterometer Winds from Seasat-A. *Mon. Wea. Rev.*, **112**, 368-376.

Yu T.W. and W.H. Gemmill. 2004. Assimilation experiments at NCEP designed to test

quality control procedures and effective scale resolutions for

QuikSCAT/SeaWinds data 2004. *Proceedings of the 84th AMS Annual Meeting,*

Seattle, Washington, 11-16 January, 2004.

Zapotocny, T., W. P. Menzel, J. A. Jung, and J. P. Nelson III, 2005: A Four Season Impact Study of Rawinsonde, GOES and POES Data in the Eta Data Assimilation System. Part I: The Total Contribution. *Wea. Forecasting*, **20**, 161-177.

Zapotocny, T., J. A. Jung, J. F. Le Marshall and Treadon, R. 2007: A Two-Season Impact Study of Satellite and In Situ data I the NCEP Global Data Assimilation System. *Wea. Forecasting*, **22**, 887-909.